
# UNIVERSITY OF STUDY OF CATANIA

# INTERNATIONAL Ph.D. IN CHEMICAL SCIENCES

# XXXII CYCLE

## Ph.D. Thesis

***Marcello Condorelli***

*Metal nanoparticles shape control to enhance plasmon and catalytic properties*

**Department of Chemical Sciences**

*Ph.D. COORDINATOR: Prof. S. Sortino*

*TUTOR: Prof.ssa M.E. Fragalà*

---

**ACCADEMIC YEAR 2018-2019**

# Index

**Summary**... ... ... ... ..... ... ... ... ... ... ... ... ... ... ... ... ... ... ... ... ... .pag 5.

***Chapter 1***... ... ... ... ..... ... ... ... ... ... ... ... ... ... ... ... ... ... ... ... ... .pag 6.

- ***1.1 The magic of nanoparticles***... ... ... ... ... ... ... ... ... ... ...pag 6.
  - ***1.1.1 Understandig the Plasmon resonance***... ... ... ..pag 7.
  - ***1.1.2 Metal optical properties***... ... ... ... ... ... ... ... .pag 11.
  - ***1.1.3 Mie theory and rigorous models***... ... ... ... ... .pag 17.
  - ***1.1.4 Dipolar approximation***... ... ... ... ... ... ... ... ..pag 18.
  - ***1.1.5 Size effect on SP***... ... ... ... ... ... ... ... ... ... ..pag 20.
  - ***1.1.6 Shape effect***... ... ... ... ... ... ... ... ... ... ... ... .pag 22.
  - ***1.1.7 Dependence of SP on enviorment***... ... ... ... ...pag 24.
- ***1.2 Refractive index sensing and DS***... ... ... ... ... ... ... ... ..pag 25.
- ***1.3 SERS***..... ... ... ... ... ... ... ... ... ... ... ... ... ... ... ... ... ... ... .pag 26.

***Chapter 2***... ... ... ... ..... ... ... ... ... ... ... ... ... ... ... ... ... ... ... ... ....pag 31.

- ***2.1 Nano-materials***... ... ... ... ... ... ... ... ... ... ... ... ... ... ... ... pag 31.
  - ***2.1.2 Shape and dimension of nanoparticles***... ... ...pag 32.
- ***2.2 Synthetic Methodologies***... ... ... ... ... ... ... ... ..... ... ...pag 34.
  - ***2.2.1 Seeds-mediated growth***... ... ... ... ... ... ... ... ..pag 35.
  - ***2.2.2 Synthesis of Silver NPTs***... ... ... ... ... ... ... ...pag 36.
- ***2.3. Chemical-physical properties of NPTs*** ... ... ... ... ... ... ...pag 38.
  - ***2.3.1 Shape and size features***... ... ... ... ... ... ... ... ..pag 45.
- ***2.4 Theoretical modelization of experimental data***... ... ... ... pag 45.
- ***2.5 Effect of the synthesis kinetics on the shape and size of NPTs***... ... ... ... ... ... ... ... ... ... ... ... ... ... ... ... ... ... 

# Table of abbreviation and symbols

SP : Surface Plasmon

NP: Metal Nanoparticle

NPs : Metal Nanoparticles

AgNPs : Silver Nanoparticles

NPTs : Silver Nanoplatelets

NRs : Nanorods

VIS : visible region

NIR : Near Infrared Region

SEM : Scanning electron microscopy

AFM: Atomic force microscopy

SERS : Surface enhanced Raman spectroscopy

SAM : Self assembled monolayer

EF: Enhancement factor

R: Roundness

MOCVD: metallorganic chemical vapor deposition

CB: conducting band

VB: valance band

M: metal

MO: Metal oxide

$E_F$: Fermi energy

MB: Methylene blue

$\vec{P}$: Polarizability

$E_L$: Laser electric field

$p_r$: Raman dipole

$\omega_r$: Raman dipole oscillation frequency

RI: Refractive index

DS: Dipole sensitivity

MONSs: Metal-Oxide nanostructures

$\sigma_{ext}$: Extinction cross-section

$\sigma_{ads:}$ adsorption cross-section

$\sigma_{sca:}$ scattering cross-section

$\varepsilon_m$: dielectric constant of the medium

$\varepsilon$: dielectric function of metal

RIU: refractive index unit

PLAL: Pulsed laser ablation in liquid

AR: Aspect ratio

TSC: trisodium citrate

# Summary

In the last decades, the interest of scientific community on nanomaterials has increased rapidly. Indeed, in the last fifteen years the number of publications in the field increased from 19754 to 141663. This is a worldwide tendency, in fact, in 2015; more than 110 countries in the world took part in publishing of "nano-articles"[1].

The reason for this great interest in nanomaterials (specifically on metal nanoparticles, NPs) is attributed to the unique properties of nanomaterials with respect to the bulk materials. One of the most outstanding properties is the nanomaterials response to an "optical" electromagnetic radiation. This originates the so called Surface Plasmon (SP) resonance[2]. It consists in the collective oscillation of free conduction electron, on the surface of NPs consisting of positively charged ions, excited by the electromagnetic field of the incident light. The SP generate an intense electromagnetic field around the NP that increase greatly the light extinction at the resonant frequency. This behavior gives to scientist the possibility to manipulate, concentrate, and amplify the light at the nano-dimension[3] opening the door to a huge field of application for NPs, ranging from medicine to sensing and photo-catalysis and so on. The aim of this work is to study the necessary experimental condition to enhance ad modulate it, to make optical properties of NPs (particularly AgNPs) appealing at all technological level. Most of the work here reported is centered on photocatalysis and sensing application of SP. To reach this goal we first describe the correlation between NPs size and shape and their plasmon resonance features in regions which span from near ultraviolet to near infrared (300-1500 nm). A careful modification of the NPs synthetic approach is the key feature of this study. The experimental work is always supported by a

deep characterization of the obtained nanoparticles and of the related optical properties, thanks to a complete statistical study of shape and dimension through SEM and AFM analysis.

Then we try to fit the experimental results with the theoretical model using a numerical computational method (BEM) in collaboration with Prof. Meneghetti of Padova University. Because the theoretical model fits perfectly with our experimental results, we proceeded with sensing capability study. We focus on the production of SERS active substrate and Refractive index sensors. To prepare SERS substrate we functionalize silicon substrates with a silanization method or the nanoparticles, in a green functionalization method, so obtaining a SAM of AgNPs. We evaluated the SERS EF analyzing a standard molecule at known concentration. As refractive index sensor, we studied the sensibility of plasmon resonance to the variation of the refractive index medium of AgNPs, in colloidal dispersion. Specifically, we changed the RI of our NPs dispersion by diluting it in a sucrose solution with increasing concentration. After the complete chemical-physical characterization of AgNPs, we try to enhance furthermore the optical properties by combining our AgNPs with metal-oxide nanostructures of ZnO and $TiO_2$. The combination of NPs and MONSs give place to the so-called Schottky junction at the interface metal-metal oxide. The formation of Schottky junction causes the band alignment between the metal and the semiconductor generating many interface interactions, such as charge transfer, interface strain, and exciton-plasmon[4–6], that extend furthermore the application field of this hybrid nanostructures. We studied the chemical-physical properties also for these hybrid materials focusing on sensing and catalysis application. All these arguments will be discussed in more detail in the chapter of this work, starting from the phenomenon at the base of the whole thesis, the Plasmon resonance.

# *Chapter 1.*

## *1.1 The magic of Nanoparticles.*

The rise of human interest in nanoparticles is not of modern origin but has roots as old as humanity itself. The first evidence of the use of metallic nanoparticles dates back to the beginning of glassmaking in Egypt and Mesopotamia (1400-1300 BC). The red color in some pottery and glasswork, in fact, were attributed to the presence of Cu NPs[7]. Other evidence are colored glasses from bronze age (1000-1200 BC) founded in Italy [8]. The Lycurgus cup(400 AC) maybe it's the most famous ancient evidence of the use of nanoparticles in artwork, thanks to the presence of Au and Ag NPs, exhibit different coloration depending on the light direction[9,10]. At that time also Maya civilization used nanoparticles to produce blue paints[11]. In Middle ages, the variety of NPs for glass coloring increased even more[12,13]. All these achievements were empirically obtained and demonstrate that humankind, since ancient time, finds something of "unique and magic" in NPs. This interest is still the same today with the difference that today we now the "magic" behind NPs thanks to Gustav Mie's work in early XX century.

### *1.1.1 Understanding the SP*

In this section SP will be discussed in an accessible way, so every reader with different background could understand the physical phenomenon behind SP. As said before SP is a physical phenomenon born from the interaction between light an NPs. To obtain a mathematically correct interpretation of this phenomenon, the resolution of the Maxwell equation with the appropriate boundary condition is needed[14]. However, at this part of the work, a simplified

classical description of the phenomenon, it's useful to better understand the SP. NP could be considered as an ionic core with a sea of electron that moves all around the core. When this system is illuminated by the light, the electromagnetic field practices a force on NPs, exactly on electrons forcing them to move on the NPs surface. Because of this electron accumulation, a dipole is formed; with a negative charge on one side and positive charge in the other (figure 1). The dipole generates an electric field opposite to that of light forcing electrons to assume the equilibrium position, leading to a resonant density oscillation of conducting electrons. This restoring force's proportional to the displacement of electrons. Hence, when the electrons are displaced from the equilibrium position and the field it's removed, they will start to oscillate with a typical frequency called plasmon frequency. This behavior can be assimilated to the classical physical model of damped oscillator[15]. The dampening effect, in the case of SP, is due to the interaction of oscillating electrons with the ionic core and the surface of the NPs.

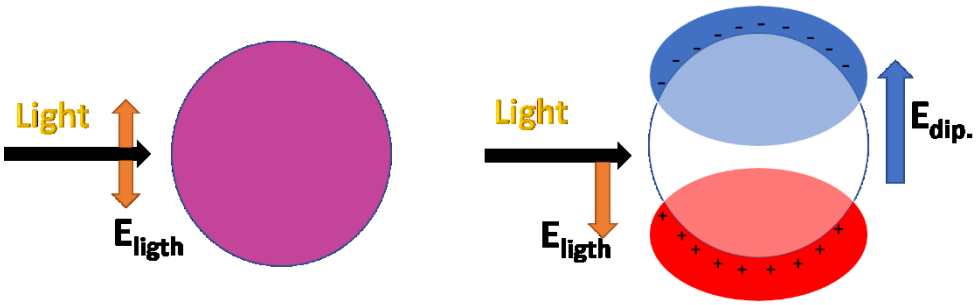


***Fig.1:*** *Scheme of the interaction of light with NPs the generation of dipole due to the separation of charges generate an electric field opposite to that of light.*

When an alternating force it's applied to a linear oscillator, the maximum amplitude of the oscillation will be obtained at the resonance frequency. It's possible to understand, hence, that if the frequency of light it's the same as the

plasmonic frequency the electrons will oscillate with the maximum of amplitude (figure 2). Even if is not possible to observe the oscillation of electron directly, it's possible to evaluate their amplitude thanks to the optical absorption. In fact, the electron oscillation involves the increasing of energy associated with the dipole, this energy it's provided by the light. Consequently, the light extinguishes partly when interacting with NPs at the resonant frequency this extinction will be maximum. For metal NPs this frequency corresponds to the UV-VIS light and so, SP makes appear absorption bands in the UV-VIS region of the spectrum (figure 2).

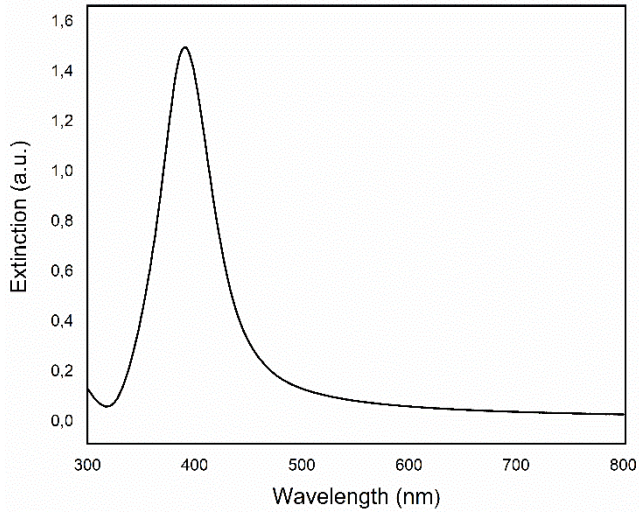


***Fig.2:*** *UV-VIS spectra of AgNPs, at resonant frequency (400 nm) the extinction of light is maximum, then decreases as it moves away from it.*

The absorbing efficiency of NPs it's associated with their absorption cross-section. The absorption cross-section it's defined as the section of a complete

opaque particle, that adsorb all incoming light, that will adsorb the same number of photons of the NP considered (figure 3 a). The light that interacts with NPs is not only adsorbed but it's also scattered so, it's possible to define a scattering cross-section. In this case, it's defined as the section of a perfect scatter particle, that scatter all photons, with the same scattering efficiency of the NP considered (figure 3 b).

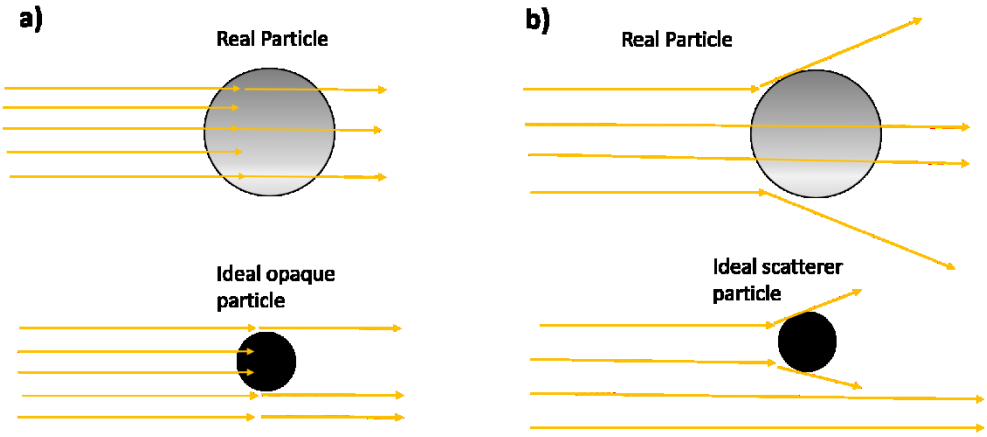


***Fig.3:*** *Illustration of adsorbing cross-section of a particle (a) and of scattering cross-section (b)*

The sum of these two quantities it's the so-called extinction cross-section and represent the efficiency of particles to remove photon from incident light, either by scattering or absorption. The value of extinction cross-section for an ideal opaque particle it's the geometrical section of the particle itself, that is equal to $\pi*R^2$. This behavior's the same for all particles and molecule that interact with light. But NPs distinguish from the rest of species, it's found, in fact, that the extinction cross-section for noble metal NPs are 10 times higher than their geometrical cross-section. In some way, the SP phenomenon makes NPs capable of adsorbing and scatter light even away from their physical

position. Considering that the intensity of light passing through a colloid of NPs decay exponentially with the extinction cross-section, according to equation 1:

$$I(x) = I_0 e^{-C\sigma x} \quad \textbf{(Eq.1)}$$

Were $I_0$ it's the intensity of incident light, C the concentration of NPs, σ it's the extinction cross-section and x is the distance traveled in the medium[15]. Consequently, a little increase in the extinction cross-section corresponds to a great enhancement of light absorption. So as said earlier SP give to scientist the possibility to concentrate the light at the nanoscale. This behavior can be explained in a simple way using a classical model. As already said the interaction between light and NPs induce a charge accumulation at NPs surface; as a result of which it generates an intense electromagnetic field inside and in a region larger than NPs physical size. In some region, the field is opposite to that of light, so their interaction is destructive, leading to an intense light extinction far from NPs surface. Meanwhile, in another region, the result of the combination between the field generated by the SP and that of light is a field with another propagation direction inducing light scattering. The sum of these two phenomena explains qualitatively the huge extinction cross-section of NPs.

### *1.1.2 Metal optical properties*

The classical description of SP can be useful as an introduction into the world NPs, but to better understand and try to control this phenomenon an accurate description is needed. Is to note that, Gaussian unit will be used for the description of the phenomenon.

One of the earliest theories for electrons in metals and their behavior was presented by Drude in 1900[16]. It is possible to give a quantitative interpretation to the classical model exposed before by starting from the Lorentz model, which describe the response to an electric field of a bonded electron in a generic material. Starting from the Lorentz model is possible to better understad the Drude model.

The Lorentz model, as said before, explains the behavior of an electron bounded, subjected to an external electromagnetic field. The electron in this condition will be affected by a recall force (-kx) when moved from its equilibrium position. This behavior can be interpreted with the model of the classic oscillator, and so the motion equation for such system will be :

$$m\frac{\delta^2 x}{\delta t^2} = -kx \quad \text{Eq. (2)}$$

Being m the mass of the electron, x the displacement from the equilibrium position, and $k=\omega_0^2 m$ the spring constant, the system's own oscillation frequency will be:

$$\omega_0 = \sqrt{\frac{k}{m}} \quad \text{Eq. (3)}$$

Considering, as said before, the damping of electrons due to the interaction with other electrons or the environment of the system, corrective terms must be introduced in equation 2 to take account of the damping behavior.

$$qE_0\cos(\omega t) = m\frac{\delta^2 x}{\delta t^2} + kx + \gamma\frac{\delta x}{\delta t} \text{ Eq. (4)}$$

Were $\gamma\frac{\delta x}{\delta t}$ is the friction coefficient that takes account of the dampening behavior, $\gamma$ is the dampening coefficient, q is the elementary charge and $E_0$ is the electric field. Being $k=\omega_0^2 m$ and $\gamma = \frac{m}{\tau}$ ,were $\tau$ is the time of scattering of the electrons of the material, by solving equation 4 the amplitude of electron displacement due the external electric field $x_0$ is obtained (equation 5):

$$x_0 = \frac{qE_0}{m[(\omega_0^2-\omega^2)+i\frac{\omega}{\tau}]} \text{ Eq. (5)}$$

Were ω is the frequency with which the electric field varies.
When an electromagnetic field, *E,* interacts with matter, it induces within the material a dipole $\mu_{ind}$ :

$$\mu_{ind} = x_0 q \text{ Eq. (6)}$$

Considering that the polarizability $\vec{P}$ of the material, subjected to an external electric field, is strictly dependent on the number of $\mu_{ind}$ generated, which in turn depend on the electric susceptibility χ of the material,it is possible to write $\vec{P}$ as follow:

$$\vec{P} = n\mu_{ind} = \chi E \text{ Eq. (7)}$$

Where n is the density of dipoles induced by the electric field, by imposing $E=E_0$ it is possible to find χ as described below:

$$\chi = \frac{n\mu_{ind}}{E_0} = \frac{nq^2}{m[(\omega_0^2-\omega^2)+i\frac{\omega}{\tau}]} \text{ Eq. (8)}$$

Now let's consider the dielectric displacement $\vec{D}$ , which is used to describe the electrical polarization of a dielectric material after the application of an electric field.

$$\vec{D} = E + 4\pi\chi E = \varepsilon \mathrm{E} \quad \text{Eq. (9)}$$

$$\varepsilon = 1 + 4\pi\chi \quad \text{Eq. (10)}$$

Were ε is the permittivity, by replacing equation 8 in equation 10 the Lorenz equation is achieved :

$$\varepsilon = 1 + \frac{4\pi nq^2}{m[(\omega_0^2-\omega^2)+i\frac{\omega}{\tau}]} \text{ Eq. (11)}$$

The above equation shows that permittivity depends on the frequency of the electric field, besides the plasma frequency and damping which are properties of the medium. Moreover if $\omega = \omega_0$ the system is in resonance condition, in fact, the denominator reach the minimum value, and $\varepsilon$ assume the maximum value possible for the system.

The Lorentz model gives a quantitative interpretation for the behavior of a generic material immersed in an electric field with bonded electrons. For a quantitative interpretation of a metal system in an electric field, the Drude model is needed.

The Drude model is based on three assumptions:

i. The metal is composed by a positively charged ionic core, and a number of free-electrons, not bonded to the ionic core, that become delocalized when the valence levels of the atom came in contact with that of other atoms[16].
ii. The interaction between, free-electrons and ionic core or other electrons are neglected; the only possible interaction is instantaneous collision with electrons environment. The average time between subsequent collisions of such an electron is $\tau$[16].
iii. After a collision event, the velocity (and direction) of the electron only depends on the local temperature distribution and is completely independent of the velocity of the electron before the collision event[16].

In metals, the electrons are not bound to the nuclei, hence they move freely around the lattice of the structure[17]. These delocalized electrons are the so-called “sea of electrons". In such condition the electron when is moved from

its equilibrium position, due to the electric field, is not affected by any "spring restoring force" that brings it back to its initial position. In this condition :

$$F_{spring} = -kx = 0 \text{ Eq. (12)}$$

$$k = \omega_0^2 m = 0 \text{ Eq. (13)}$$

This condition yields to $\omega_0 = 0$ that means that the system doesn't present any own oscillation frequency. Nevertheless the II assumption accepts that there's still a damping term, due to the collision within the electron cloud and the nuclei, so is possible to rewrite the equation 11 as follow :

$$\varepsilon = 1 + \frac{4\pi n q^2}{m(\omega^2 + i\frac{\omega}{\tau})} \text{ Eq. (14)}$$

This is the dielectric constant for a free-electron obtained by the Drude model. Not having the system, an own oscillation frequency, how is it possible to make it go into resonance? Setting :

$$\omega_p^2 = \frac{4\pi n q^2}{m} \text{ Eq. (15)}$$

Were $\omega_p^2$ is the plasmon frequency, is possible to rewrite equation 14:

$$\varepsilon = 1 + \frac{\omega_p^2}{(-\omega^2 + i\frac{\omega}{\tau})} \text{ Eq. (16)}$$

It is clear from equation 16 that if a metallic system is irradiate with light with:

$$E = h\nu = \hbar\sqrt{\frac{4\pi nq^2}{m}} \quad \text{Eq. (17)}$$

The system will enter in resonance and ε will reach maximum value.

These model obtained starting from a classical mechanical model, is useful to the understand and develop accurate insight on the optical properties of metals. Nevertheless, in some problems, the Drude models result to be unsatisfactory. For this reason more accurate models have been introduced.

.

### *1.1.3 Mie theory and rigorous models*

To obtain an accurate description of the SP and the associated light adsorption the Maxwell equation at NPs region must be solved, using the proper boundary condition. Obliviously, this is not a simple task, moreover, it is possible to obtain an analytical solution only for a certain dimension and geometry. The first to have succeeded in resolving this task for homogenous sphere was Gustav Mie in 1908[18]. The solution of Mie theory is valid for small non-interacting spherical particle. The extinction cross-section $\sigma_{ext}$ given by Mie theory is:

$$\sigma_{ext}=\frac{2\pi}{|k|}\sum_{i=0}^{\infty}(2L+1)Re[a_L+b_L] \quad \textit{Eq. (18)}$$

Where $a_L$ and $b_L$ correspond to:

$$a_L = \frac{m\Psi_L(mx)\cdot\Psi_L'(x) - \Psi_L'(mx)\cdot\Psi_L(x)}{m\Psi_L(mx)\cdot\eta_L'(x) - \Psi_L'(mx)\cdot\eta_L(x)} \quad ; \quad b_L = \frac{\Psi_L(mx)\cdot\Psi_L'(x) - m\Psi_L'(mx)\cdot\Psi_L(x)}{\Psi_L(mx)\cdot\eta_L'(x) - m\Psi_L'(mx)\cdot\eta_L(x)}$$

Being *k* the light wavevector in the dielectric medium:

$$k = \frac{2\pi\varepsilon_m^{1/2}}{\lambda} \quad \textbf{Eq.}(19)$$

$\psi_L$ and $\eta_L$ are the cylindrical *Bessel-Ricatti* functions, $m = n/n_m$, being n and $n_m$ are respectively the refraction index of the metal and that of the surrounding dielectric medium, and $x=|k|\cdot R$, were R is the NP radius. These equation results to be very hard to solve. For this reason, exist a large amount of approximation to simplify the calculation for well-defined geometry and dimension[19].

### *1.1.4 Dipolar approximation*

For NPs smaller than light <50 nm (considering that the resonance corresponds to the visible range) the most simple and common approximation is the dipolar approximation. The electromagnetic fields generated inside NP with a dimension smaller than light can be considered uniform, hence the NP can be considered and treated as a dipole. Another approximation applied in this case it's the quasistatic approximation, that assume electric field of light constant. With these conditions, the polarizability of a particle of volume V is:[20,21]

$$\alpha = 3\varepsilon_0 V \left(\frac{\varepsilon - \varepsilon_m}{\varepsilon + 2\varepsilon_m}\right) \quad \textit{Eq. (20)}$$

where $\varepsilon_0$ is the permittivity of vacuum, $\varepsilon_m$ is the dielectric constant of the medium and $\varepsilon$ is: $\varepsilon(\omega) = \varepsilon_r(\omega) + i\varepsilon_i(\omega)$ respectively real and imaginary part of the dielectric function of the metal. It is clear that $\alpha$ can become very large when the denominator is close to zero

$$\varepsilon_r = -2\varepsilon_m \quad \textit{Eq. (21)}$$

The denominator minimization is often denoted as the *Plasmon Resonance Condition*.

In this approximation the adsorption and scattering cross-sections, $\sigma_{ads}$ and $\sigma_{sca}$ are considered in terms of the dipolar polarizability:

$$\sigma_{ads} = k\, \mathrm{Im}(\alpha) \quad \textit{Eq.(21)}$$

$$\sigma_{sca} = \frac{k^4}{6\pi} |\alpha|^2 \quad \textit{Eq.(22)}$$

where $I_m$ is the imaginary part and k is the wave vector as defined in equation 19.

Considering that for particles smaller than light, $r << \lambda$, the scattering cross-section is negligible and the extinction cross-section, is mainly dominated by absorption result to be:

$$\sigma_{ext} = \sigma_{ads} = \frac{24\pi^2 R^3 \varepsilon_m^{3/2}}{\lambda} \frac{\varepsilon_i}{(\varepsilon_r + 2\varepsilon_m)^2 + \varepsilon_i^2} \quad \textit{Eq.(23)}$$

### *1.1.5 Size Effect on SP*

Size of NPs influences heavily the characteristic of SP. The features that are mainly influenced by the size are width, intensity, and position of the resonance[22]. As the ionic core of NPs radius increase, the number of conducting electrons increases as well, proportionally with the volume of NPs. As first consequence of this, the extinction of NPs increase with the increasing radius, as marked in equation 23. Although this consideration is valid based on the dipolar approximation, on the other side this approximation can no longer be considered valid when the NPs size approach the wavelength of light. When this occurs, NPs cannot be homogeneously polarized by the light resulting in excitation of higher-order oscillation mode[23], hence the NPs cannot be treated as dipole anymore figure 4.

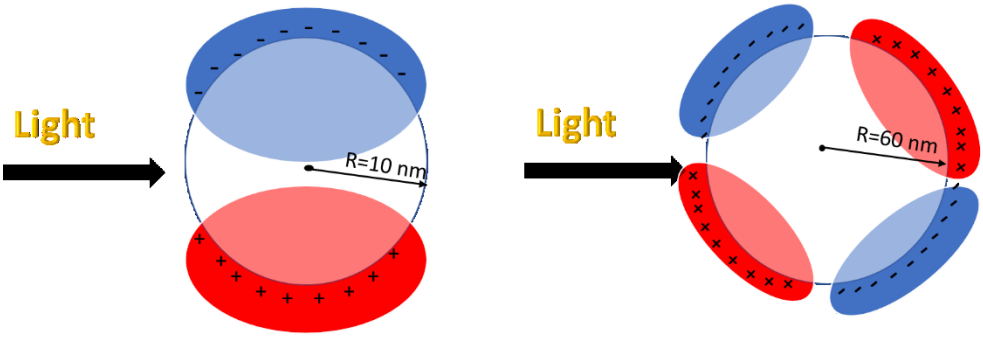


***Fig.4:****2-D illustration of the effect of size for NPs, left NP with radius 10 nm homogeneously polarized by light can be treated as a dipole; right NP with radius 60 nm, the polarization is no more homogeneous, NP must be treated as multipole.*

Higher-order modes resonance fall back to greater wavelengths, the general plasmon resonance condition (equation 21) for resonance mode of order l became:

$$\varepsilon_r = -\left(\frac{l+1}{l}\right)\varepsilon_m \quad \textit{Eq. (24)}$$

If l=1 (first-order mode) the equation 24 became the same of equation 20 relative to dipolar resonance mode, l > 1 corresponds to multipolar resonance peak, i.e. l=2 quadrupolar mode (figure 5). Higher-order modes, besides, present a significative broadening and redshift of the resonance peak due to a reduction of the phase coherence and electromagnetic retardation[24].

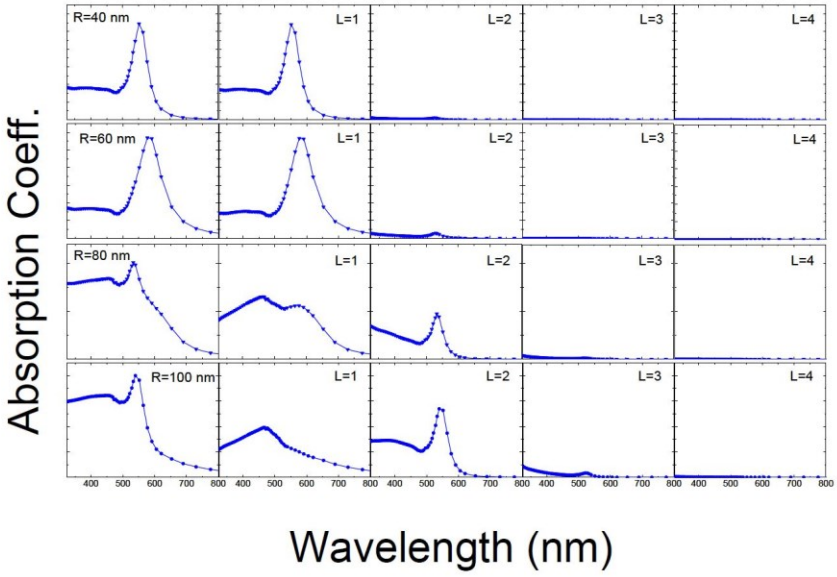


***Fig. 5***[15]***:*** *optical absorption spectrum for Au NP with different size, calculated by M.A. Garcia, according to the Mie theory, and the contribution of the different multipolar terms with increasing size*

The dependence of SP on the size of NPs explain the experimental broadening of the resonance peak. Nevertheless, the synthesis method for NPs has increased in the last years, the colloidal dispersion of NPs presents always size dispersion. Hence the experimental SP will be an average of all size present in the sample, causing a broadening of the experimental peak respect the calculated one.

### 1.1.6 Shape effect

The position of peak resonance it's strongly influenced by the shape of NPs; actually, the strength of the restoring force, generated as a response to the displacement of electrons due to the polarization by light, it's influenced by NPs geometry. In general, for surfaces with sharper edge, like NPTs or NRs,

along the light polarization direction, the restoring force result to be weaker, meanwhile orthogonally respect the light polarization direction it is stronger figure 6. These because the restoring force is proportional to charges accumulations.

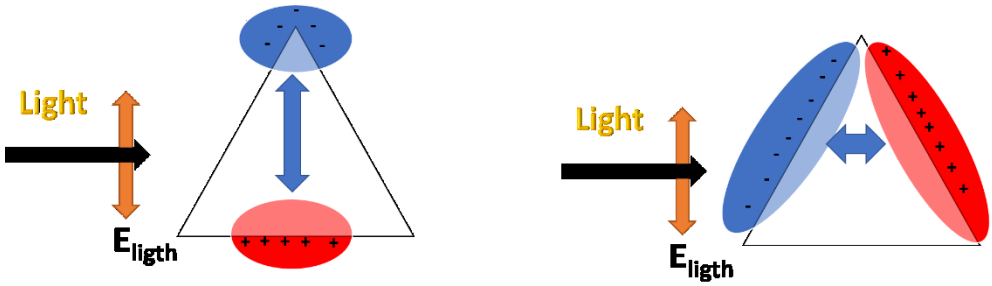


***Fig.6:****2-D Illustration of two possible charge accumulation (longitudinal and transversal) giving place to different plasmon resonance.*

Mathematically for any general shape the polarizability of a NP is[25] :

$$\alpha = \frac{\varepsilon_0 V}{L}\left(\frac{\varepsilon-\varepsilon_m}{\varepsilon+\left(\frac{1-L}{L}\right)\varepsilon_m}\right) \quad \textbf{Eq.}\ (25)$$

Where L is a depolarization factor, which depends on the shape of NPs. For spherical nanoparticles the value of L=1/3, hence for isotropic spherical NPs the equation 25 became equation 20. The plasmon resonance condition (equation 21) for non-spherical NPs became:

$$\varepsilon_r = -\left(\frac{1-L}{L}\right)\varepsilon_m \quad \textbf{Eq. } (26)$$

### *1.1.7 Dependence of SP on the chemical Environment*

SP is not only influenced by NPs characteristic like shape, size or type of Metal, but it is highly sensitive to the chemical environment surrounding the NPs[26]. Surrounding media, in fact, have two different effects on the SP. The first is that an increase in the medium $\varepsilon_m$ results in a more negative value of $\varepsilon_r$ to satisfy the plasmon resonance condition (equation 21), resulting in a redshift of the resonance peak. The second effect is an increase in the intensity of the resonance peak mathematically reflected in equation 23 where the proportionality between $\sigma_{ext}$ and $\varepsilon_m^{3/2}$ is clear. In simple words, when the dielectric constant of the medium surrounding NPs increase, SP redshift and increase his intensity proportionally to $\varepsilon_m$ as shown in figure 7.

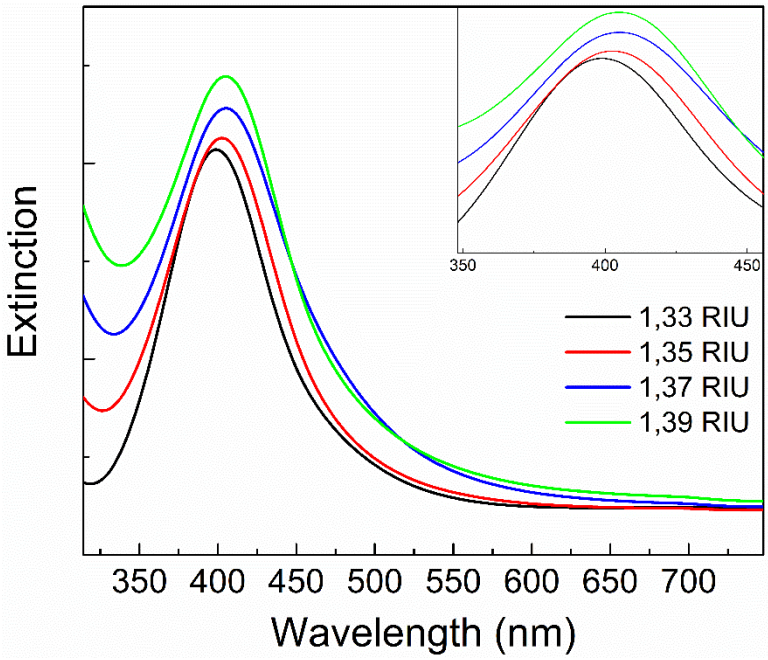


***Fig.7:*** *Experimental UV-VIS spectra of AgNPs with different medium with increasing $\varepsilon_m$. As predicted the SP peak redshift and increase its intensity with the increase of $\varepsilon_m$. In the inset is reported the magnification of the plasmon resonance to better appreciate the shift.*

This behavior turns out to be very interesting for this work, because open the possibility to create simple and easy to use RI sensors for the detection of variation of $\varepsilon_m$ around NPs.

### *1.2 Refractive index sensing and dipole sensitivity*

The redshift due to the increase of the RI of the medium is found to be linear respect the RI increase. By following the shift it's possible to detect changes in the chemical surrounding of NPs. These changes can be induced by the adsorption or the binding of a molecule into the surface of NPs. Obviously, to

obtain a specific sensor it is necessary to make the surface of the NPs selective to a target. This can be achieved by the conjugation of the NPs with specific recognition molecules which bind to the selected target[27]. For example, Silver NPs capped with biotinylated have been used to sense streptavidin molecules by specific biotin-streptavidin binding. Similarly, the detection of Alzheimer's disease has also been achieved using this strategy[28]. The advantage of this kind of RI sensor is that the Plasmon shift can be followed using a simple spectrophotometer. Is to note, that the aim of this work is not to produce a specific RI sensor for a specific target; but to study the better chemical-physical characteristic in terms of shape, dimension, and SP to produce NPs with enhanced RI sensibility to be used as a basis for specific very high-performance sensors. For this reason, in this work, refractive index sensitivity, or dipole sensitivity, has been defined as follows[29]:

$$DS = \frac{d\lambda_{LSPR}}{dn} \quad \textbf{Eq.}(27)$$

where n is the refractive index of the host matrix, $\lambda_{LSPR}$ is the wavelength at the maximum plasmon resonance, and $\varepsilon_r$ is the real part of the dielectric function of the metal constituting the nanoparticle. Thanks to DS is possible to evaluate the influence of shape, size, and plasmon resonance peak position on the sensibility of NPs to the variation of the surrounding chemical environment.

### 1.3 Surface-enhanced Raman scattering (SERS)

As already well established before in this work, SP generates an intense enhanced electromagnetic field localized inside and outside of NPs. This

enhanced field is capable of enhancing Raman spectroscopy signal[30,31] of a molecule in near proximity or bounded to the NPs surface in a process called Surface-enhanced Raman scattering. Raman is a spectroscopic technique used to observe vibrational, rotational, and other low-frequency modes in a system. It relies on inelastic scattering, or Raman scattering, of monochromatic light, usually from a laser in the visible, near-infrared, or near-ultraviolet range. The laser light interacts with molecular vibrations, phonons or other excitations in the system, resulting in the energy of the laser photons being shifted up or down. The shift in energy gives information about the vibrational modes in the system. Hence, Raman scattering is a powerful spectroscopy technique, that provides structural information on molecular structure, giving a molecular-specific signal that can be used for characterizing new molecule or to detect already know analyte. Even though it is a powerful technique, it still has a major drawback, molecules, in fact, present a small Raman scattering cross-section, resulting in a very low-intensity signal and in very low detection limit for the technique itself. The introduction of NPs as SERS active substrate gives the possibility to enhance the Raman scattering cross-section at the metal surface of $10^5$-$10^6$ times, thus increasing the detection limit up to nano-molar concentration. i.e. has been reported the detection and characterization of protein at in-vivo concentration[32] using an AgNPs substrate. While a part of this enhancement effect is attributed to a chemical factor, the major part is due to field enhancement near the NPs surface. To understand this phenomenon, is useful to discuss the Raman tecnique.

The Raman emission can be defined as the emission from a Raman dipole $\mathbf{p_r}$ oscillating at Raman-shifted frequency $\boldsymbol{\omega_r}$ induced by the exciting laser electric field $\mathbf{E_L}$. By using a linear response approximation is possible to define the Raman polarizability $\boldsymbol{\alpha_r}$ with a simple proportionality relation within the above parameters[33]:

$$p_r(\omega_r) = \alpha_r(\omega_L, \omega_r)E_L(\omega_L)$$ ***Eq.****(28)*

Were $\boldsymbol{\omega_L}$ is the oscillation frequency of the electric field of exciting laser.
The differential Raman cross-section, which characterizes the intensity of Raman scattering, is simply related to the power emitted by this Raman dipole. Considering the standard EM theory[34] the power of such dipole is proportional to $|p_r|^2$. Equation 28 can be used to understand the SERS effect. Considering a generic molecule adsorbed or in close vicinity to a metal NPs, in such condition the $p_r$ is affected by several factors so it is possible to rewrite equation 28:

$$p_s(\omega_r) = \alpha_s(\omega_L, \omega_r)E_S(\omega_L)$$ ***Eq.****(29)*

Were $\alpha_s$ and $E_s$ are the modified Raman polarizability and electric field at molecule position, due to the presence of NPs. It is possible from equation 29 distinguish two different cause of the modification of Raman signals:

- A modification to the value of $\alpha_s$ which is the so-called chemical enhancement. This kind of enhancement can be caused by different phenomena i.e. a weak electronic interaction between the molecule and the NPs, might result in a perturbation in the electronic density so changing the $\alpha_s$. Another possible phenomenon is the charge transfer between the molecule and NPs. This latter case is of great interest for this work because will be used to enhance the SERS capability of NPs.
- A modification in $E_s$ which corresponds to the electro magnetic (EM) enhancement. The electric field at the molecule position $E_s$ is strongly affected by the plasmonic response of the structure and result to be, as said before, much larger in magnitude than the incident field $E_L$[35], this

phenomenon is even more pronounced when the wavelength of the exciting laser is close to the optical resonance of NPs. The local field intensity in this condition can be as larger as $10^5$ especially for molecule located at “hot spots” (figure 8).

Is to note that experimentally the delimitation between the chemical and EM enhancement of Raman signals is not so clear-cut.

The electromagnetic part of the SERS enhancement is proportional to the square of the field intensity at the NPs[30] position. This phenomenon is one of the main interests of this work, in fact, the intensity of the field near the NPs and so the EM enhancement of Raman signals can be enhanced by tuning the chemical-physical characteristic of NPs. For example, by tuning the shape of NPs creating sharper curvature, like NPTs respect spherical NPs, can induce a stronger electric field at the tips of the nanostructures (lighting road effect) enhancing $10^7$-$10^8$ times the signal. Thanks to the production of SAM of NPTs, it is possible to obtain “hot-spot” (figure 8) where the edge of NPTs are nearly in touch, capable of intensifying the electromagnetic field and the signal of $10^9$ times.

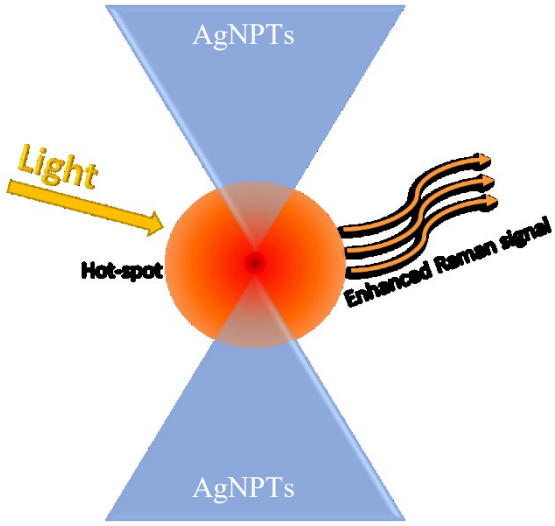


***Fig.8:*** *2-D Illustration of hotspot generated near the edge of two AgNPTs in near proximity. The signal of a molecule inside the hotspot could be enhanced up to $10^9$ times.*

In this work, the best chemical-physical characteristic will be studied, to produced NPs with maximum enhancement factor. To study the efficiency of SERS enhancing of the different NPs will be used the so-called enhancement factor (EF), defined as :

$$EF = \frac{I_{SERS}/C_{SERS}}{I_{RS}/C_{RS}} \quad \textbf{Eq.}(30)$$

Were $I_{SERS}$ and $C_{SERS}$ are respectively the intensity of the SERS signal and the concentration of a standard solution; $I_{RS}$ and $C_{RS}$ the intensity of normal Raman signal and the concentration of the standard solution used. Is to note that all experiment must be done with the same experimental condition in terms of objective and power of the laser used, and with $C_{RS} >> C_{SERS}$.

## Chapter 2

### *2.1 Nano-materials.*

Nanoparticles are generally defined as any particulate material for which at least one dimension lies in the range of 1−100 nm. They can exist in various shapes, such as spheres, rods, wires, stars, cages, platelet, etc. The various chemical processes that guide the synthesis of materials in the nanometer scale can be defined as nanochemistry, which plays a critical role in tailoring the physical and chemical properties of nanoparticles. Nanoparticles have several unique properties with respect to their bulk counterparts, which include high surface-to-volume ratio, high surface energy, unique mechanical, thermal, electrical, magnetic, and optical behaviors, etc. These properties make them suitable for a wide range of applications, ranging from electronics to energy harvesting and storage, to sensing, to biology, to medicine, and to catalysis.[36] One of the most interesting and useful properties of NPs is the well discussed SP. Thanks to this unique property, nanoparticles are suitable for applications in advanced chemical and biological sensing. In fact, these applications are mainly based on the sensitivity of the optical response of metal nanoparticles LSPR as well as on the capacity to enhance Raman signal of the analyte adsorbed near the metal surface[37]. All this feature depends on the shape, dimension and type of noble metal used. Another intriguing application for Plasmonic nanostructures deals with the possibility to combine them with conventional semiconductor photocatalysts in order to create materials with enhanced photo-activity[38]. In this context, mechanisms associated to charge transfer from the semiconductor to the metal, transfer of electrons from the photo-excited metal to the semiconductor and localized SPR-induced heating can be invoked: however, this coupling contributes to the improvement of the photo-activity due to the expansion of the absorbance spectrum in the visible region allowing for a better exploitation of solar light for activation of

photocatalysis. The most used semiconductor for photocatalysis is $TiO_2$ which adsorbs in the near UV region of solar spectrum

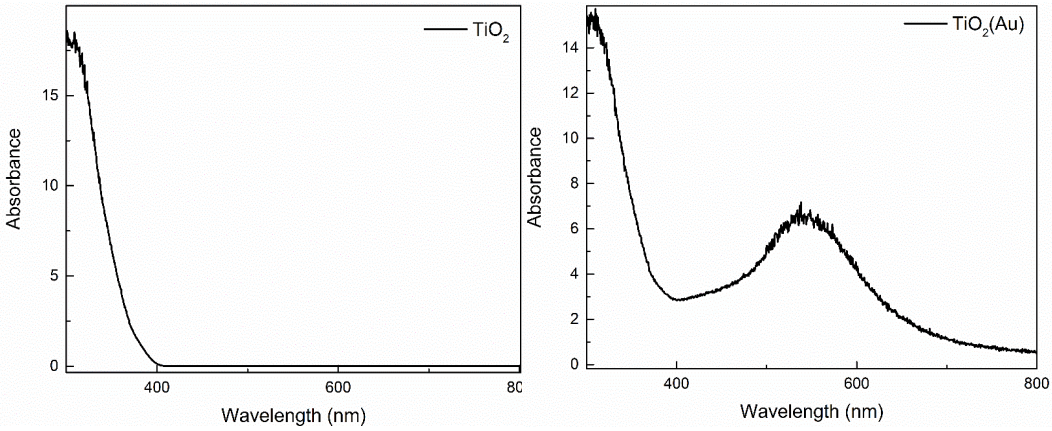


***Fig.9:*** *Absorbance spectrum of pure $TiO_2$ (a) and $TiO_2$ loaded with Gold NPs*

### *2.1.2 Shape and dimension of nanoparticles*

Noble metal anisotropic nanoparticles, differently from spherical shaped nanoparticles, exhibit multiple surface plasmon resonances due their size and shape (figure 9), as already said and reported in equation 26.


***Fig.10:*** *Different anisotropic AgNPs. The macroscopic coloration is an indication of a change in the plasmon resonance peak.*

When the edges of NPs became sharper the resonance peak redshift; moreover the increased dimension of NPs leads to the appearance of higher order resonance peak l>1 (equation 24) due to the inhomogeneity of the polarization of NPs. As a matter of fact, a slight change in particles geometry can produce great changes in their surface plasmon peak position, which can hardly be achieved using spherical nanosystems by a similar change in diameter[39]. In addition, the optical properties of anisotropic gold or silver nanorods (NRs) or prisms are tunable throughout the visible, near-infrared (NIR), and infrared regions of the spectrum[40]. For instance, triangular silver nanoplatelets show four plasmon resonances ranging from UV-visible to near-infrared (NIR), corresponding to different modes of plasmon excitation. Specifically, they show two first-order resonance peak l=1 associated with

dipole mode and two higher-order modes associated with quadrupole mode with l=2. Consequently, they are more versatile toward using different laser lines for getting larger Raman enhancements[37]: furthermore, the presence of shaped tips can enhance the electric field in their proximity, resulting in a very high enhancement of Raman signal and related surface plasmon resonance sensitivity. These specific properties make the anisotropic nanoparticles the most interesting systems on which this work is focus.

### *2.2 Synthetic Methodologies*

Since a sphere is the lowest-energy shape, a simple reduction of metal salts generally results in the formation of spherical nanoparticles. By proper control of the experimental parameters such as concentration of the metal precursor, reducing agents, and stabilizers and reaction conditions such as temperature and time, it is possible to tune the shape of the nanoparticles[40].

For these reasons, many different chemical and physical synthesis approaches have been proposed and investigated: seed-mediated synthesis, polyol synthesis, photochemical synthesis, electrochemical synthesis template-mediated synthesis, are just some of the most used.

Among the chemical synthesis, seed-mediated growth results to be the best synthesis for the aims of this work, because it's a simple, rapid, low-cost method and as it is accessible with ubiquitous laboratory equipment and offers the possibility to prepare higher quantities of nanoparticles than with other methods. Even if seed-mediated growth is an ideal way of synthesis of anisotropic NPs, it uses different kind of toxic chemicals for humanity an environment. Moreover, the presence of chemicals as byproducts of the synthesis could influence negatively the chemical-physical properties of the synthesized NPs. For all these reasons in this work, will be studied the seeds

mediated growth, and will be introduced also a new hybrid physical-chemical method, which consists in the synthesis of spherical nanoparticles by PLAL, and the subsequent, photochemical reshaping to obtain anisotropic Ag NPs by using non-toxic reagents.

### *2.2.1 Seeds-mediated growth*

The seed-mediated growth process is a widely used method that can yield various metal nanostructures such as rods, wires, triangles, stars, flowers, and so on[37]. This method it's a wet chemical synthesis and it's constituted by two steps: the first step is the formation of spherical AgNPs, the seed on which the NPTs will grow, by a traditional reduction process in which a salt of the noble metal is reduced by a strong reducing agent, in the presence of stabilizing agent. The second step is the growth of the nanoparticles, starting from the seeds and shaping them using different coordinating agents, mild reducing agents, and a precursor solution of the metal. The surfactant molecules will form suitable templates that facilitate the growth process to yield nanoparticles of desired morphology. Thanks to these steps, by controlling the reaction parameters homonucleation is hindered during the growth, thus preventing size broadening and production of undesired spherical nanoparticle. Herein, in this work AgNPTs have been fabricated with the seed-mediated growth method. Ag seeds are prepared by chemical reduction of $AgNO_3$ by using $NaBH_4$ and trisodium citrate. Different amounts of this solution (containing silver seeds) are added to another solution containing $N_2H_4$ and trisodium citrate, a more accurate focus on the experimental of the synthesis will be reported below. The fundaments of the seed-assisted growth of silver NPTs regard the ability to drive nanoplatelets growth via homo-nucleation by pre-existing seeding, thus disfavoring possible hetero-nucleation[41] events: in

particular, the presence of preformed seeds lower the energy of homo-nucleation, thus defining a preferential reaction path[42–44]. Of course, reactants concentration represents a crucial factor since if it is too high (more than a critical concentration) heteronucleation starts to compete causing a polydispersity in term of size and shape of obtained nanoparticles. For this reason the use of mild reductants, control of pH, rate of reactants addition as well the use of surfactants is essential to increase the energy barrier of hetero-nucleation[45,46]: luckily, standard reduction potential of silver is enough high ($E_0$ = +0.799 V) to permits the use of reducing agents as citrate ($E_0$ = −0.180 V) and hydrazine ($E_0$ = −0.230 V). Noteworthy, role of citrate ion is double since it can act as complexing agent of Ag+ ions, thus retarding reduction rate or Ag nanoparticles stabilizer (depending on pH). The hierarchical order of addition is important since it guarantees $Ag^+$ ions to be always in defect with respect to reducing and complexing agents. Platelets-like particles will grow by using the pre-existing spherical nanoparticles as nucleation agent, while the citrate will favor the anisotropic growth along Ag(100) surface.

### *2.2.2 Synthesis of Silver Nanoplatelets (NPTs)*

Some details on the experimental condition and “modus operandi” for the synthesis of AgNPTs are reported. Is to note that, experimental conditions have been modified to control shape, morphologies and the properties of the AgNPTs.

Three different solutions are prepared at room temperature to obtain AgNPTs:

1. SEEDS: Silver seeds solution is obtained by reducing 0,5 ml of a solution 59 mM of $AgNO_3$ with 0,5 mL of a solution of 20 mM of $NaBH_4$ in presence of 1 mL of 34 mM trisodium citrate solution as stabilizing agent in 10 mL of deionized water (18.2 MΩ*cm) at room temperature under strong stirring. The resultant solution was aged for 24 hours before use


***Fig.11:*** *Ag spherical NPs (seeds) formation process*

2. SOL (1): 50 µl of aqueous 400 mM hydrated hydrazine solution, 60 µl of aqueous 400 mM trisodium citrate solution and different quantities of silver seeds are added to 20 mL of deionized water.
3. SOL (2): 60 µl of 590 mM $AgNO_3$ are added to 6 mL of deionized water.

SOL (2) is added dropwise to SOL (1) under strong stirring conditions.

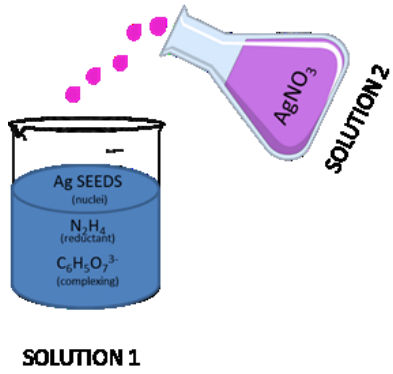


***Fig.12:*** *Experimental setup for the growth of AgNPTs*

To modulate the shape, dimension and optical properties of AgNPTs two parameters were varied:

1. The volume of seed solution to be added to SOL (1) ranging from 20 µl to 1 mL;
2. Addition time of SOL (2) to SOL (1) from 6 mL/min to 0.3 ml/min a peristaltic pump was used to regulate the flow rate.

### *2.3. Chemical-physical properties of NPTs*

AgNPTs have been characterized by UV-Vis spectroscopy (Jasco V-530), both in solution and after deposition.
Morphological characterization has been performed by atomic force microscopes (AFM- Witech Alpha 300 RS), field-emission scanning electron microscopies (ZEISS SUPRA 55 VP FE-SEM) and scanning transmission electron microscopes (STEM- JEOLJEM 2010).
Sensing capabilities have been estimated in term of Dipole sensitivity (DS).

It's reported the UV-Vis spectra of Ag seeds (Figure 13) and AgNPTs (Figure 14). Ag seeds spectrum is characterized by a resonance peak centered at 395 nm as predicted from equation 21; the narrow bandwidth indicates that the colloidal solution synthesized has a low degree of dispersion of dimensions and shapes.

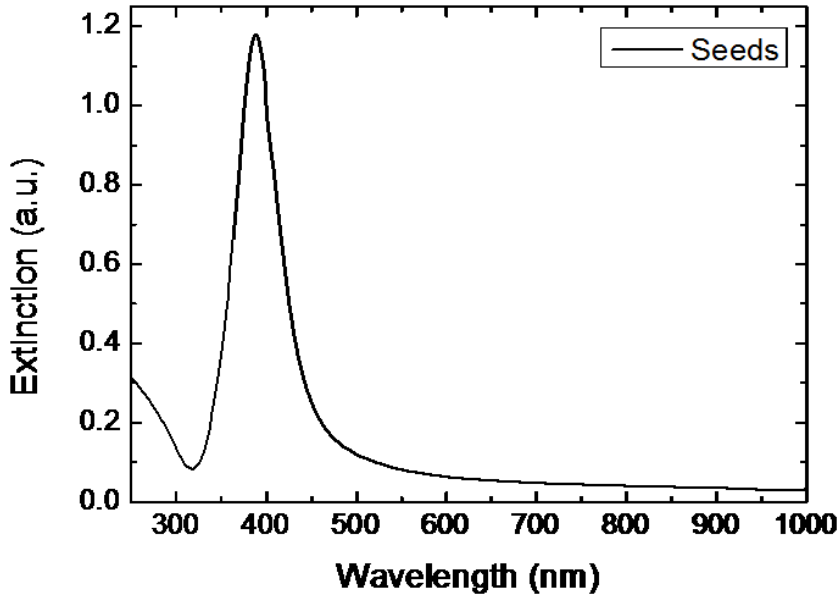


***Fig. 13.*** *Extinction spectra of Ag seeds solution the maximum of extinction is centered at 395 nm*

Figure 14 shows the extinction spectra of AgNPTs grown using different seeds volumes, ranging from 20 µl to 1 ml. It is interesting to note the main resonance peak results to be redshifted respect the Ag spherical NPs. this is in perfect agreement with the effect of the shape on the plasmon resonance frequency. In fact, as predicted from equation 26, the sharper are the edges of NPs than more redshifted SP will be. This first experimental evidence confirms that by changing the volume of seeds in the growth process it's

possible to obtain sharper NPs. Moreover, there are several new resonance peaks. Also, in this case this experimental result is predicted from the theory. Equation 24 predicts the existence of higher-order resonance peak with $l > 1$ for NPs, with dimension comparable with light frequency, redshifted and broadened. Considering this, it is evident that as the volume of seeds decreases the dimension and the sharpness of NPTs increased, which is further demonstrated by the broadening and increasing intensity of all order resonance, for the NPTs produced with the lowest volume of seeds (figure13 and table 1).These features give the possibility to tune the plasmon resonance from VIS to NIR. The different peak showed from NPTs are from the most intense to the lowest respectively:

- Longitudinal in-plane dipole mode l=1
- Longitudinal quadrupole mode l=2
- Transverse dipole mode l=1
- Transverse quadrupole mode l=2

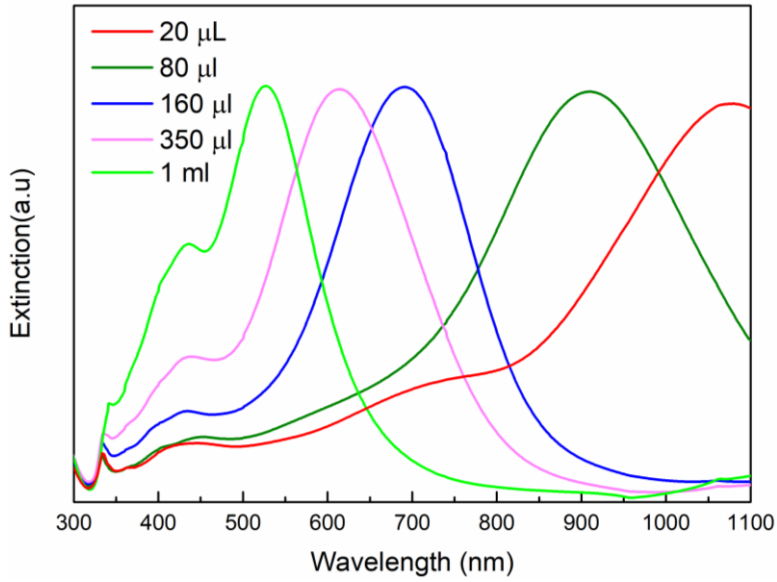


***Fig.14:*** *Extinction spectra of AgNPts produced with different seeds concentration (flow rate of 0.3 mL/min)*

| | Longitudinal Dipole $\lambda_{max}$ (nm) | Transvers Dipole $\lambda_{max}$ (nm) | Longitudinal Quadrupole $\lambda_{max}$(nm) | Transvers Quadrupole $\lambda_{max}$ (nm) |
|---|---|---|---|---|
| **20 µL** | 1075.6 | 440.8 | 731.5 | 331.3 |
| **80 µL** | 905.4 | 444.3 | 560 | 333.7 |
| **160 µL** | 692.1 | 396.3 | 433.2 | 333.1 |
| **350 µL** | 613.4 | 402.1 | 436 | 336.2 |
| **1 mL** | 526 | 402 | 433 | 343.5 |

***Tab.1:*** *$\lambda_{max}$ of NPTs grown with different seeds volume*

Is to note from table 2 that Longitudinal resonance result to be at a lower frequency, meanwhile transversal at highest frequency due to the difference

in the force of the restoring force as predicted in chapter 1 associated to the inhomogeneity of the charge distribution in NPs (figure 6).

Another parameter that permits to tune de SP properties, using this kind of synthesis is the addition flow rate of the precursor solution (SOL(2)). In graph 15 it's reported the evolution of the extinction spectra as a function of the precursor addition rate. NPTs have been synthesized by fixing initial seeds volume (20 µl, 80 µl, 160 µl, 350 µl, 1 ml) and by varying the adding flow rate of SOL(2) in SOL (1) from 6ml/min to 0.3ml/min. In figure 15 it's reported the spectra of NPTs synthesized with a fixed volume of 20 µl. All the other spectra are reported in the supplementary information at the end of this work (S1, S2, S3, S4). The reported spectra present a component at λ=400 nm associated with secondary nucleation which produces mostly spherical nanoparticles at high addition rates.

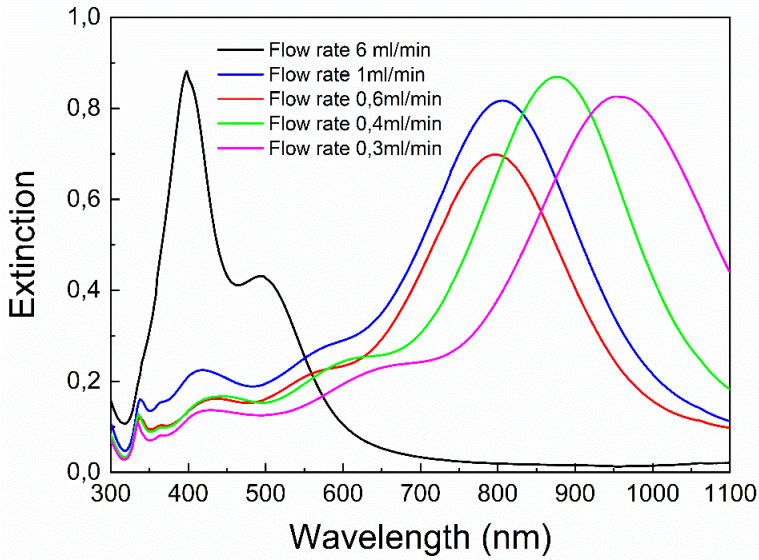


***Fig.15:*** *Extinction spectra of NPT grown with 20 µL with different addition flow rate.*

The slower is the addition rate the more pronounced is the redshift of $\lambda_{Max}$: noteworthy, using a seed volume of 20 µL and 80 µL (Figure 15 and Table 1) the longitudinal resonance peak is in the near IR region for the slowest adding rate. When the addition rates are significantly slow-down, the contribution related to secondary nucleation is not visible in the spectra anymore. It's clear that by slowing down the adding the rate the growth of big triangular-shaped NPTs is favored with respect to homonucleation of spherical NPs. In figure 16 are reported the positions of the $\lambda_{Max}$ as function of SOL (2) addition rate for the different AgNPTs colloids. For samples obtained by using a seeds volume of 160 µL, 350 µL and 1 mL, $\lambda_{max}$ reaches a plateau at faster flow rate of 1.2 ml/min (5 min), while by lowering the seed volume down to 20 and 80 µl the saturation of $\lambda_{max}$ requires slower SOL (2) flow rate 0,3 ml/ min (20 min) to be reached.

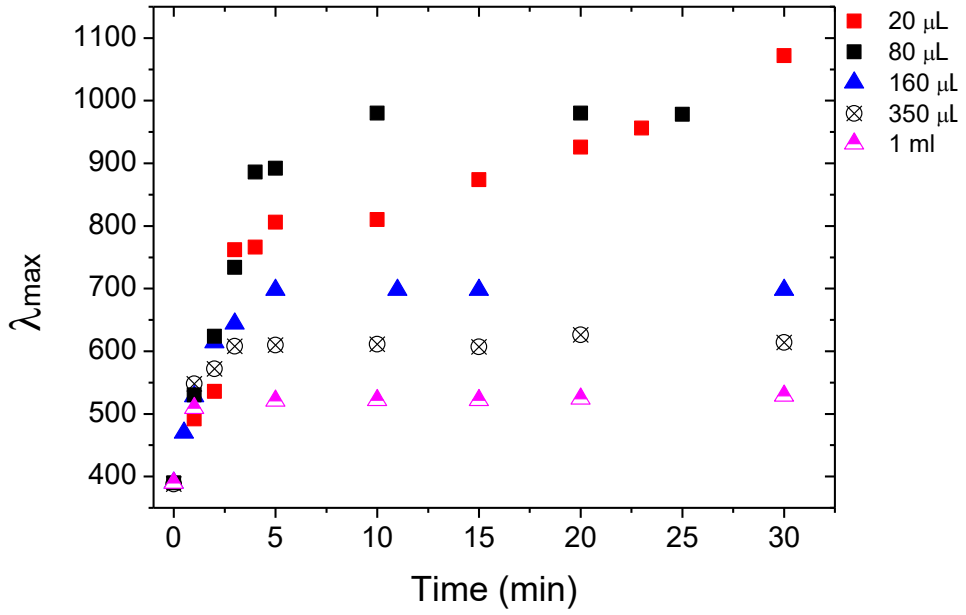


***Fig.16:*** *In-Plane dipole resonance $\lambda_{Max}$ trends where the time corresponds to the time for adding 6ml with a given flow*

It's possible to associate the growth kinetics to a classical saturation model, which can be well presented by the empirical relation:

$$\lambda_{LSPR} = (\lambda_{sat} + \lambda_{sat} - \lambda_0)e^{(-kt)} \quad \textit{Eq. (31)}$$

Where λsat is the saturation value for λ, k the kinetic constant *indicates* how fast the growing process is, and the parameter $\lambda_0$ which represents the plasmon wavelength position at t = 0. λsat gives the final position of the longitudinal dipole mode, once the growth is finished[29] The empirical relation in equation (31) clearly originates from a first-order kinetics. Xia et al.[47] have recently proposed the use of such a law in seed-mediated growth of colloidal metal nanocrystals. Thanks to this kinetic relation, it's possible to predict, once fixed the experimental parameters such as temperature and concentrations, the position of plasmon resonance in the UV-VIS spectra.

In table 2 the $\lambda_{max}$ of the Longitudinal dipole resonance peak as a function of SOL (2) adding time are reported

| | *Time of addiction 1 min* | *Time of addiction 2 min* | *Time of addiction 3 min* | *Time of addiction 5 min* | *Time of addiction 10 min* | *Time of addiction 20 min* | *Time of addiction 30 min* |
|---|---|---|---|---|---|---|---|
| ***20 µL*** | *492.2 nm* | *550nm* | *763nm* | *804nm* | *873nm* | *925nm* | *1073 nm* |
| ***80 µL*** | *526nm* | *620nm* | *733nm* | *888nm* | *981nm* | *980nm* | *981nm* |
| ***160 µL*** | *554nm* | *611nm* | *645nm* | *698nm* | *700nm* | *701nm* | *702nm* |
| ***350 µL*** | *547nm* | *572nm* | *591nm* | *631nm* | *636nm* | *638.5nm* | *637nm* |
| ***1 mL*** | *509nm* | *515nm* | *518mn* | *520nm* | *521nm* | *520nm* | *522nm* |

***Tab.2:*** *$\lambda_{max}$ of nanoplatelets grown by the different time of addition of solution 2*

### *2.3.2 Shape and size features*

AgNPTs have been morphologically characterized by SEM, STEM and AFM techniques in order to estimate their shape and to calculate their aspect ratio (length/thickness) and to evaluate their roundness. Here it's reported just the data for NPTs synthesized with 20 µl all the other data can be found in the supplementary information (S5, S6, S7, S8). Together with the morphological characterization are reported also a statistic study on the aspect ratio (length/thickness) and the roundness of NPTs synthesized with 20 µl and 80 µl. This statistic data will be used for a modelization of NPTs

AFM characterization of the AgNPTs obtained by using 20 µl of seeds is reported in Figure 17.

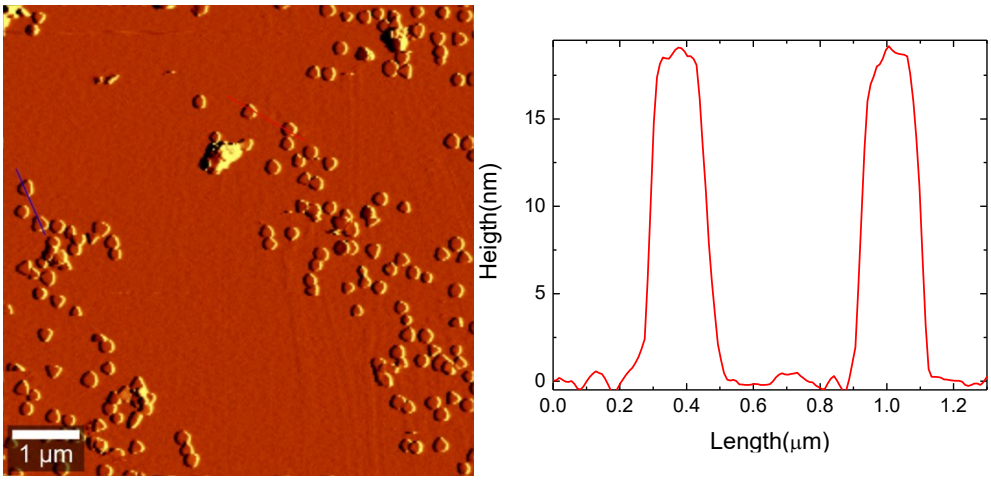


***Fig.17:*** *AFM image and section analysis of Silver Nanoplatetelets grown with 20 µL of seeds*

From section analysis, it is possible to estimate the NPTs aspect ratio. It is possible to observe how AgNPTs thickness remains unchanged, while their lateral dimension (length) increases. These data are summarized in Figure 18:

accordingly, the resulting aspect ratio varies from 3 to 13 as the seeds volume decrease. This is the result of the selectivity of citrate to bind on specific crystal facet thus allowing the growth of facet (111) at disadvantage of (100)

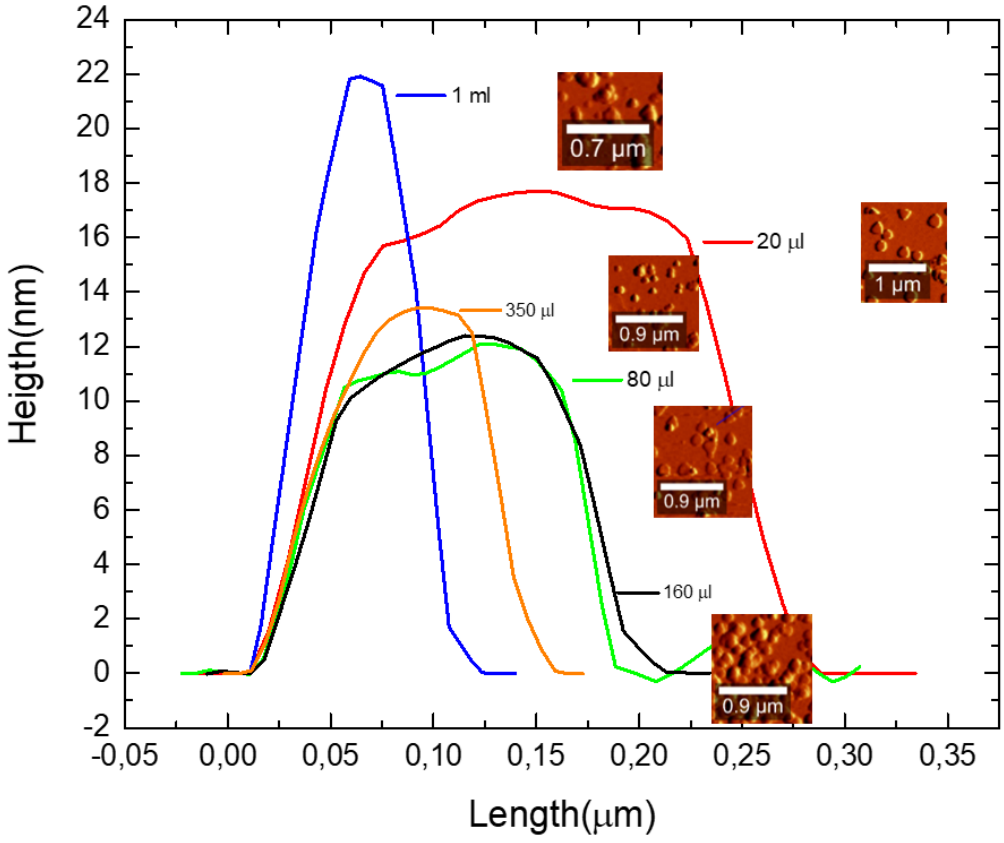


***Fig.18:*** *AFM image and section analysis of Silver Nanoplatetelets grown with different volume of seeds.*

In table 3 are reported the statistical study of length and thickness for all AgNPTs synthesized with different seeds volume.

| | Thickness(nm) | Length(nm) | Aspect Ratio | Dipole plasmon resonance(nm) |
|---|---|---|---|---|
| **20 µL** | 17 | 203 | 16 | 1075.6 |
| **80 µL** | 11 | 140 | 12 | 905.4 |
| **160 µL** | 11 | 140 | 12 | 692.1 |
| **350 µL** | 13 | 105 | 8 | 613.4 |
| **1 mL** | 21 | 64 | 3 | 526 |

***Tab.3:*** *Thickness and Length of NPTs with relative aspect ratio and dipole resonance.*

Ag NPT aspect ratio (edge length divided by thickness), increases from 3 to 16 (Tab. 3) It's to note that the aspect ratio increases concomitantly with the LSPR redshift, which reach the maximum value of 1075 nm for the biggest nanoplatelets with an aspect ratio of 16. Accordingly, with this experimental data as the dimension of NPTs increase, their sharpens increase to and the SP redshift. SEM images of two colloids with resonance peak at 1100 nm and 788 nm (red and blue curve in figure 14) are reported in image 19 and 20 respectively.

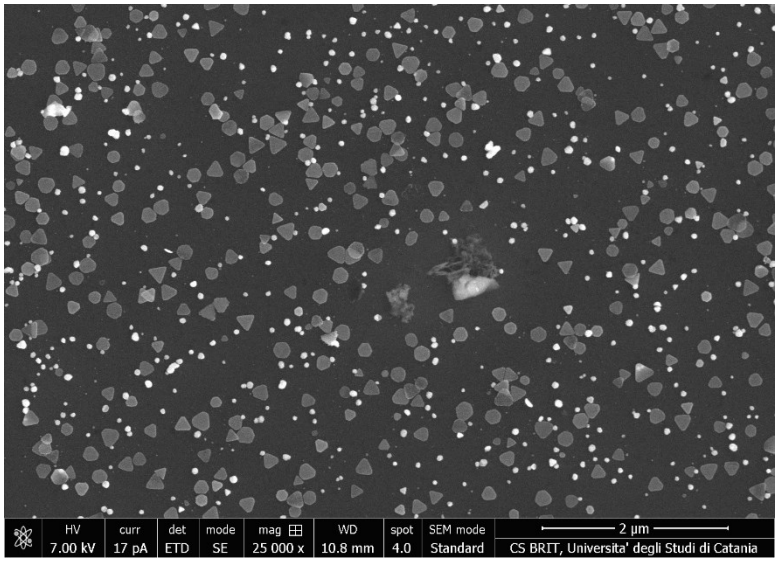


***Fig. 19:*** *SEM image of NPTs with Spat 1100 nm.*

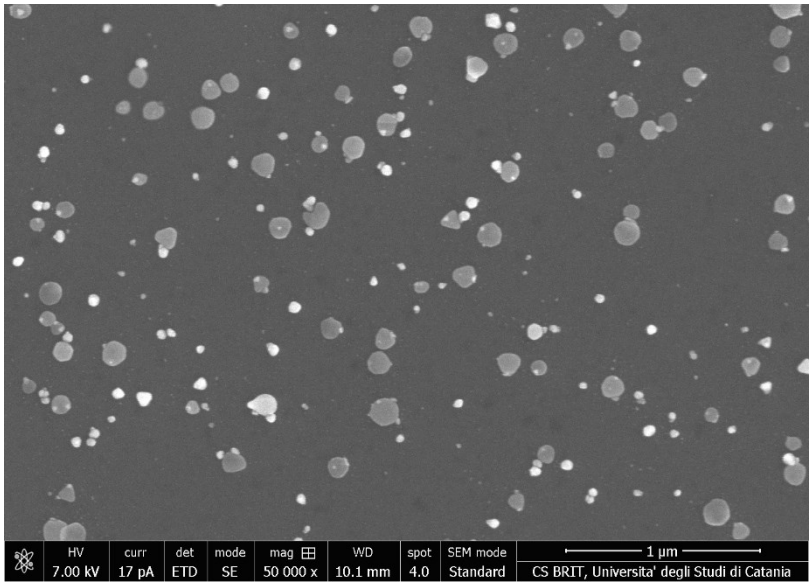


***Fig. 20:*** *SEM image of NPTs with SP centered at 788 nm here the hexagon-shaped NPs are the most numerous*

In figure 19 it's evident the prevalence of triangular-shaped NPs with a little number of other shapes for NPTs with resonance peak at 1100 nm (red curve figure 14). This result is perfectly consistent with the theory, in fact, for sharper NPs the SP redshift as predicted from equation 26. This is also concordant with image 20 where NPTs with resonance peak at 788 nm (blue curve figure 14) show a big number of hexagons with less sharp corners. As confirmation of this data, a statistical study of these two NPTs in terms of AR and roundness it's reported. Using this statistical data, particularly 100 NPs were analyzed, a theoretical study it's reported. The aim of such calculation is to create a model able to predict a priori the plasmonic properties of NPs with certain geometries and shapes. The "roundness" R has been calculated as follow.

First, the values for a perfect circle, a regular hexagon, and an equilateral triangle are given in equation 32-33. In figure 21 is reported the geometrical explanation of the roundness as defined in this work.

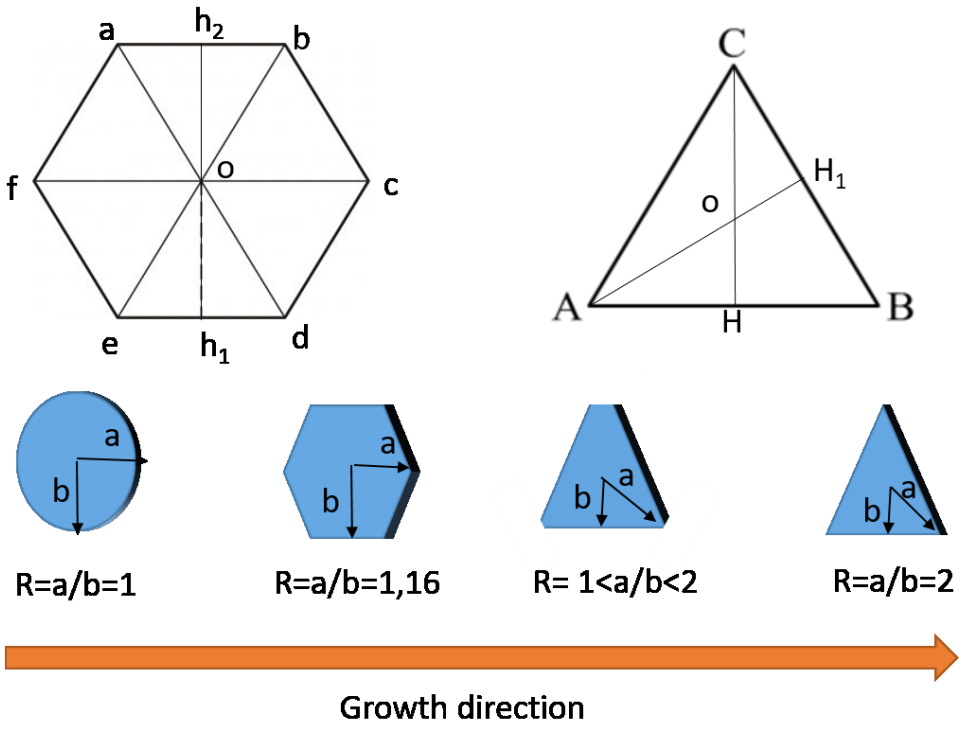


***Fig 21:*** *Geometrical representation of a sphere, a truncated triangle, equilateral triangle and regular hexagon with relative limit value of Roundness as defined from equation 32-33 equation*

The limit values of roundness for the respective geometries have been calculated as:

1) Regular hexagon $\frac{ad}{h1h2} = 1{,}16$ ***Eq.****(32)*

2) Equilateral Triangle $(\frac{2AH1}{3})/(\frac{CH}{3}) = 2$ ***Eq.****(33)*

The same formulas have been applied for the evaluation of the roundness of the nanoparticles from the SEM images. In figure 22 is reported the statistic

on the aspect ratio and on roundness for NPTs with resonance centered at 1100 nm. It's clear that the distribution of AR is centered at 15 meanwhile the R present two distribution: one constituted by a little number of particles with R=1.12, typical of hexagonal-shaped NPs, the second one presents an R=1.8 typical of triangular NPs.

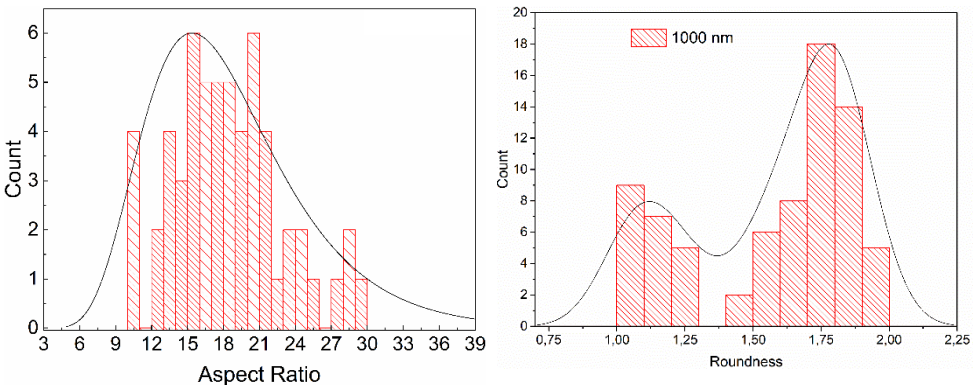


***Fig.22:*** *Statistical distribution of 100 NPTs with SP at 1100 nm AR centered at 15(left); Statistical distribution of R with two maxima R=1.16 and 1.8.*

Because of this bi-distribution, the main resonance peak in the red curve in figure 14 is very broadened. The optical properties, in fact, as already said in chapter 1, are an average of al shape and size contained in the colloidal dispersion. In figure 23 it's reported the statistical distribution of NPTs with main resonance peak at 788 nm. In this case, the distribution of AR it's centered at 11 indicating the smaller size of NPTs. The R distribution is centered at 1,17. This value is typical of hexagonal-shaped NPs.

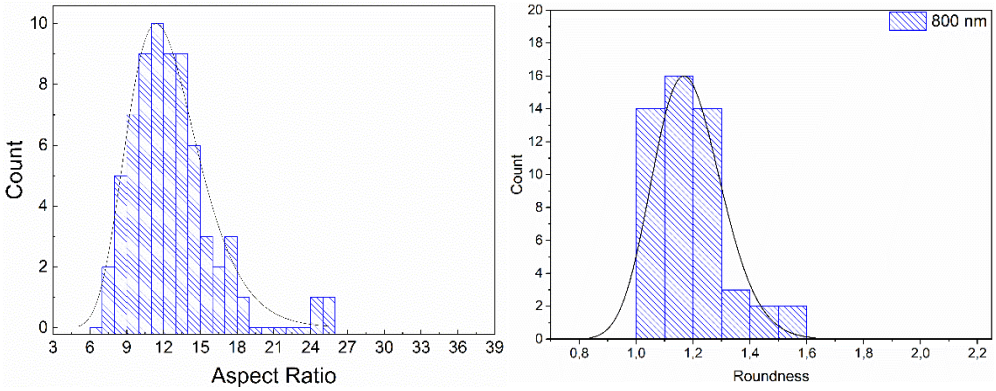


***Fig.23:*** *Statistical distribution of NPTs with resonance at 788 nm AR centered at 11 (left); Statistical distribution of R with maximum R=1.17*

However, since only NPs with this shape are present, the main resonance peak (blue curve figure 14) result to be narrower respect to the NPTs with the bi-distribution.

### *2.4 Theoretical modelization of experimental data*

From these statistical data, it's clear the direct dependence on AR and R of the position and shape of the plasmon resonance. As confirmation of this, are reported two BEM simulation, thanks to Prof. M. Meneghetti of the University of Padova, of two NPs with the same shape and size founded with the statistical study. BEM is a numerical computational method of solving linear partial differential equations , which have been formulated as integral equations. This method permits to solve Maxwell's equations for a dielectric environment where bodies with homogeneous and isotropic dielectric functions are separated by abrupt interfaces like NPs immersed in a dielectric.

Specifically, in figure 24 is reported the BEM simulation for NP with AR = 15 and R = 1.8 and for a NP with AR = 11 and R = 1.17

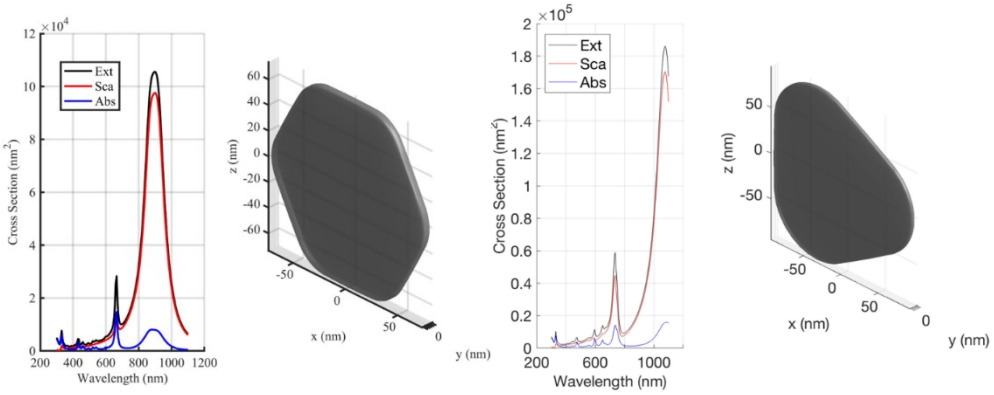


***Fig.23:*** *BEM calculation of well-defined anisotropic NPs. Left for hexagonal NPs Right for triangular NPs*

The simulation considers a spectral range of 300-1100 nm. The results obtained, in terms of the position trend of the maximum band/roundness factor, are absolutely consistent both with plasmonics, and experiments: the greater is the size and/or roundness factor, the greater is the redshift of the band.

The hexagonal particle has its maximum towards 800-900 nm, the triangle particle has its maximum between 1000-1100 nm.

In addition, the simulations also show the contribution between 600-800 nm due to higher-order modes l>1. Moreover, it's clear that, there is a major contribution of the scattering cross-section of NPs to the light extinction. This finding is consistent with the theory on the effect of NPs dimension, as explained in chapter one.

### *2.5 Effect of the synthesis kinetics on the shape and size of NPTs*

Here is reported the investigation of the effect of the variation of adding flow rate in the growth process, on the shape and size features of NPTs. The following figures show the STEM images of different NPTs grown with fixed seed volume ( 20 µl) and variable adding time of SOL (2) ranging from 1 minute to 20 minutes. AgNPTs dimensions increase upon decreasing the adding rate. Even more evident is the reduction spherical NPs present in solution thus confirming the role of growth kinetic in the overall process.

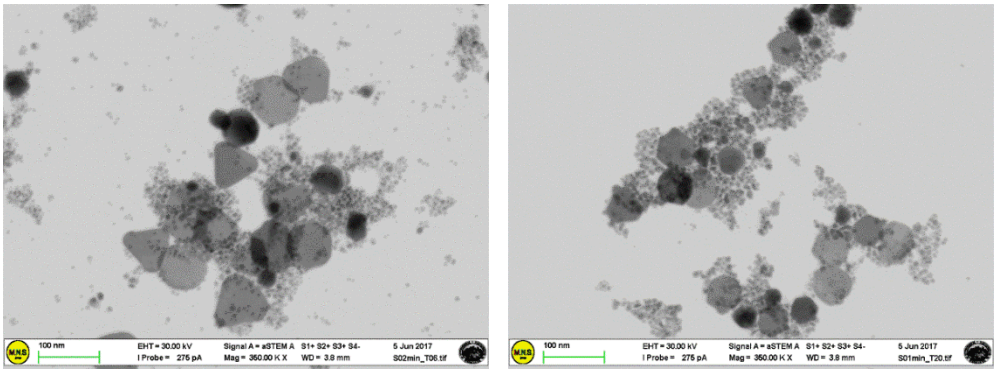


***Fig 24:*** *TEM images of NPT grown with 20 µl with left 1minute, right 2 minutes of precursor addiction*

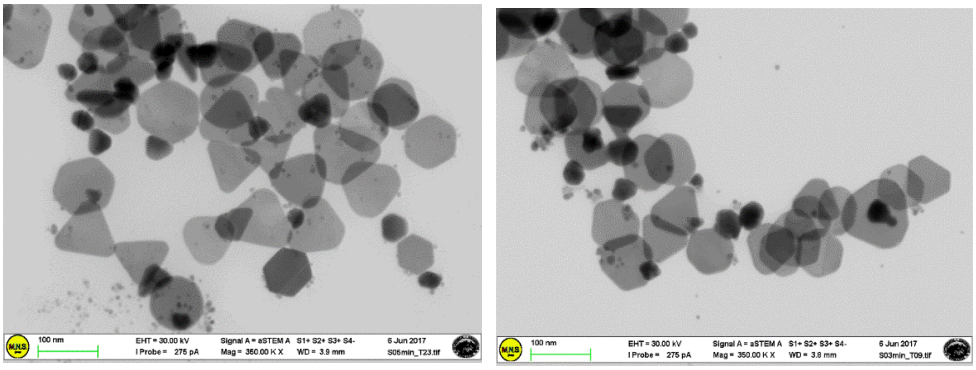

***Fig.25.*** *TEM images of NPT grown with 20 µl with: left 3 minutes, right 5 minutes of precursor addiction*

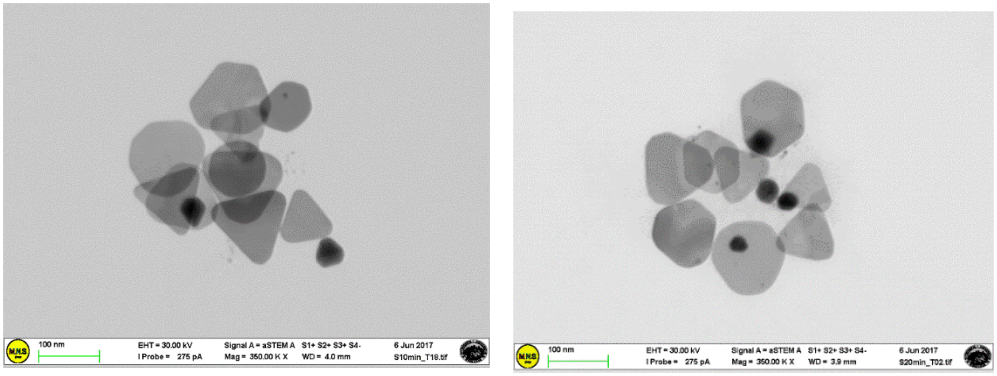

***Fig.26.*** *TEM images of NPT grown with 20 µl with: left 10 minutes right 20 minutes of precursor addiction*

Here is evident the competition between homonucleation mechanism (favored if $AgNO_3$ is added with high rate) which produce mostly spherical, particles and the growth of plates due to the heteronuclation mechanisms. Homonucleation generates the classical 400 nm signal (slightly shifted to

higher wavelengths with respect that measured for the seeds colloid due to increased dimension of the new formed NPs), while heteronucleation gives the characteristic in-plane dipole mode which moves redshifting during the growth process. TEM data reported give an idea of the seed-mediated growth synthesis kinetics, once the $AgNO_3$ addition rate is increased. At high addition rates, the plates are quite small, and the presence of spherical nuclei is evident. At the lowest rates, perfect isolated plates of large size are formed. Of course the intensity of the signal at 400 nm, relative to spherical NPs, decrease while the plates growth.

### *2.6. A green way of synthesis for Anisotropic NPs: light reshaping process*

As already said before, even if the chemical synthesis of NPTs results to be one of the best ways of synthesis, the use of chemicals like $N_2H_4$ and $NaBH_4$ which are toxic and cancerous for humankind and environment, makes it an unsustainable synthesis for the environment and humankind. Moreover, the presence of byproducts, due to the synthesis process, bonded on the surface of NPs could influence the properties of NPs. For this reason, in this work is presented a new method of synthesis[48] which combine a physical way of synthesis like PLAL with a photochemical reaction to reshape a spherical pure NPs. Also, in this case the synthesis is divided into two steps:

1. Synthesis of spherical NPs by PLAL method in pure water in the presence of TSC.
2. Reshaping process of synthesized spherical NPs under light irradiation in presence of $H_2O_2$

Step 1:

NPs have been synthesized by PLAL tecnique[49,50].In general laser ablation is a physical synthesis method that permits to obtain highly pure spherical NPs in different media[51,52]. The mechanism of "laser ablation" depends on the type of laser used and on the topographic, optical and thermodynamic characteristics of the target[53,54]. When the pulsed laser radiation is absorbed by a solid surface, the electromagnetic energy is initially converted into electronic excitation energy and, subsequently, into thermal, chemical, photo-emission and mechanical energy.

When the incident beam has high energy, as in the case of a pulsed laser, it can be obtained the depletion of the material, the target that absorbed the light energy can release the energy by the expulsion of the material that constitutes it. The phenomena involved are evaporation, ablation, plasma formation, and "exfoliation" of the solid. The "evaporated" species form the so-called "plume", that is a mixture of energetically excited species consisting of atoms, molecules, electrons, ions, clusters, solid micro-particles and spherical particles in the molten state[55].

Immediately after laser irradiation, the "plume" expands rapidly from the surface of the target into the surrounding environment with the formation of a jet of matter that behaves according to the hydrodynamic laws of fluids. As the temperature of the plasma decrease, the aggregation of the metal atoms starts and the NPs is formed. Because spherical particles are mainly observed for low melting temperature materials and Ag have a melting temperature of 961 ˚C the only shape obtained by PLAL of an Ag target is the sphere.

AgNPs have been obtained by the ablation of a Silver metal[56] target in water containing trisodium citrate (TSC) 10 mM, using the first harmonic, 1064 nm wavelength, of a Nd:YAG pulsed laser with 10 Hz repetition rate and 6 ns of pulse duration for 20 min with a laser fluence of 1 J/cm$^2$. In figure 27 is reported the schematic of the experimental setup.

Step 2:

The second step of the process is the reshaping process. The spherical NPs are reshaped into anisotropic NPs by adding 30% w/w hydrogen peroxide ($H_2O_2$) to reach a concentration of 10 µl/ml under LED light irradiation for 6 h. Two different sources of light have been used for the irradiation, one monochromatic 580 nm, and one white polychromatic. Considering the strong interaction between NPs and light, it's expected that the two different sources of light will modify the shapes, and so the SP resonance, differently.

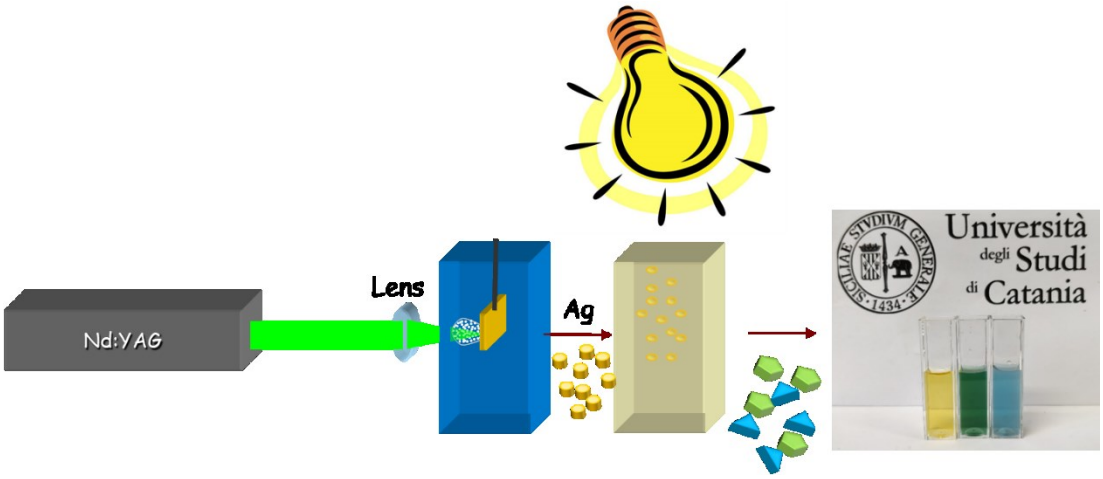


***Fig 27:*** *Experimental setup of the reshaping process*

### *2.7 Chemical-Physical features of "green reshaped" NPs*

In figure 28 is reported the UV-Vis characterization of Ag spherical NPs produced by PLAL as expected they present the typical resonance peak centered at 395 nm. Figure 29 shows the spectra of the two colloidal solutions reshaped with the monochromatic and polychromatic light. As it's possible to see, the plasmon resonance of an as-prepared spherical Ag NPs it's compared to the reshaped silver colloid. After 6 h of irradiation, the spectrum drastically changes. First, when the as prepared colloids it's irradiated with white light two new peaks appear at 475 nm and 620 nm due to the formation of new nanostructures as shown later in the SEM images. The peak relative to the initial spherical Ag NP is still present, but it is red-shifted to 412 nm and broadened, due to the increased size of such nanoparticles. Instead, when the starting colloid is irradiated with monochromatic light (580 nm) the peak at 412 nm completely disappeare and the spectrum become the same as that of Silver Nanoplates. The disappearance of the peak at 412 nm, associated with bigger spherical nanoparticles, can be associated with the disappearance of any spherical structure. This spectroscopically information indicates that the as-prepared spherical NPs are reshaped in a new bigger and sharpener shape.

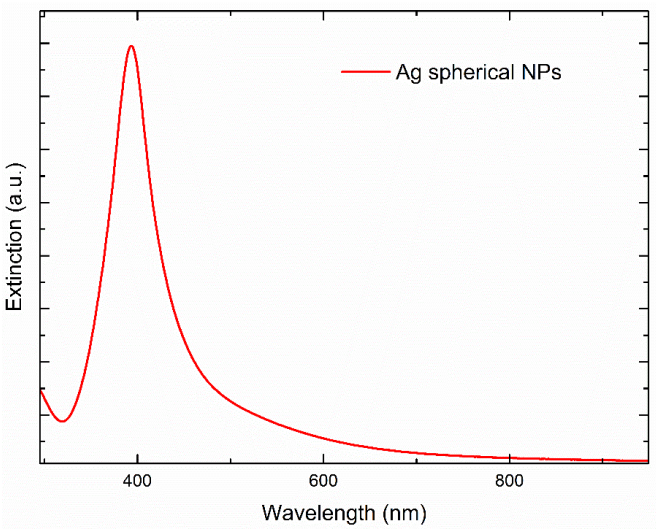


***Fig.28:*** *UV-VIS spectrum of AgNPs synthesized by PLAL method*

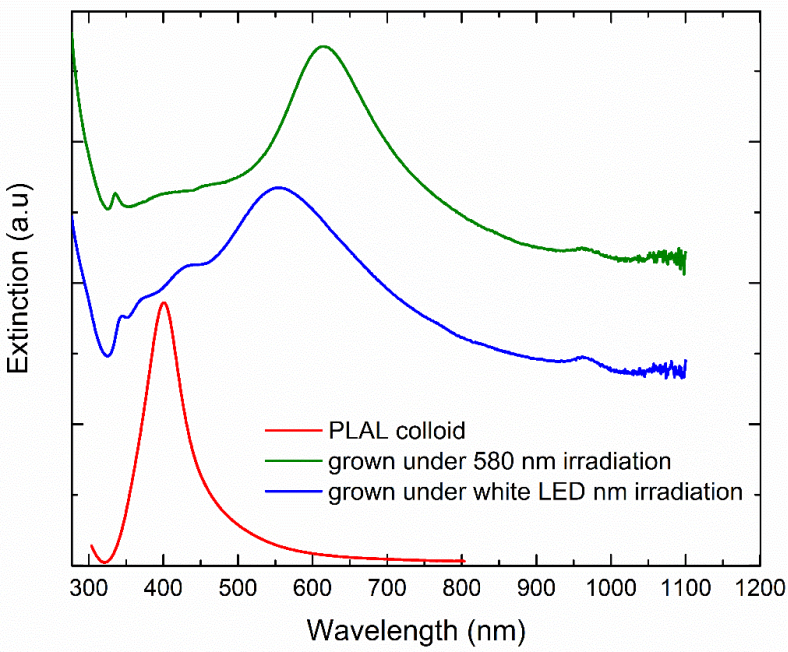


***Fig. 29:*** *Extinction spectra of Ag NPTs produced by reshaping process*

This is possible thanks to the combined action of light of a specific wavelength and a source of active oxygen. In this case, as Oxygen source $H_2O_2$ have been used. $H_2O_2$ oxidatively etches the Ag NPs forming $Ag^+$ ions[57] that are used for the growth of the new anisotropic nanostructure in a seed-mediated growth like process. Figure 30 shows that the reshaping process also takes place under irradiation only, without the addition of $H_2O_2$. However, figure 30 suggests that this process is limited to some extent. Then the $H_2O_2$'s ultimate role is to accelerate the process and eventually bring it to completion.

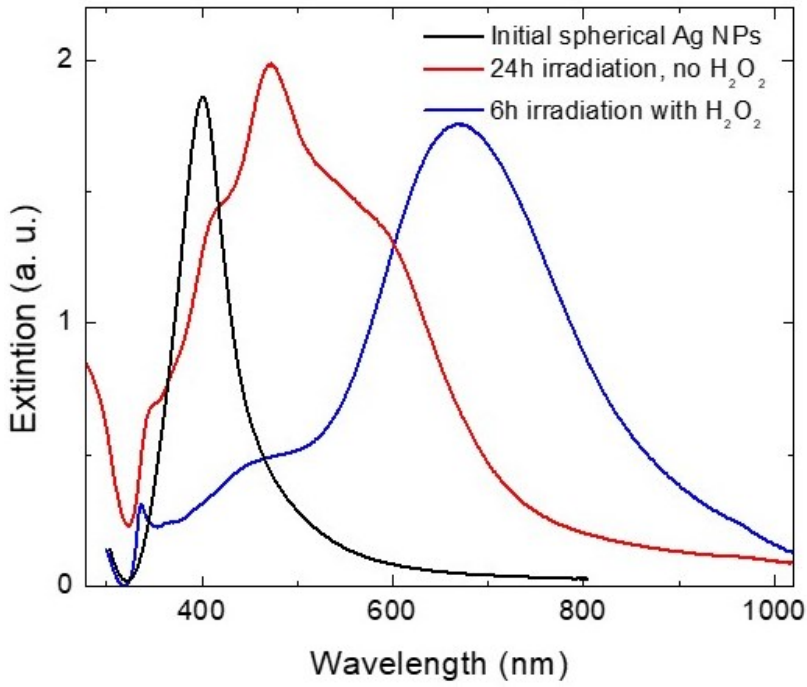


***Fig. 30:*** *Extinction spectra of Ag NPTs produced by reshaping process without $H_2O_2$*

Indeed $H_2O_2$ acts simultaneously as facet selective oxidizing etchant and as reducing agent for metallic nanoparticle as shown in the following set of chemical reactions [57,58] :

Oxidizing reactions

$$Ag^+ + e^- \rightarrow Ag$$

$$H_2O_2 + 2e^- \rightarrow 2HO^-$$

$$2Ag + H_2O_2 \rightarrow 2Ag^+ + 2HO^-$$

Reduction reactions

$$H_2O_2 + 2HO^- \rightarrow 2H_2O + O_2 + 2e^-$$

$$H_2O_2 + 2Ag^+ + 2HO^- \rightarrow 2Ag + 2H_2O + O_2$$

However, the equilibrium between the total oxidation of nanoparticles and their partial oxidation/reduction in the reshaping process is very delicate. The free citrate ions indeed also contribute to the reduction of $Ag^+$ under light irradiation according to the equations[59]:

$$\text{Citrate} + \lambda \rightarrow \text{acetone-1,3-dicarboxylate} + CO_2 + H+ + 2e^-$$

$$2Ag^+ + + 2e^- \rightarrow 2Ag$$

Because the absence of TSC significantly affects the process by dramatically dropping the yield of nanoplates, this process is one of the keys in aiding the

mild reducing action of $H_2O_2$[48]. Also, the irradiation of the solution may set the equilibrium between total oxidation and reshaping process. Radiation of appropriate wavelength, indeed, can excite metal nanoparticles. This excitation generates an intense Electromagnetic field near the surface of the NPs. The generated field, furthermore, causes the aggregation of the NPs does increase the probability that two nanoparticles collide to form a new structure. However, these are not the only two phenomena that occur when AgNPs are excited by light. The light, in fact, is also adsorbed by Ag aggregates and converted efficiently to thermal energy, which can drive the equilibrium towards the partial oxidation/reduction, and in addition, induce coalescence of different NPs to generate bigger nanostructures.

### *2.7.1 Size and shape features of green reshaped NPs*

In figure 31, it's reported an SEM image of Ag spherical NPs monolayer.

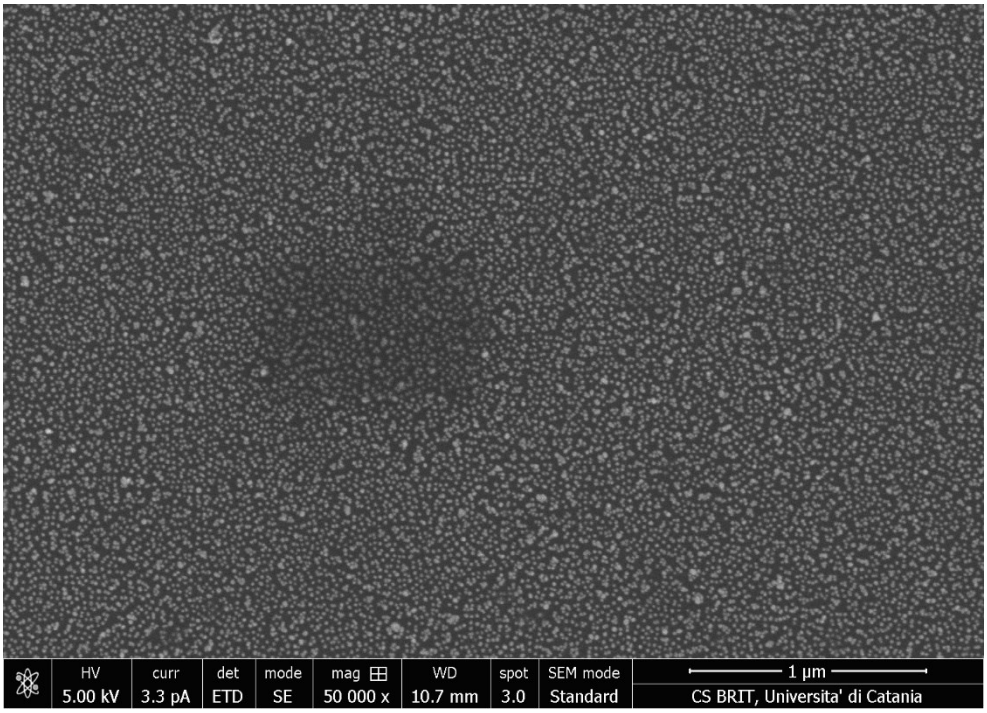


***Fig. 31:*** *SEM image of Ag spherical NPs monolayer on Si*

From the SEM image, it's clear that the mean dimension of AgNPs is circa 5-7 nm.

Figure 32 (A, B) show respectively, Ag nanostructure reshaped by light irradiation of 580 nm and polychromatic light. From figure 32 (A) demonstrate that using a monochromatic light source of 580 nm allows obtaining the same results obtained by the seed-mediated growth. Comparing in fact, SEM image in figure 19 and SEM image in figure 32 (A) is clear that both NPTs," chemical" and "green one" shows the same triangular shape; the only difference is the dimension that for "green NPs" is 109 nm, that in the can be likened to "chemical" NPTs with SP resonance at 613 nm grown with 350 µl. The resonance peak of "green" NPTs in fact, is at 620 nm as shown in

figure 29. Figure32 (B), in contrast, shows that the use of polychromatic light, generate different type of nanostructures like Ag nanostar, Ag NPTs, and Ag nanodisk. This shows that the effect of light is of great importance not only in promoting the oxidation/reduction process but also in directing growth thanks to the excitation wavelength and the induced electromagnetic field. This can be explained considering that the electromagnetic field generated by the light could redistribute charge on different areas of the surfaces, to either facilitate or inhibit particle-particle fusion in preferential direction[60] depending on the wavelength of the light.

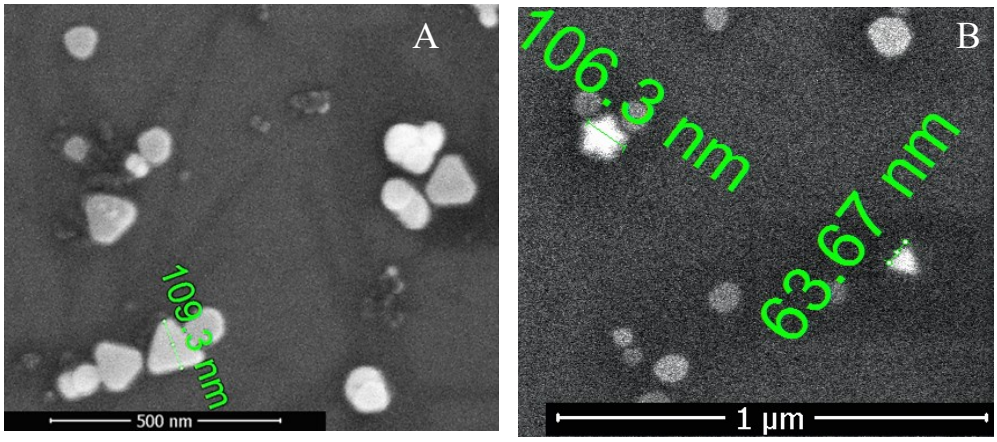


**Fig. 32:** *SEM image of Ag NPTs produced by light reshaping using(A)monochromatic source, (B) polychromatic source.*

### *2.8 NPTs Monolayer production*

To study the morphological properties of NPTs, bust most to study their chemical-physical properties and sensing features, in this work were prepared

monolayer of NPTs on a different substrate. Is to note that all SEM and AFM images are of monolayer produced as follow.

To produce monolayer, two different methods were used. The first consist in the functionalization, with green chemicals, of nanoparticle so they can self-assemble on the substrate. Thank to this method it is possible to produce a self-assembled monolayer on a wide range of hydrophobic substrate[61]. But the functionalization of the NPs surface could influence their sensing capability because the functionalization covers the surface of the NPs. The NPs functionalization has been made as follow:

1. 10 mL of Polivynilpirrolidone (PVP) of a 2 mM (PVP) solution were added to 25 mL of silver colloid under strong stirring condition.

2. 0.3 mL of an ascorbic acid solution of a 100 mM ascorbic acid solution. Were added into the NPTs and PVP solution leaving the solution under strong stirring condition for 10 minutes.

3. As of last stage of the functionalizing process glass slides, silicon wafers, or polymeric substrates with hydrophobic surfaces were cleaned using detergent and deionized water in sequence and then dried. The cleaned substrates, without any need for further surface modification, were immersed vertically into the colloids for approximately 20 h. Single-layer of NPs then uniformly self-assembled on the surfaces of the substrates.

The second methods it's a typical silanization process of a silicon substrate. With this method is possible to avoid the functionalization of the NPs surface thus leaving the NPs chemical-physical properties unchanged. Furthermore, is easier to have control of the assembling process through the experimental

conditions. But this method can be applied only on Silicon substrate and it's more complex. The process consists in:

1. The first step is cleaning the Silicon substrate to eliminate any organic pollutant on the surface with Piranha solution ( $H_2O_2$: $H_2SO_4$ 1 : 3 v/v) for 30 min. at 80° C.
2. Then the cleaned Silicon substrate was immersed for 15 min. in a solution of 10% (v/v) of 3-aminopropyl-tri-ethoxy silane (APTES) in Iso-propanol in presence of 1%(v/v) of Acetic Acid.
3. The substrate then was rinsed in isopropanol and water and submerged in the colloidal solution for 15 min. After this time the substrate it's ready to be dried and characterized.

In figure 33 there's a schematic of the PVP functionalization and silicon functionalization.

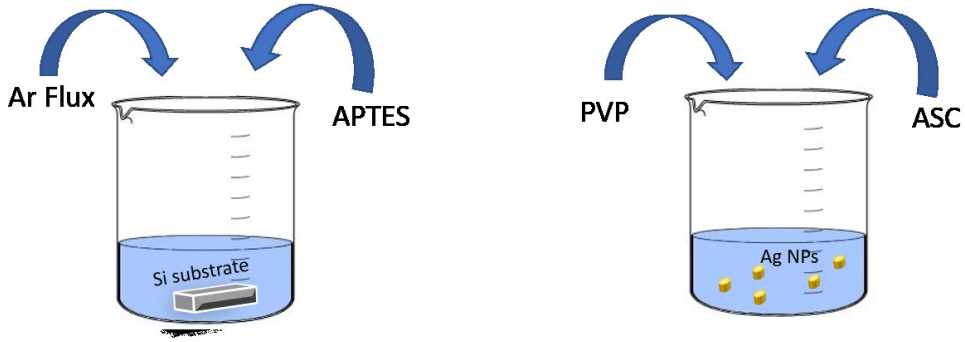


***Fig.33:*** *Left schematics of silicon functionalization, right functionalization of NPs both functionalization permit to obtain a SAM.*

### *2.9 Sensing capability of AgNPs*

Here it's reported the study of the sensing capability in terms of DS and EF of the different AgNPTs produced. As the aim of this work is to find the best chemical-physical parameters in terms of size shape and SP resonance, that are required to obtain an NPs with enhanced sensing features, a comparison between the NPTs synthesized with the seed-mediated growth method and with the reshaping method will be presented. This comparison will allow understanding the effect of the synthetic byproducts and the surface purity of the NPs on their optical properties.

#### *2.9.1 Dipole sensitivity experimental condition*

To prove the potential use of AgNPTs for plasmon sensing application it is fundamental to determinate how the position plasmon resonance ($\lambda_{max}$ ) shift with the refractive index of the media. As said in Chapter 1, in fact, the position of resonance depends in addition to the type of metal, shapes, and dimensions, also from the chemical surrounding near the NPs surface. An increase in the medium RI results in a more negative value of $\varepsilon_r$ to satisfy the plasmon resonance condition (equation 21), resulting in a redshift of the resonance peak. The Dipole sensitivity of silver nanoparticles was evaluated by plotting the shift of the plasmonic bands wavelength position ($\lambda_{max}$) against the refractive index. As predicted from theory the plasmonic resonances were found to linearly redshift as the solvent refractive index increase. Linear regression analysis of this data allows us to determine the DS. Generally, to test the dipole sensitivity of different metal nanoparticles, solvents having different refractive index are used[62,63]. However, this approach is affected by NPTs geometrical dependence on solvent nature. The change of solvent in

which the NPs are dispersed leads to the aggregation and precipitation of them. Moreover, the process of changing solvent could lead to the change of shape and dimension of NPs[63]. To overcome this limitation, in this work the refractive index of the solution was changed by adding 100µl of concentrated NPTs to different sucrose solution[64]. In particular, sucrose concentration varies from 0% To 60% thus changing RIU from 1.33 (pure water) to 1.44 (RIU) (60 % of sucrose) as reported in figure 34.

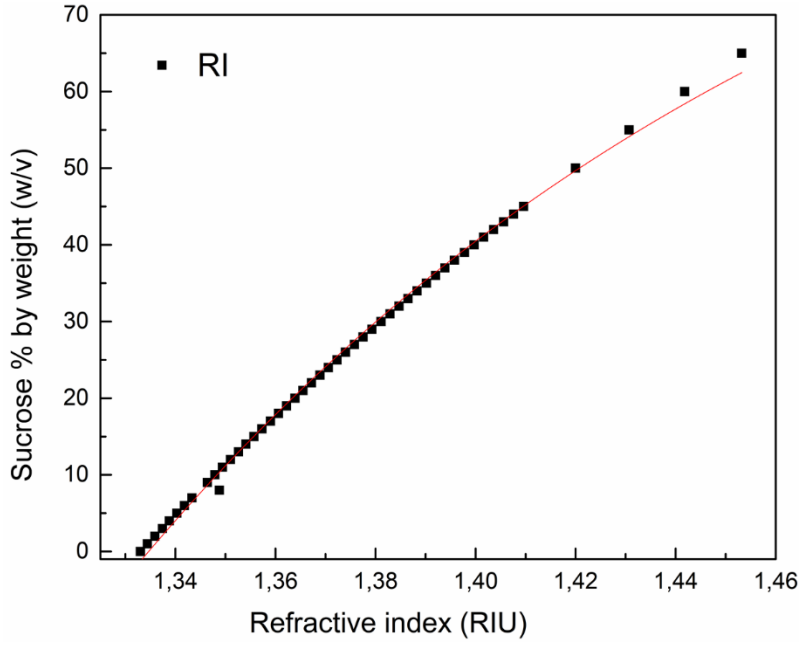


***Fig 34*:** *RI dependence on Sucrose percentage*

### *2.9.2 LSPR sensitivity evaluation*

The LSPR sensitivity of different AgNPTs colloids was evaluated. Specifically, the colloids have been grown with 20, 80,160, and 350 µl and the NPTs produced with the reshaping method. Is to note that below will be reported just the spectra for the NPTs grown with 20 µl and the confrontation between NPTs produced with reshaping process with monochromatic light, and the corresponding in terms of shape and dimensions chemically synthesized with 350 µl. The other spectra can be found in supplementary information (S10, S11,S12,S13). The following graphs show both the plasmonic spectra, of the said colloids, and the linear regression fit $\Delta\lambda_{max}$ ($\lambda_{water}$-$\lambda_{sucrose}$) in function of RI value.

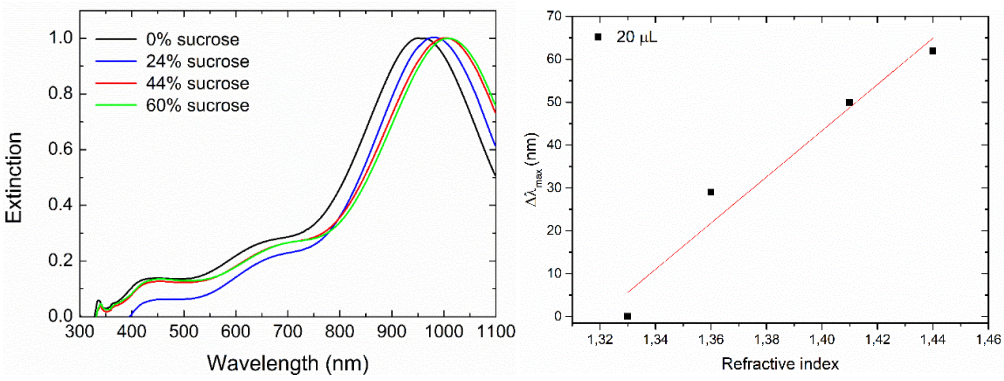


***Fig.35:*** *Extinction spectra of NPTS grown with 20µL of seeds with different sucrose solution, the plot of $\Delta\lambda_{max}$ in function of refractive index*

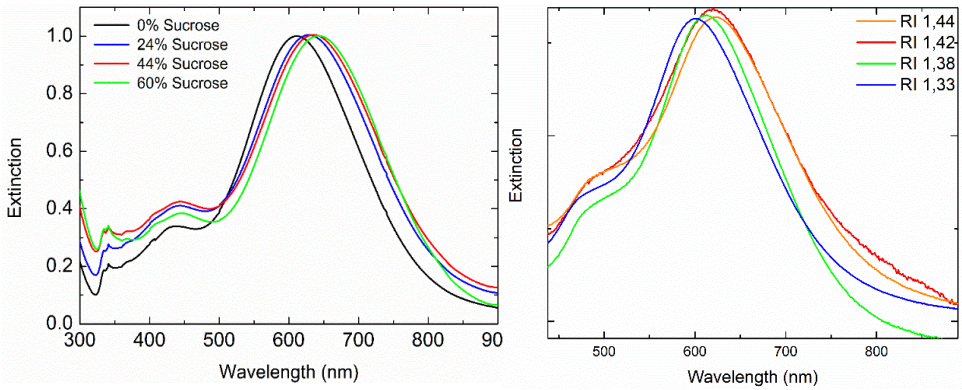


***Fig.36:*** *Extinction spectra of with 350µL of seeds left, right NPTs reshaped with 580 nm light with*

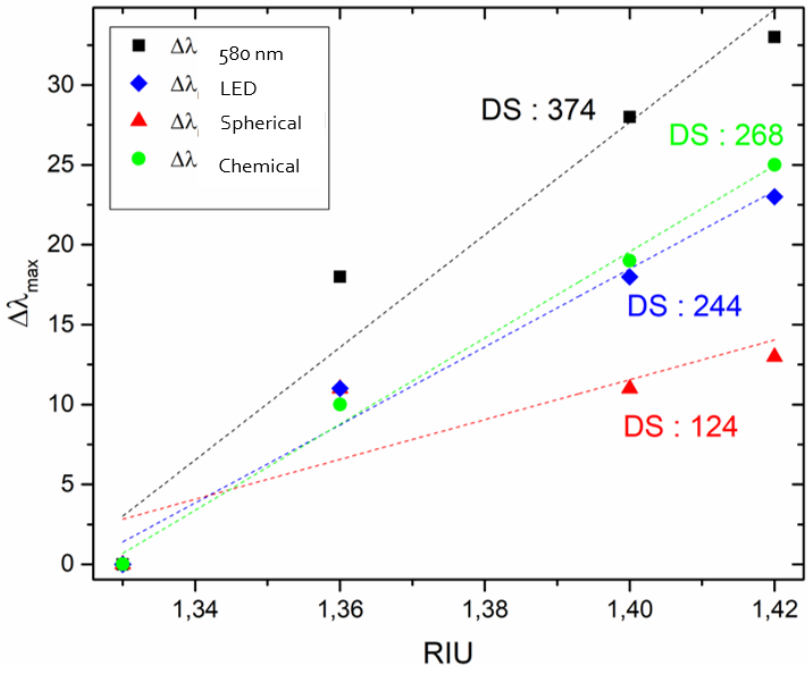


***Fig.36:*** *Confrontation between spherical AgNPs (red) and NPTs produced with a seed-mediated growth with 350µl(green) and reshaping method (blue and black).*

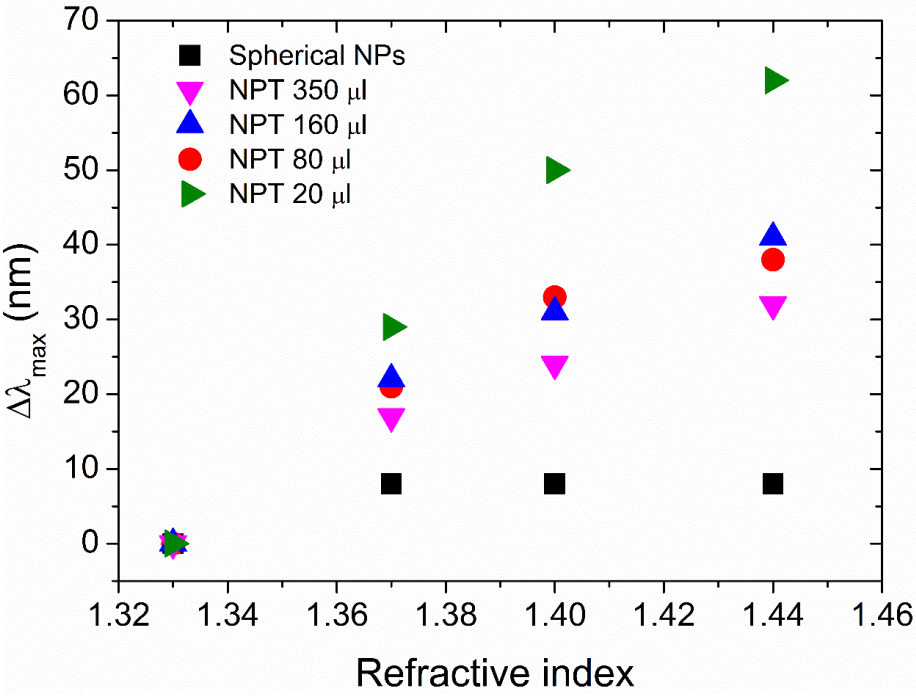


***Fig.37:*** *are compared the dipole sensitive of all colloids tested, to better understand the sensitive capabilities of the different colloids.*

| | *LSPR sensitivity (nm/RIU)* | *Dipole plasmon resonance(nm)* |
|---|---|---|
| ***20 µL*** | *449* | *1075* |
| ***80 µL*** | *367* | *905* |
| ***160 µL*** | *349* | *692* |
| ***350 µL*** | *286* | *613* |
| ***Reshaped with 580 nm LED*** | *374* | *620* |
| ***Reshaped with white LED*** | *244* | *520* |
| ***Spherical NPs*** | *125* | *400* |

***Tab.4:*** *LPSR sensitivity and of NPTs and spherical nanoparticles.*

Ag spherical NPs show a sensitivity of 125 nm/RIU. This is very low compared to other nanostructures made of the same metal. It is well known in literature[65] that the plasmon sensitivity of a nanostructure depends on different factors like size, shape, metal composition and so on. For the anisotropic NPs in fact, was found that the sensitivity of NPTs increased with the increasing of LSPR $\lambda_{max}$ and the Aspect ratio, reaching the maximum of 449 nm/RIU for the nanoplatelets grown with 20 µl and with an aspect ratio of 15 (Table 4). This can be justified by the increased dimension of the nanoplatforms which presents an extended surface and more shaped tips. The presence of shaped tips, in fact, give rise to an enhancement of the local electrical field near the tips (lightning road effect) itself that can provide a more sensitive response of the LSPR to the variation of refractive index. In addition, the presence of a larger surface, due to larger dimensions of NPTs, exposed to the chemical environment, increases the possibility of the nanostructure to detect variations in the surroundings, resulting in an augmented LSPR sensitivity. Regarding the green reshaped NPTs, the reshaping process dramatically enhances plasmon sensitivity. After 3h of irradiation (blue curve), with LED lamp, we derive a RI sensitivity value of 244 nm/RIU. Furthermore, if the monochromatic led is used as source of light, all the spherical particles are reshaped, and the value of RI sensitivity becomes three times higher than the value of the initial colloidal solution, reaching a value of 374 nm/RIU[66–68]. If this value is compared with the DS of the NTPs synthesized with the seed-mediated growth with 350 µl, which present the same position of the main resonance peak, as reported in figure 36 and table 4, it is clear the effect of the bi-products of the synthesis. The 350 µl, in fact, presents the value of DS of 286 nm/RIU which is lower respect the "green" synthetized NPTs. Considering that the position of the main resonance peak

as the size and shape for both NPTs are nearly the same, the enhanced sensitivity of the "green" NPTs must be determined by the difference in the synthesis method. The SP as already said; it is influenced by the chemical environment next to the surface of NPs, this obviously includes the synthesis by-products that remain bound to the NPs surface. A clean synthesis that does not produce by-products of reaction, therefore, allows synthesizing NPs with enhanced DS.

### *2.9.3 SERS enhancement factor evaluation*

As already said in Chapter 1 Raman spectroscopy is a powerful spectroscopy technique, that provides structural information on molecular structure, giving a molecular-specific signal that can be used for characterizing new molecule or to detect already know analyte but it's not very sensitive. To enhance the Raman signals can be used as a noble metal nanostructure as substrate in SERS technique. To evaluate the efficiency of enhancement of the different NPs in this work is used the EF as reported in equation 30. Practically, Raman intensity $I_{RS}$ of a concentrated solution of analyte $C_{RS}$ can be compared to the SERS intensity $I_{SERS}$ taken under identical conditions (i.e., same laser wavelength and power, same microscope objective). SERS experiments will start with the analyte in solution at a known concentration $C_{SERS}$ (usually much smaller than $C_{RS}$). In figure 38 is reported a schematic of experimental setup.

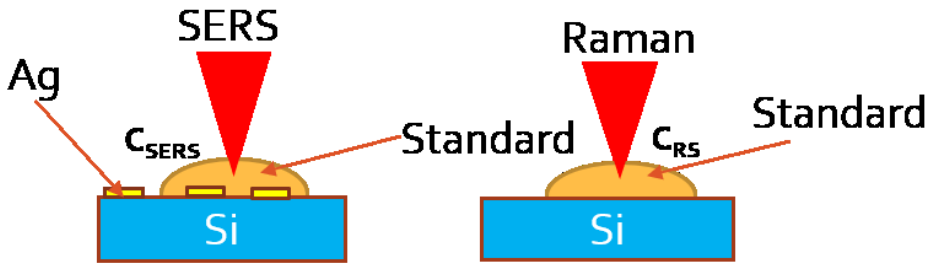


***Fig.38:*** *Experimental setup for EF evaluation. Left SERS measurement of a drop of glucose on a monolayer of AgNPs, right normal Raman spectra of a drop of glucose on a silicon substrate*

To study SERS EF, of the different substrate produced, different solutions of glucose were used. Glucose's a good standard molecule because is not toxic, cheap, easy to find, soluble in water and present well-defined Raman peak, moreover it is a biological interest molecule. (figure 39).

Experimentally two different solutions of glucose were prepared,

1. High concentrated 1 M for normal Raman measure, and
2. High diluted $10^{-7}$ for SERS measurements.

In figure 39 it's reported the spectrum for the 1 M glucose solution obtained by measuring a drop of glucose solution on a silicon substrate. For the measurement a 532 nm Laser was used with a power of 25 mW, using an objective of 50x magnification. The same experimental setup was used for the SERS measurements except for concentration of the solution and for the substrates used. The evaluation of the enhancement factor will be made by comparing the intensity of the peaks centered at 2942 $cm^{-1}$ which is due to glucose doublet, which is caused by C-H stretching vibration[69]

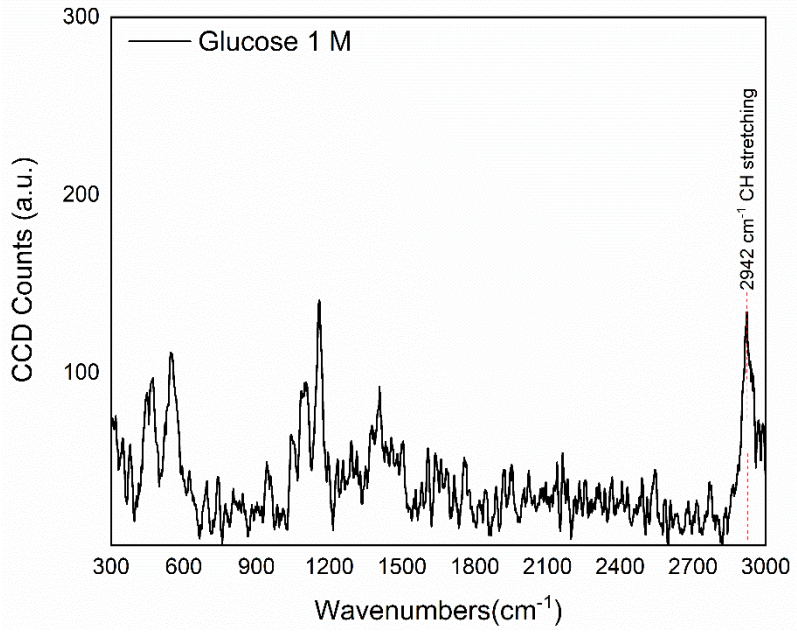


***Fig.39:*** *Raman spectra of Glucose solution 1M*

In figure 40 is reported the comparison between the intensity of peak at 2942 $cm^{-1}$ of normal Raman spectra of 1 M glucose solution and the SERS spectra obtained with NPTs synthetized with seed-mediated growth (Blue) and the reshaped one (Red).

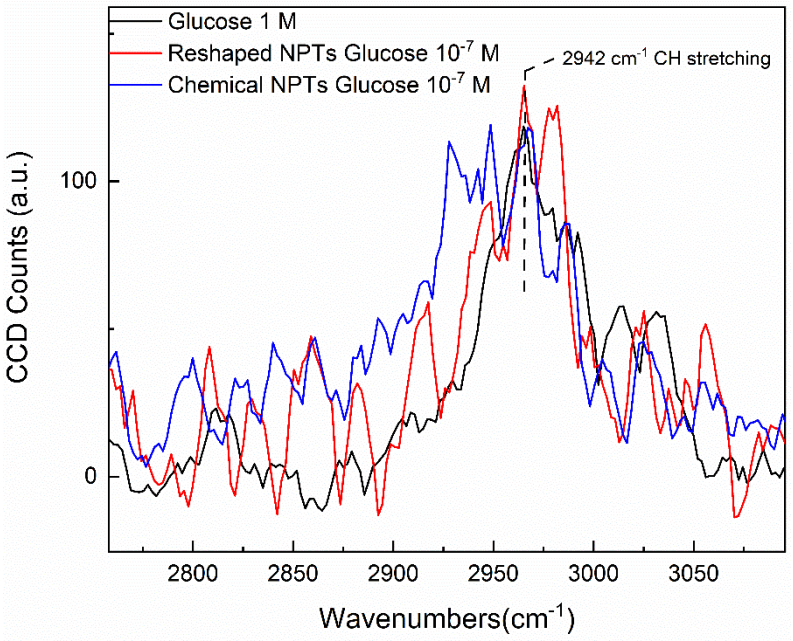


***Fig.40:*** *Confrontation of the intensity of peak at 2942 $cm^{-1}$ for the different Raman(black) and SERS (red and blue) spectra*

As in the case of DS, the NPTs produced with the green reshaping process present the highest SERS EF respect the chemicals one. Is to note that both NPTs present higher SERS EF respect classical spherical AgNPs. In literature, in fact, are reported value of $10^5$-$10^6$ for classical spherical NPs[70,35]. In table 5 are reported the value of intensity of peak at 2942 $cm^{-1}$ and the relative EF.

| **Substrate** | **Concentration(M)** | **Intensity(a.u.)** | **EF** |
|---|---|---|---|
| **Si** | 1 | 97 | / |
| **Chemical NPTs** | $10^{-7}$ | 88 | $9 \times 10^6$ |
| **"Green"NPTs** | $10^{-7}$ | 119 | $1.2 \times 10^7$ |

***Tab. 5:*** *Intensity value of peak centered at 2942 $cm^{-1}$ and relative value of EF*

The same motivation for the increased DS for reshaped NPTs can be invoked for the enhanced EF. So as a result of these two different sensing capabilities test, it's clear that sharpener tips and increased size produce an enhancement of the optical properties of NPs, due the so-called lightning road effect and for the augmented surface of NPs. Of a relevant impact on chemical-physical properties of NPs, it's the synthesis method from which depend not only the size and shape of NPs but also their surface purity. Is this latter, in fact, that give to NPTs produced in absence of chemicals enhanced optical properties.

## *Chapter 3*

### *3.1 Metal-oxide nanostructures*

Semiconductors, in contrast, to metals that present a continuous band, has a bandgap in its band structure. The conductivity of a semiconductor is dominated by electrons in the conduction band CB (n-type) or holes in the valence band VB (p-type) figure 41.

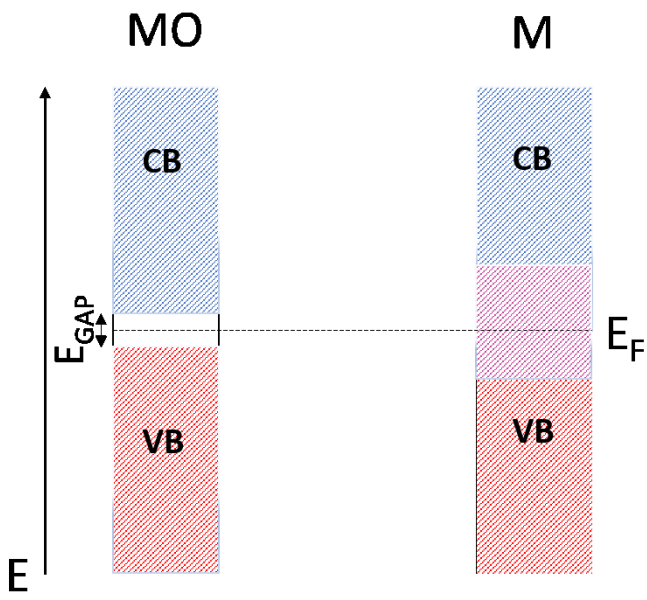


***Fig 41:*** *Example of CB and VB in metal oxide (MO) and in a Metal. The latter presents an overlapping of the two bands meanwhile the MO present an* $E_{gap}$ *between the two band.*

Only the light with higher energy than the $E_{Gap}$ can be absorbed by a semiconductor. As result of the light adsorption Electron-hole pairs can be generated. [71,72] Thanks to these properties semiconductor-based nanostructures have found wide applications in areas such as photocatalysis, photovoltaics,[73,74] photoluminescence[75,76], and photochromics[77,78].

As said before, the most studied and used semiconductor nanostructure in the field of catalysis and sensing are $TiO_2$ and ZnO. The reason for this interest of all scientific community resides in their unique properties. First, they are totally biocompatible, they are very cheap materials, high efficiency in charge separation and furthermore all these properties can be easily tuned by changing the dimension and structure of the nanoparticles. In this context ZnO and particularly ZnO NRs are used for a broad range of high-technology

application[79], ranging from surface acoustic wave filters, photonic crystal, photodetectors, gas sensors, Bio-sensors, Photocatalytic substrate and so on. One of the reasons for this multi-field application for this nanostructure it's the wide range of synthesis method that can be used to produce them. In this work ZnO NRs were synthesized, by MOCVD. As substrate for the growth were used a monolayer of Ag NPs, with the dual purpose of catalyzing the growth of nanorods to a specific direction[80] and to combine the Nobel Metal nanoparticles with the semiconductor nanostructures. The aim of this combination is to enhance the chemical-physical properties of both nanostructures thanks to the formation of the so-called Schottky junction.
Specifically, ZnO nanorods (NRs) with metallorganic chemical vapor deposition method (MOCVD) were grown on Silver NPs monolayer, trying to combine the two different materials. These new nanostructures thanks to their stability and enhanced properties can be used as a plasmonic platform for molecular sensing[66,81]or as catalytic substrate. The sensing capability of these structures has been studied by investigating their Surface enhancement Raman scattering (SERS) capability[81]. A little summary on catalytic efficiency of this structure is also reported.

### *3.1.1 Schottky junction*

When a metal comes in close contact with a semiconductor, at their junction interface an energetic barrier is formed. This barrier is the so-called Schottky barrier. The Schottky barrier blocks the electron transfer from the metal to the semiconductor and vice versa. Moreover, as a consequence of the formation of the metal/semiconductor junction, the $E_F$ of the semiconductor, that is lower in energy respect to that of metal, because of their larger work function, equilibrate with the $E_F$ of the metal. The critical parameter that determinate if

an electron could pass from the metal to the valance band of the semiconductor and vice-versa is the Schottky barrier height. The heights value depends on the semiconductor type specifically if is a p or n-type semiconductor. Considering that in this work are reported two n-type semiconductor just this latter case is defined. The Schottky barrier $\Phi_B$ for an n-type semiconductor is measured from the conduction band edge to the vacuum level as shown in figure 41 bis and is defined as the difference between the work function metal-vacuum of the metal and the semiconductor-vacuum electron affinity. If electrons possess energy > respect the $\Phi_B$ they can be injected into the semiconductor or to the metal. The electron can acquire the necessary energy to pass the barrier in different ways, but the most interesting way for this work is the excitement of electrons due the light irradiation. The efficiency and the direction of the electron transfer depend on the wavelength of light used to excite the material[82]. When the wavelength of the exciting light, in fact, match the plasmon resonance condition, the electron transfer from the metal to a semiconductor can occur during the decay of the SPR. The excited surface plasmons, indeed, decay by either emitting a photon or generating an electron-hole pair[83]. The exciton pairs have larger energy than the carriers near the Fermi energy and are called "hot" carriers[83]. This "hot carriers" have enough energy to pass the Schottky junction. This phenomenon enhances the charge separation, with the highest charge density region at the interface metal/semiconductor.

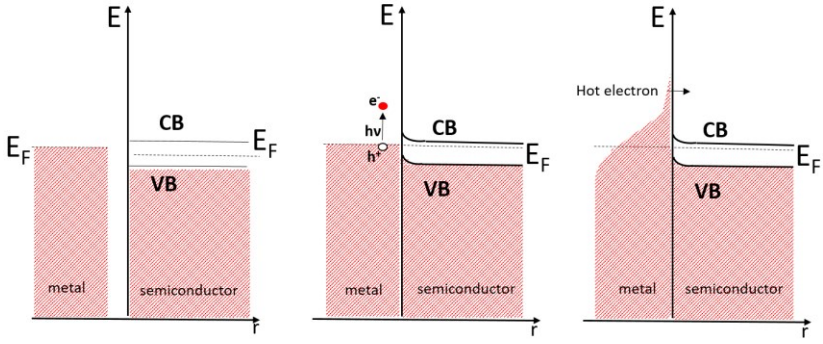


***Fig 41 bis:*** *Phenomena involved at the interface metal/oxide, in the formation of a metal/semiconductor junction, and in the electron transfer due the plasmon resonance.*

Thanks to this charge separation, the intensity of the electric field in the proximity of the nanostructure is magnified. As a consequence the Raman intensity of molecule in the near proximity of the interface will be proportionally increased due to the enhanced local *E*-filed[84] as already reported in chapter 1. This charge separation can be used also in catalytic field, in fact, when a semiconductor encounters these intense fields being, the electron-hole formation rate in a semiconductor proportional to the local intensity of the electric field, (more specifically to the square of the module | E |$^2$)[85,86], the formation rate of exciton pair consequently increases by some orders of magnitude. All these phenomena enhance the properties of both Metal a Metaloxide particles raising the sensing and catalysis efficiency.

### *3.1.2 Photocatalysis*

Photocatalysts are almost exclusively semiconductors. The absorption of a photon by a photocatalyst, for example, $TiO_2$ of a suitable wavelength, with energy greater than the bandgap, determines the promotion of an electron from the valence band (VB) to the conduction band (CB), thus generating what is called exciton. Excitons are a pair of high-energy charge carriers electron ($e^-$) hole ($h^+$), with a certain lifetime which depends on the chemical-physical characteristics of the semiconductor considered, with respectively oxidizing and reducing properties.

$$\text{photocat.} + h\nu \rightarrow h+ + e^-$$

These excitons can evolve according to three different processes[87]:

1. Instantaneous recombination of the electron-hole pair and thermal dissipation of the absorbed energy.
2. Migration of holes and electrons towards the surface of the catalyst from the valence and conduction bands respectively;
3. Redox reactions at the semiconductor surface (interface): the holes in the valence band can oxidize the molecules of the donor (for example polluting), while the electrons of the conduction band can reduce the molecules of the electron acceptor (for example the H+ of hydrogen water).

$$D + h+ \rightarrow D^+$$
$$A + e^- \rightarrow A^-$$

The last point is possible only if the migration described in point 2 occurs; moreover, only if the charge carriers separate from each other for sufficiently long times they can be used to carry out catalytic chemical transformations in the active sites at the semiconductor/liquid interface. For example, in water, the hole will oxidize it, into hydroxide radical ($OH^{\cdot}$), while oxygen will act as an electron acceptor transforming itself into superoxide radical ($O_2^{\cdot}$).
These intermediates being highly reactive will, in turn, react, for example with the target molecules (air and water pollutants), degrading them[88].

### *3.2 ZnO NRs synthesis by MOCVD*

The classical synthesis of ZnO NRs by MOCVD start from the deposition of ZnO buffer Layer on silicon substrate[89]. The deposition is performed in a tubular hot wall furnace (Fig 4).

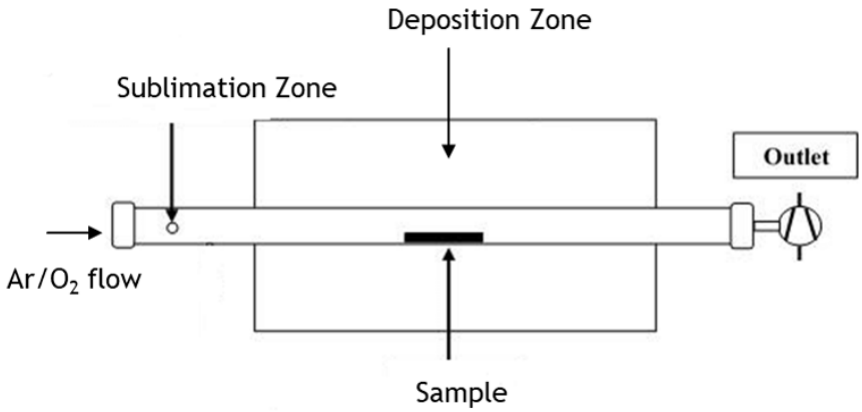


**Fig 42:** *CVD tubular reactor*

As metallorganic precursor has been used (N,N,N′,N′-tetramethylethylenediamine) (TMEDA) adduct of Zinc(II)bis(2-thenoyl-

trifluoroacetonate) [Zn(tta)2•tmeda][90] . The process it's composed of two steps:

1. Deposition of ZnO buffer layer. The temperature of deposition was set at 600°C and the time of deposition was 60 minutes. Ar (250 sccm) an $O_2$ (250 sccm) have been used as the carrier and reactive gas.
2. The second step it's the growth of ZnO NRs on preexisting ZnO layer at the same experimental condition.

In this work three different substrates for the growth process were used:

- Silicon
- A monolayer of Ag NPs on Si
- A monolayer of Ag NPTs on Si

In the case of the two monolayers substrate, the growth of ZnO NRs takes place in a single step catalyzed by the presence of Noble Metal NPs.

It's well known in literature the catalytic process for the growth of ZnO Nanorods by MOCVD[80,89,90]in presence of NPs of noble metal, like Au or Ag, used as catalysts. During the catalytic MOCVD growth, Zn precursor vapor solubilizes into the metal catalyst, that at high temperature fuse, does form an alloy droplet. After saturation into the fused metal, Zn precipitates and start to build up until it comes out of the droplet. In presence of the reactive gas $O_2$ ZnO that start to growth is oxidized does form ZnO NRs. An interesting side effect of the catalyzed process is that: during the growth process, ZnO NRs start to grow under the metal droplet dragging the metal catalyst with it. For this reason, at the end of the growth process, metal catalyst droplet can be found on the tips of the NRs. Being this droplet partly fused with the MO below and exposed to the environment it can be used as nanoplatforms for enhanced sensing or catalytic application.

### *3.3 ZnO NRs morphological Characterization*

Here is reported the SEM image of ZnO nanostructure obtained by growing in a single step by MOCVD technique on a different substrate. In order, are shown: Si substrate before and after the MOCVD process, Ag spherical and triangular NPs substrate before and after MOCVD.

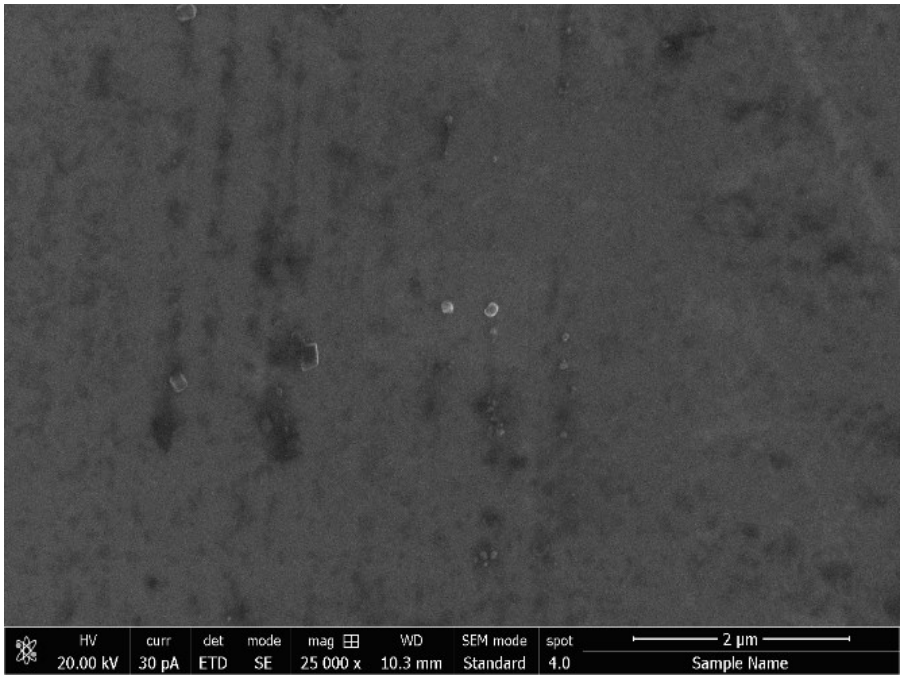


**Fig. 43:** *SEM image of Si substrate before the MOCVD process*

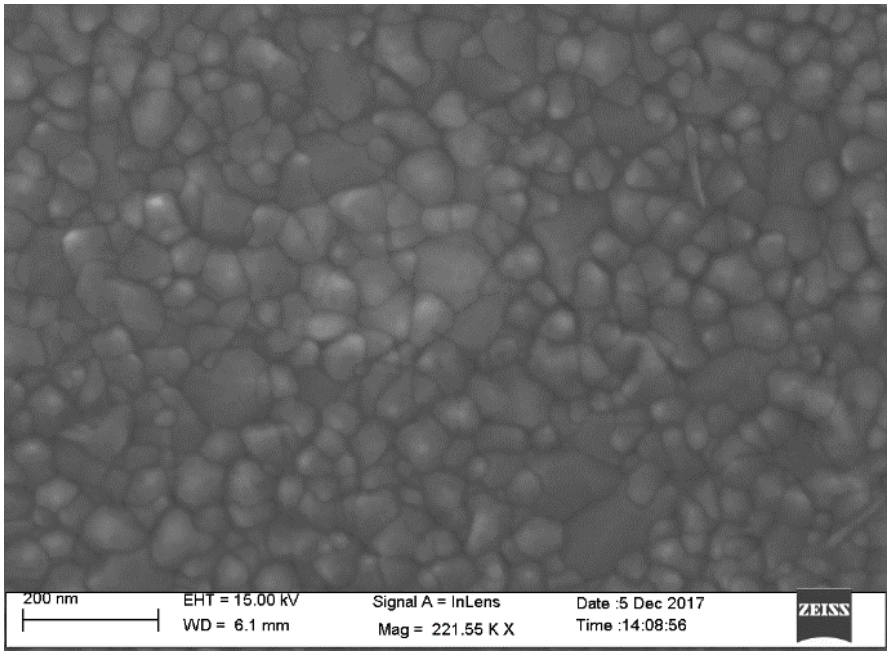


**Fig. 44:** *SEM image of Si substrate after ZnO MOCVD deposition it is clear the formation of a layer of ZnO*

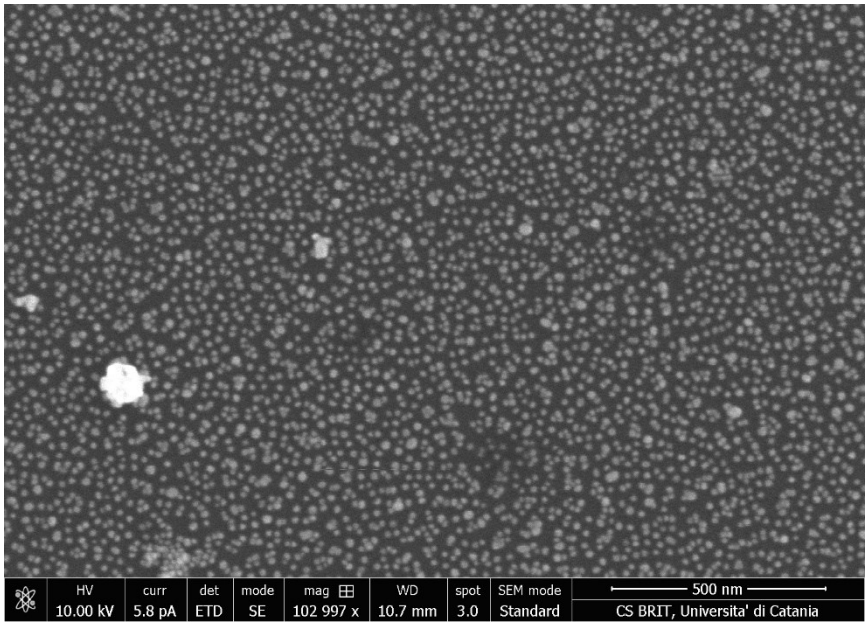


***Fig. 45:*** *SEM image of Ag spherical NPs monolayer on Si*

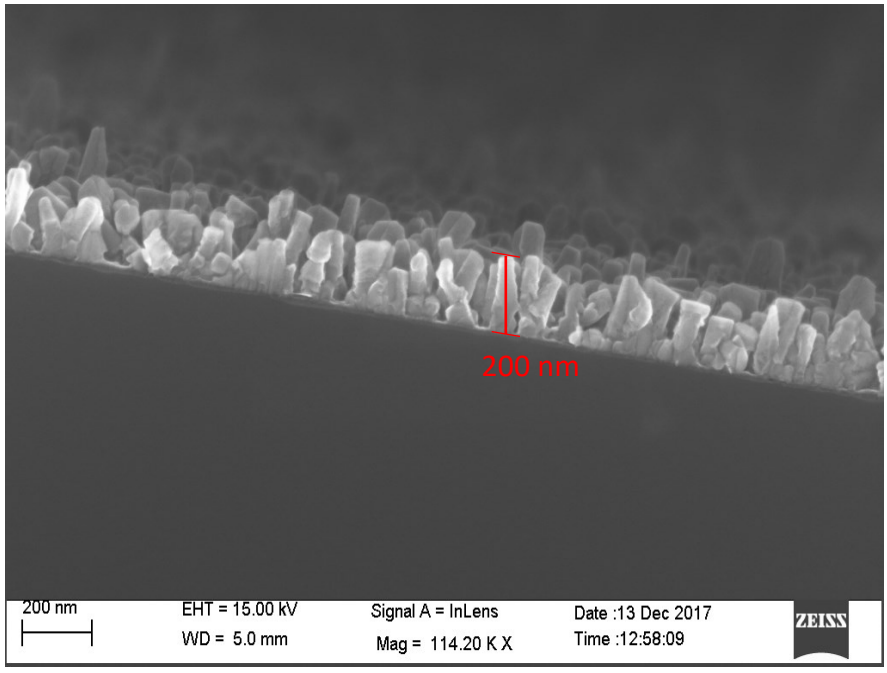


***Fig. 46:*** *SEM image of Si substrate functionalized with spherical Ag NPs after ZnO MOCVD deposition.*

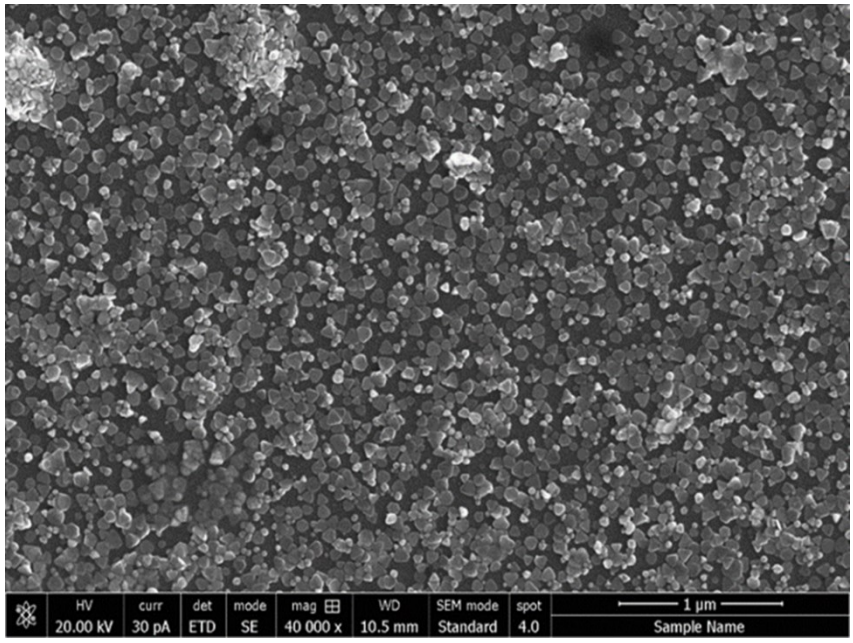


***Fig. 47:*** *SEM image of Ag NPTs monolayer on Si*

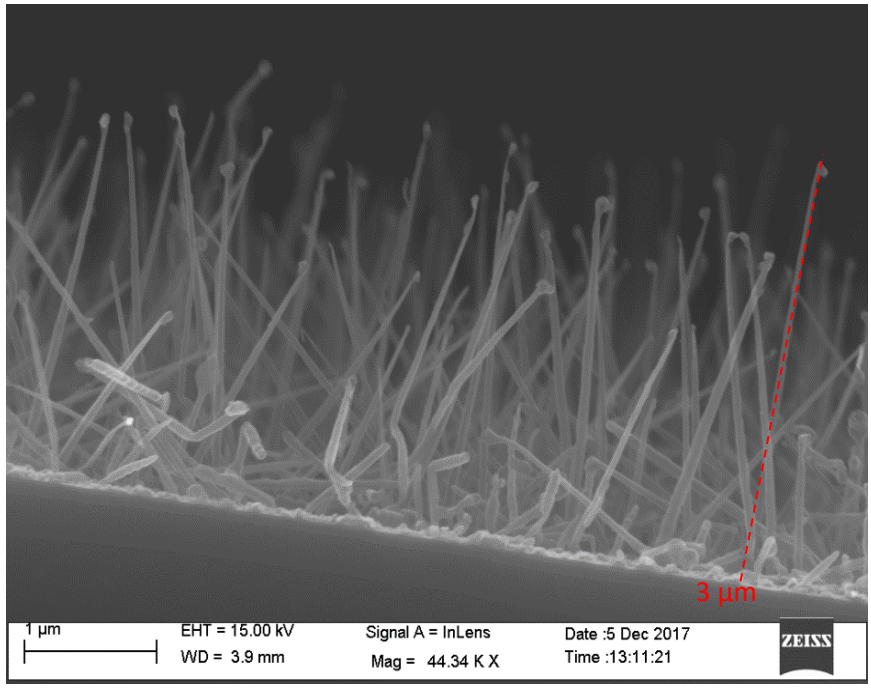


***Fig. 48:*** *SEM image of Si substrate functionalized with spherical Ag NPTs after one MOCVD process*

In figure 44 the absence of any buffer layer on Si substrate produces, after the MOCVD process, a layer of ZnO on which it's possible to grow ZnO NRs with a second MOCVD process.

Figure 46 shows what happen when a layer of Ag spherical NPs is used as a substrate for the growth process. In this case, it's clear that after one MOCVD process the ZnO NRs are already present. The NRs shows a typical hexagonal and defective structure, and their length t's about 200 nm. However, the most interesting and a-typical structure is shown in figure 48. These structures are obtained by using as starting layer AgNPTs. As it's possible to see from the SEM image the ZnO NRs are totally different from the classical one. First, they are elongated approximately 3 μm and highly oriented, they are also very thin as it's can be deduced from the transparency of the structure. A very interesting feature it's the presence on the tips of a spherical-like structure. XRD analysis confirmed the presence of silver in the sample. To better show the feature of this nanostructures others SEM image for this sample are reported. From this SEM image (figure 49), it's possible to see that the growth process has taken place on the whole surface rich in NPTs (figure47), moreover this growth is homogeneous in terms of structures and dimensions on the whole substrate. In figure 50 is reported a zoomed image of these nanostructures. Is it clear from this image that the nanostructures are not real nanorods but nanotubes. They, in fact, are empty inside.

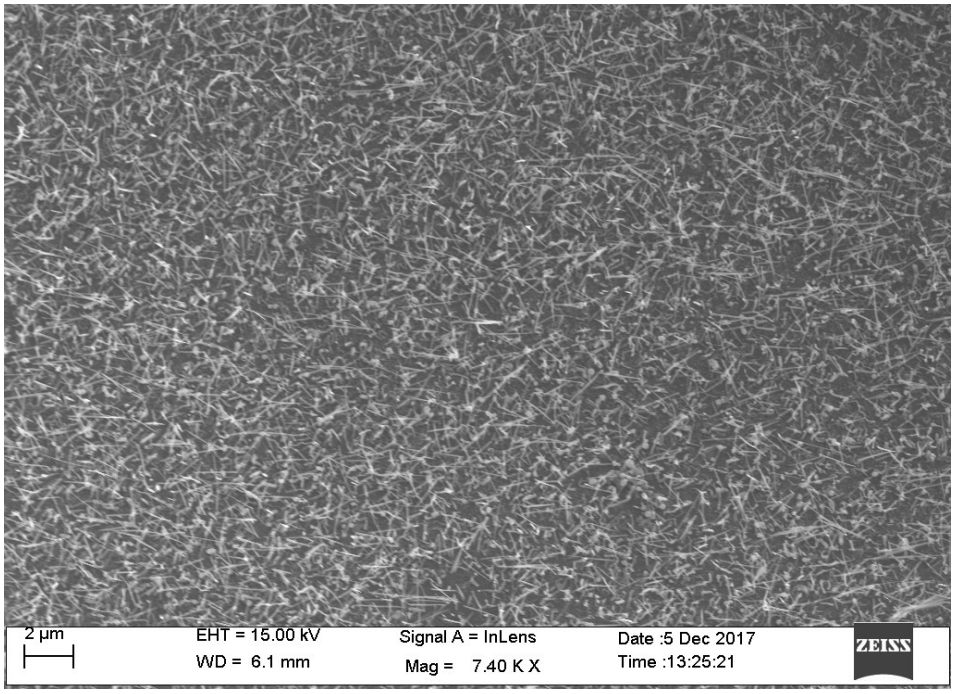


**Fig. 49:** *SEM image of ZnO nanotubes grown starting from a AgNPTs monolayer*

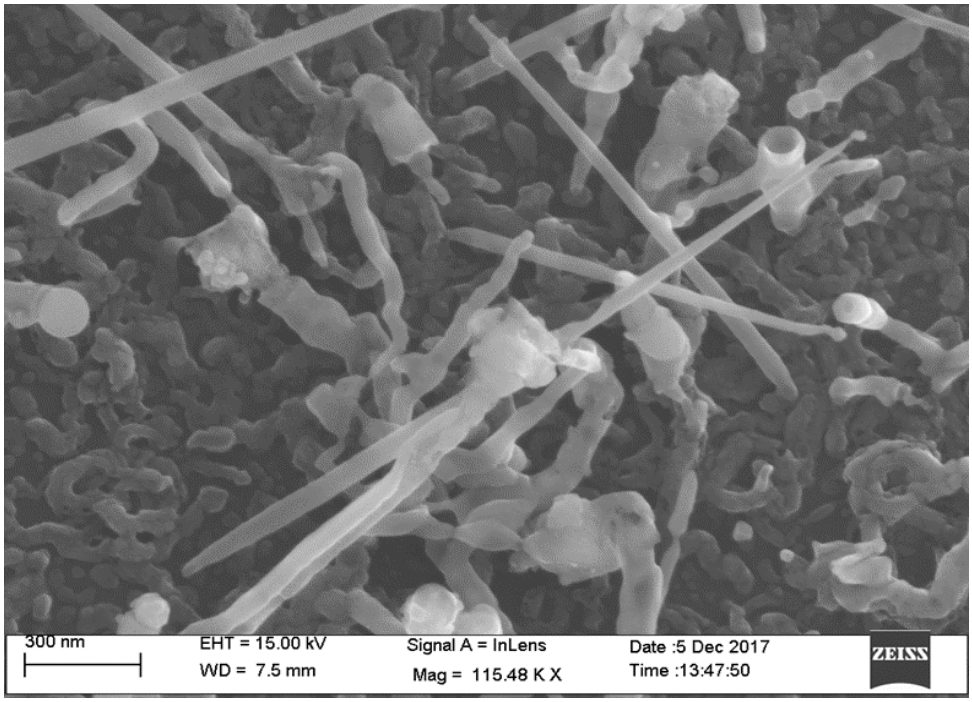


**Fig. 50:** *SEM image details of ZnO nanotubes grown starting from a AgNPTs monolayer*

### *3.4 ZnO NRs Optical properties*

Figure 51 report the reflectance spectra for the sample studied and the value of the Energy BG calculated from the Tauc plot. Typically, a Tauc plot shows the quantity hν (the energy of the light) on the abscissa and the quantity $(\alpha h\nu)^{1/r}$ on the ordinate, where α is the absorption coefficient of the material. The value of the exponent r denotes the nature of the transition. The resulting plot has a distinct linear regime which denotes the onset of absorption. By

fitting the linear area of the plot, we can obtain a more accurate value for the Energy BG. Is to note that the NRs grown with the NPTs as catalytic substrate shows the presence of the typical plasmon resonance for metallic nanoparticles does demonstrate the presence of Ag NPTs.

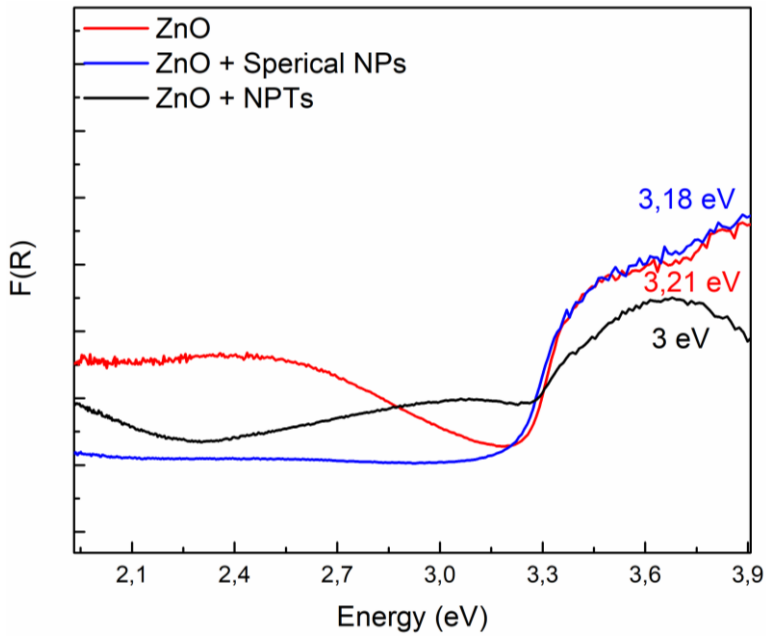


***Fig. 50:*** *Tauc Plot for ZnO NRs growth with NPTs, NPs and without catalyst.*

Moreover, from the SEM image, it is clear that the structure of the metallic catalyst strictly influences the structure of the nanorods. When Ag spherical NPs are used (figure 46,45), the ZnO NRs grow with the typical hexagonal structure. Otherwise, when Ag NPTs are used as substrate (figure 47,48), the ZnO grow in nanotube like structure. Although the mechanism of growth has not yet thoroughly investigated, however is possible to understand the growth of these hollow nanostructures assuming the fused Ag flows within the

growing nanostructure of ZnO until getting out of the tip, where are found the spherical-like Ag droplets (figure 48). It's to note that, the Bandgap decrease from 3,21 eV of ZnO to 3,0 eV for the NRs grown with AgNPT's. This finding could be interesting for employing this hybrid nanostructure in catalysis.

### *3.5. Raman analysis of the nanostructures*

To understand if the hybrid nanostructures present enhanced optical properties, a study of EF have been done.

Before determinate, the SERS EF the different ZnO NRs produced have been characterized by Raman spectroscopy. Is to note that as already said in Chapter 2 every monolayer has been prepared with the silanization and PVP functionalization methods. In figure 51,52, are reported the result of the Raman Analysis for two different ZnO grown on two different monolayers produced with silanization and PVP methods.

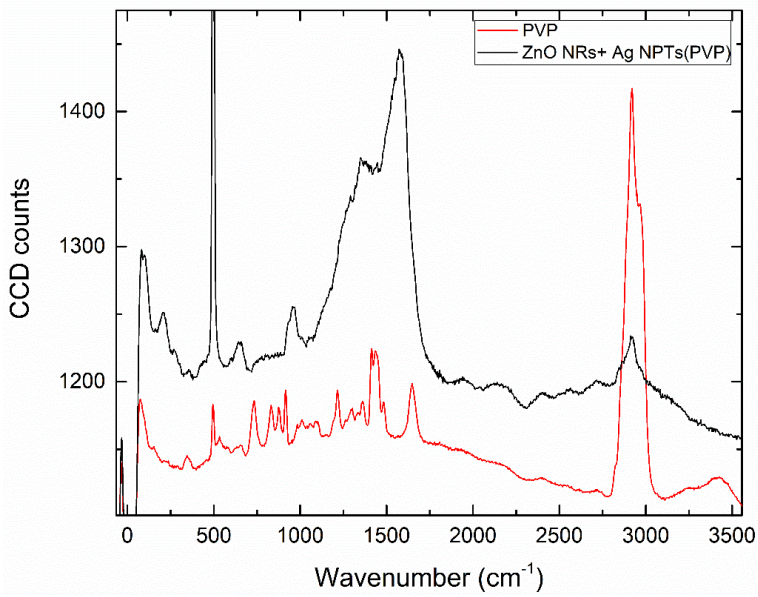


***Fig. 51:*** *Raman spectrum of ZnO NRs grown on Ag NPTs monolayer prepared with PVP*

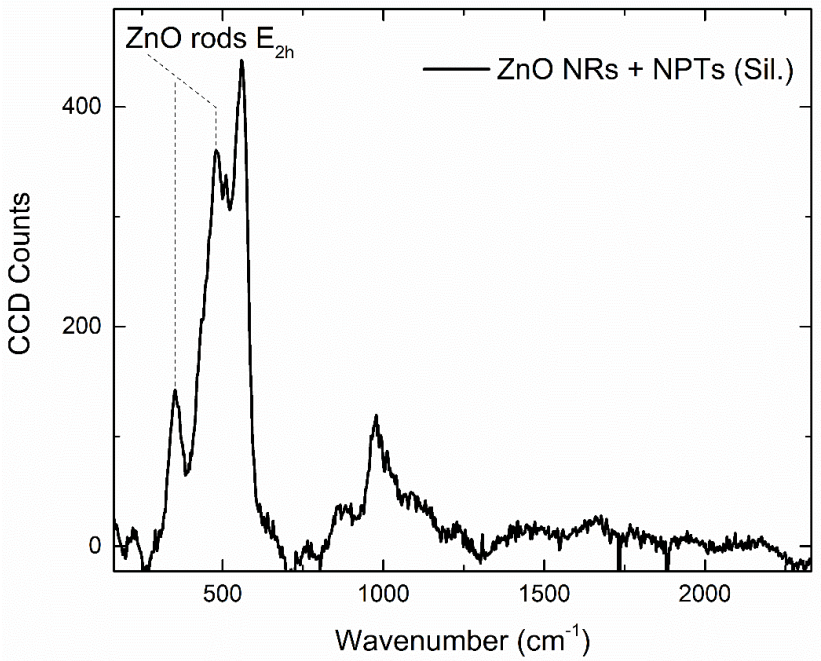


***Fig. 52:*** *Raman spectrum of ZnO NRs grown on Ag NPTs monolayer prepared with APTES*

In figure 51, it's reported the Raman Spectrum of the ZnO NRs grown on NPTs monolayer prepared with PVP and ascorbic acid and the Raman spectrum of PVP. As it's possible to see from the ZnO NRs spectrum there is a very big enhancement of the signal, but from the other hand, there are a lot of signals that can be attributed to the functionalization process. In fact, comparing the spectrum of PVP with the ZnO one, it's clear that the signals at about 1600 $cm^{-1}$, 2950 $cm^{-1}$, 1450 $cm^{-1}$, and 950 $cm^{-1}$ can be attributed to the PVP on the surface of Ag NPs used for the formation of the starting monolayer, on which the growth process take place. In this condition result very hard or impossible to use this platform as sensitive Raman substrate for

the detection of an analyte because the most typical signals lay in the region from[91] 900 $cm^{-1}$ to 2000 $cm^{-1}$.

Instead in figure 52, it's reported the Raman spectrum for the ZnO NRs grown on the silanized substrate. This sample is totally different from the other. The spectrum, in fact, doesn't show signals of the functionalization in the region of interest for detection. It's to note that, in this case, thanks to the more purity of the sample it's also possible to detect the typical vibration of ZnO NRs[92] at 482 $cm^{-1}$ and 353 $cm^{-1}$

For this reason, the SERS EF have been studied just for the sample prepared with AgNPTs and spherical Ag NPs monolayer prepared with the silanization process.

### *3.5.1 SERS EF evaluation*

The results obtained for the SERS experiments are shown in figure 53. To evaluate EF have been used the same identical experimental condition used for the evaluation of EF for NPTs in chapter 2. Here has been used in addition to glucose Rodhamin 6G to demonstrate that the EF doesn't depend on the molecule used. This molecule presents very intense and resolute vibrational picks that are not influenced by the chemical environments. To quantify the EF, two different solutions of RhD 6 G have been prepared. One 1 M used for normal Raman measurements. And the other $10^{-5}$ M used for SERS measurement.

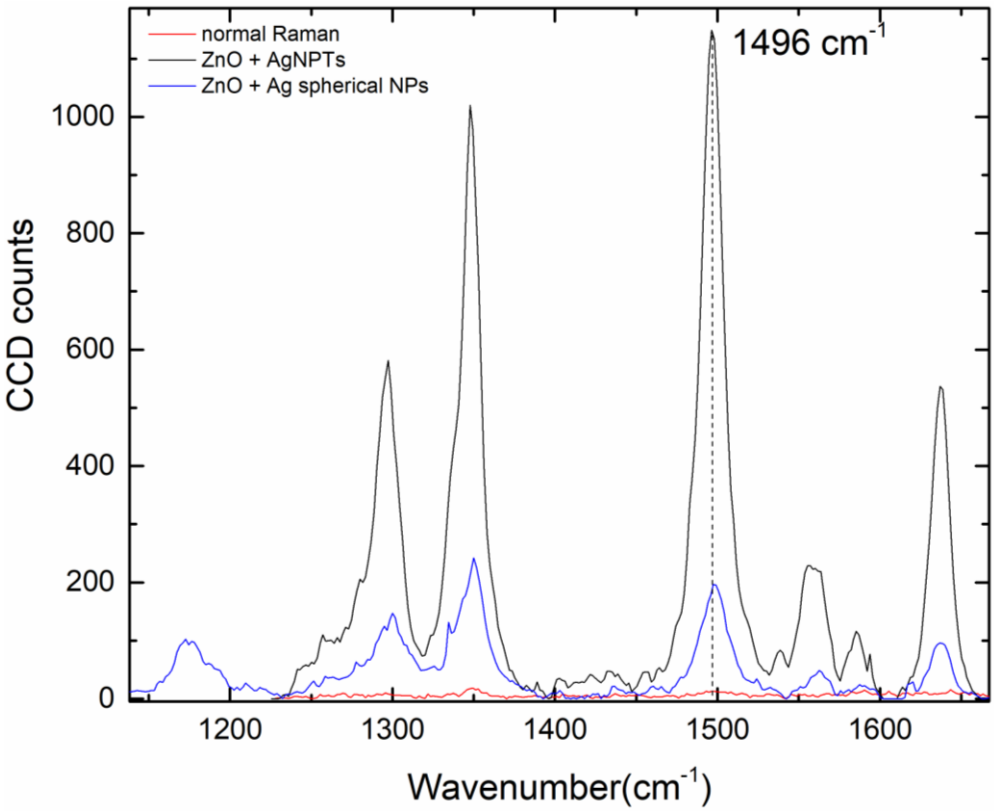


***Fig. 53:*** *Enhancement factor study for ZnO NRs grown on AgNPTs(black) and grown on spherical Ag NPs(blue)*

As said before, the evaluation of SERS EF is conducted by studying the ratio between the intensity of a SERS measurement and a normal Raman measurement. Figure 53 shows the measurements; it's to note that these measurements are done in the same experimental condition (excitation wavelength, Laser power, exposure and time of acquisition.) except for the substrate used and the concentration.

As referment peak,1496 $cm^{-1}$ have been chosen due to the high intensity. This latter is associated with stretching mode of benzene rings[93]. In table 6 are reported the value of intensity, concentration and SERS EF.

The value obtained is quite High. The difference in EF of one order of magnitude, demonstrate that the structure of the ZnO NRs combined with the presence of Ag on the tips of the structure itself enhance the sensitivity of the substrate.

In figure 54 is reported the evaluation of SERS EF using glucose as standard. The experimental parameters are the same as all other SERS experiment. In this case the peak of referment is the peak at 1522 $cm^{-1}$ relative to δ (CH) deformation, and/or δ(COH) deformation[94]

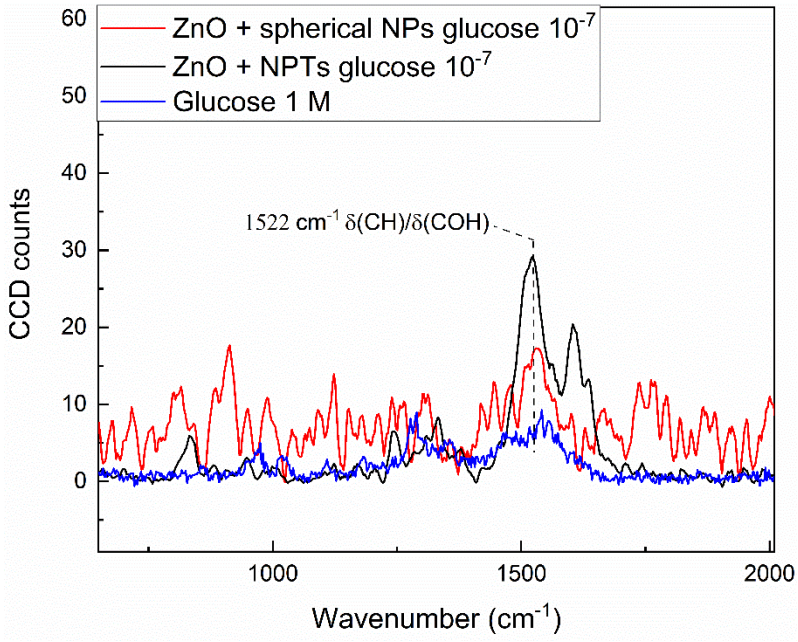


***Fig. 54:*** *Enhancement factor study for ZnO NRs grown on AgNPTs(black) and grown on spherical Ag NPs(red)*

In table 6 are reported the intensity for both experiment and relative EF obtained by equation 30. The values of EF 1,2 x 10 $^{7}$ for RhD 6G and 4,2 x 10 $^{7}$ for glucose results to be quite the same for the two different molecules; this gives a good certainty on the reproducibility of the experiments and on the relative value of EF calculated. The NRs grown on NPTs substrates present a higher EF. This enhancement can be attributed to the different and elongated shape as to the presence of spherical-like droplet of AgNPs on their tips. Structure with these features, in fact, as said before, give place to the lightning road effect, enhancing several orders of magnitude the intensity of the field around the nanostructures, does increase the enhancement factor.

| Substrate | Concentration(M) | Intensity(a.u.) | EF |
|---|---|---|---|
| **Si RhD 6G** | 1 | 12 | / |
| **ZnO+ Ag Spherical RhD 6G** | $10^{-5}$ | 181 | $1,5x10^{6}$ |
| **ZnO+ Ag NPTs RhD 6G** | $10^{-5}$ | 1495 | $1,2x10^{7}$ |
| **Si glucose** | 1 | 7 | / |
| **ZnO+ Ag Spherical glucose** | $10^{-7}$ | 17 | 2,4 x107 |
| **ZnO+ Ag NPTs glucose** | $10^{-7}$ | 30 | $4,2\ x10^{7}$ |

***Tab. 6:*** *Evaluation of the data obtained from Raman spectroscopy and evaluation of EF.*

The properties of this hybrid nanostructures result to be enhanced respect to the classical spherical NPs[70]. This can be attributed to the augmented charge separation induced by the formation of the Schottky junction at the interface ZnO NRs- Ag NPs, that give place at an intensified field, with respect to the

classical NPs when the nanostructure interacts with light. Also, the shape effect of the hybrid nanostructures influences the optical properties. More elongated and thin structure, in fact, present higher value of EF respects the classical hexagonal NRs (table 6).

### *3.6. Catalysis efficiency of the Hybrid NRs*

Below is reported another interesting application of this Hybrid nanostructure. As said before they present an interesting value of Energy band gap, so the degradation of methylene blue has been done to prove the catalytic efficiency. The samples were placed inside a beaker containing 5 ml of a $5x10^{-6}M$ ($C_0$) MB solution with the catalytically active surface facing upwards. The solution was illuminated by a UV lamp with a wavelength $\lambda$=365 nm. At fixed intervals, the absorbance of the MB solution was measured by means of a UV-Vis spectrophotometer. Sampling and subsequent measurements were carried out at 15-minute intervals for 2 hours; during the measurements the UV lamp was switched off.

Photocatalytic measurements were made for MB solutions in which they were immersed:

- Samples on which a ZnO nanostructures were grown on Si
- Samples on which ZnO nanostructures have been grown on a monolayer of Ag nanoplatelets and sphere deposited on a Si substrate.

In order to be able to compare the photocatalytic efficiencies of the samples, normalized absorbances ($C_0/C$) were reported as a function of time. In the supporting information are reported also the UV-VIS absorbance spectra.

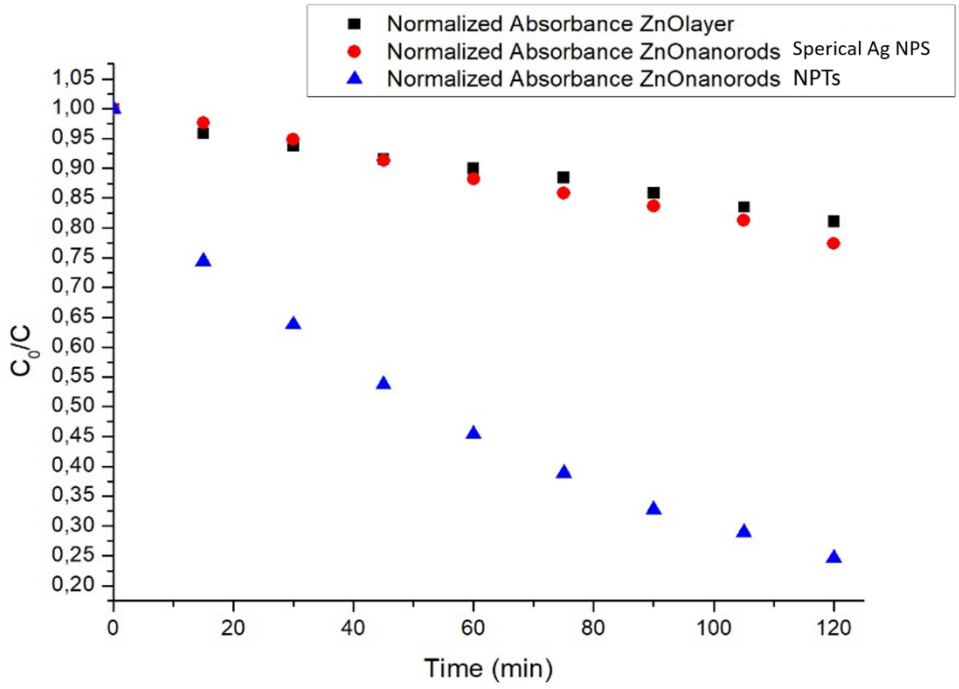


***Fig.55:*** *Normalized absorbance in function of time of degradation for the samples three samples*

Figure 55 shows that systems on which ZnO nanostructures have been grown on Ag NPTs have greater photocatalytic efficiency than systems on which a ZnO nanostructures have been grown on Si.

It is possible to justify this phenomenon taking into account the fact that the photodegradation of pollutants takes place on the surface of the photocatalyst, so nanostructured systems, which have a higher surface area, will be able to degrade more pollutants present in the solution. Moreover, can be invoked also, in this case, the enhanced efficiency of charge separation due to the

formation of the Schottky barrier. Thanks to this phenomenon, in fact, the time of life of the exciton couple is higher and so is more probable that excitons reach the surface were the photocatalytic reaction takes place.

## *Chapter 5: SESOX Project in collaboration with Universität Duisburg-Essen, Germany.*

To study the properties of different metals and Semiconductor metals, a six months collaboration with the group of Prof. Stephan Barcikowski at Universität Duisburg-Essen, Germany, working on the SESOX project. The aim of this project it's to study the influence that defect engineering of $TiO_2$, have on the catalytic efficiency of $TiO_2$-Au catalyst.

### *5.1 Introduction*

Highly active catalysts are obtained when supporting gold nanoparticles (NPs) on metal oxides, and the extensive exploration of Au-based catalysts in the past two decades has expanded their range of applications to reactions such as low-temperature CO oxidation[95,96], direct synthesis of hydrogen peroxide, alcohol oxidation and so on. In the field of alcohol oxidation, supported Au catalysts became highly attractive as deactivation is a less critical issue for Au relative to Pd or Pt benefitting from its higher resistance to oxygen poisoning[97]. Moreover, Au NPs showed superior selectivity in preferentially oxidizing functional groups without forming by-products. Generally, the particle size, oxidation state[98,99] and surrounding chemical environment affected by capping agents or ions are discussed in the literature as major factors influencing the reactivity of Au NPs. The preparation methods can significantly influence the properties of Au-based catalysts in the oxidation of

alcohols. The commonly adopted methods include wet impregnation, deposition–precipitation and sol immobilization, where calcination is essential to activate the catalyst by decomposing the precursors or removing the protecting agents. High-temperature treatments can result in metal–support interactions that change the catalytic properties of the catalytic material. For all these reasons the production of $Au/TiO_2$ hybrid nanostructures has been done with Au ligand-free nanoparticles produced by Laser ablation in pure water. These Au NPs fabricated via PLAL are purely electrostatically stabilized due to their high surface charge density and are ready for deposition on desired supports by simple mixing without additional post-treatment.

SESOX project is structured in four phases:

1. Modification of P25 with Laser treatment
2. Impregnation of the modified P25 with Au PLAL produced NPs
3. Characterization of the produced hybrid materials
4. Sensing and catalytic test to evaluate the improvement generated by step 1 and 2.

### *5.2 Phase 1: laser treatment*

As starting material, TiO2 P25 were used. P25 it's a mixture 80-20 % of respectively Anatase and Rutile. To change the defect density, the material has been pretreated using pulsed lasers with two different pulse duration (pico-second, and nano-second) and wavelength (532 nm, 355 nm). Specifically, three different lasers were used:

- Edgewave pulsed Laser (EW): 532 nm nanosecond pulse duration
- AVIA pulsed Laser (AVIA): 355 nm nanosecond pulse duration

- PIKO pulsed Laser (PIKO): 532 nm picosecond pulse duration

It is expected that the different pulse duration generates two different types of defect in the treated material. Particularly as the effect of the short pulse duration of the picosecond laser, which is in the range of the electron-phonon-relaxation, the temperature of electrons in the material is higher than the lattice after the photon absorption. This behavior generates point defects in the surface region of the material. In the case of nanoseconds lasers, on the other hand, the duration of the pulse, generate a thermal load of the lattice causing 2D/3D crystal defect in the particle bulk. The two different wavelengths determinate also, the efficiency of energy absorption. The 355 nm photons are efficiently adsorbed throughout the whole material because the energy of the photon it's above the bandgap of the $TiO_2$ (3.2 eV). The 532 nm photons, in contrast, presents energy below the bandgap of the material, so absorption is limited exclusively to interband gap states of already existing defects and adsorption efficiency result much lower than the other wavelength.

### *5.2.1 P25 defect engineering*

The experimental procedure to modify the material consists into the irradiation, with Laser light, of P25 dispersed in MilliQ water. Particularly 600 mg of P25 were dispersed in 2 l of water, the pH of the solution has been adjusted to 9 to ensure the stability of the dispersion. To make sure that the material is irradiated homogeneously during the laser modification process, a peristaltic pump has been used; the dispersion is passed through a nozzle, with a flow of 300 ml/min, and irradiated with pulsed Laser as shown in figure 56.

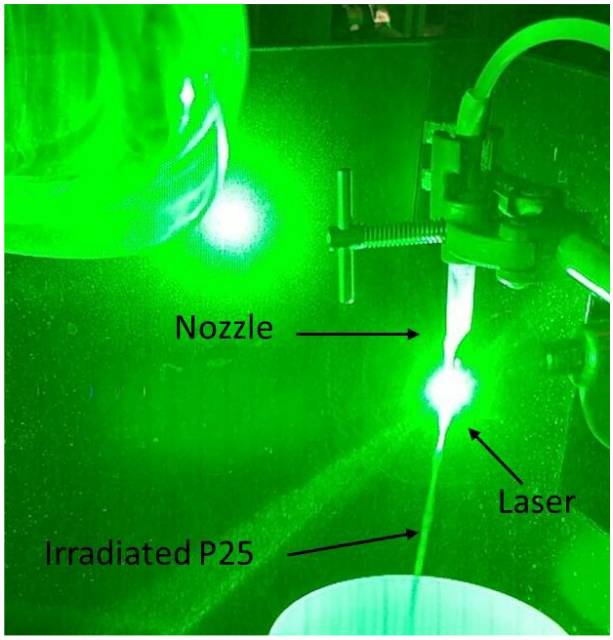


***Fig. 56:*** *Experimental setup for laser treatment in a continuous flow*

After all the dispersion it's irradiated, the process it's repeated from 1 to 25 times.

### *5.2.2 Gold NPs synthesis by PLAL*

Au NPs were synthesized using the pulsed laser ablation in liquid (PLAL) method. A nanosecond Nd: YAG laser (Edgewave) with a fundamental wavelength of 1064 nm was focused into a flow chamber which was continuously flushed with a 5 l aqueous solution with 0.1 mmol/L NaCl at a flow rate of 100 mL/min. The emitted laser pulses had a duration of 40 ns and a pulse energy of 8 mJ at a repetition rate of 5 kHz. By weighing the Gold target before and after the ablation process, a concentration of 75 mg for 1L of Au nanoparticles were estimated. To evaluate the dimension of the Au NPs

was used an analytical centrifugation disk (CPS, DC24000), finding that the as-synthesized Nanoparticles were about 20 nm. Since, the large size of such nanoparticles, a Laser fragmentation have been performed using the second harmonic of the same Laser, obtaining 4 nm Au NPs.

### *5.3 Phase 2: impregnation process of TiO2 with 4 nm Au NPs*

To obtain a 3% loaded P25, the impregnation was carried out by adding drop by drop 280 ml of Au colloid to 300 mg of irradiated P25 dispersion under magnetic stirring. The loading process was carried out at pH 9 to avoid the aggregation of the TiO2 nanoparticles, in fact, Au and $TiO_2$ NPs are negatively at pH 9 charged and stable in solution.

Z-potential at pH 9 was measured and for both NPs were found a value of -50mV, -60 mV.

Moreover, the loading process occurs in repulsive regimes, since both nanoparticles are negatively charged. In this condition, assume that the interaction between the Au NPs and P25 occurs for the interaction of Metal nanoparticles with the defective site of $TiO_2$ and not for electrostatic attraction. The deposition process was quantitative and all Au NPs result to be deposited on $TiO_2$ as indicated by the complete discoloration of the liquid phase. Then the samples were dried in a freeze dryer Alpha-model 2 LD PLUS and characterized. This deposition method including the influence of salinity and pH has been reported elsewhere on several particle-support combinations also yielding 100% material efficiency.

To further clarify the number and type of sample prepared and analyzed in table 1 it's reported a sample matrix.

| | N.Passage | 1 | 2 | 3 | 5 | 7 | 10 | 13 | 19 | 25 |
|---|---|---|---|---|---|---|---|---|---|---|
| **Laser** | / | / | / | / | / | / | / | / | / | / |
| **EW** | / | EW 1 | EW 2 | EW 3 | EW 4 | EW 5 | / | EW 6 | EW 7 | EW 8 |
| **PIKO** | / | PIKO 1 | / | / | PIKO 2 | / | PIKO 3 | / | / | / |
| **AVIA** | / | AVIA 1 | / | AVIA 2 | AVIA 3 | / | AVIA 4 | / | / | / |

***Tab 7:*** *Sample matrix for the different sample treated with the three different lasers*

### *5.4 Phase 3: characterization of the prepared hybrid materials*

#### *5.4.1 Uv-VIS reflectance*

The optical properties of modified TiO2 were studied by diffuse reflectance spectra. The reflectance spectra of TiO2 were measured for all laser tread samples not loaded and loaded with gold NPs. The variation of the energy bandgap in the material was estimated by Tauc plot. In the figures below are reported the reflectance plot for all samples.

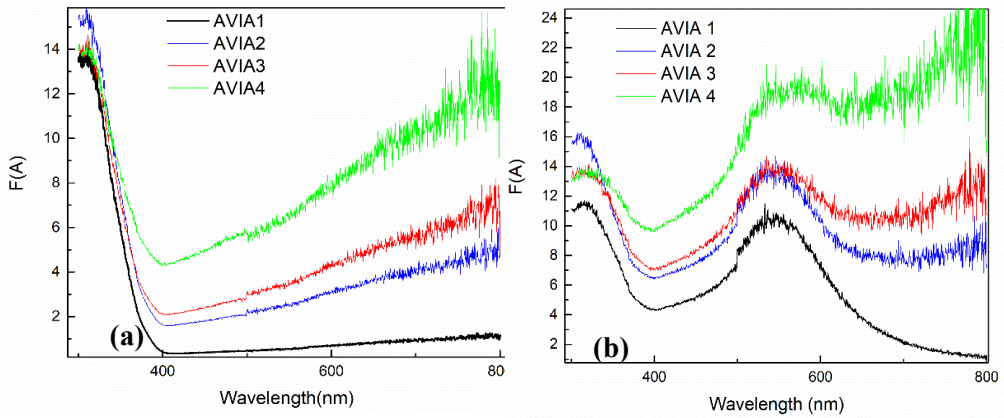


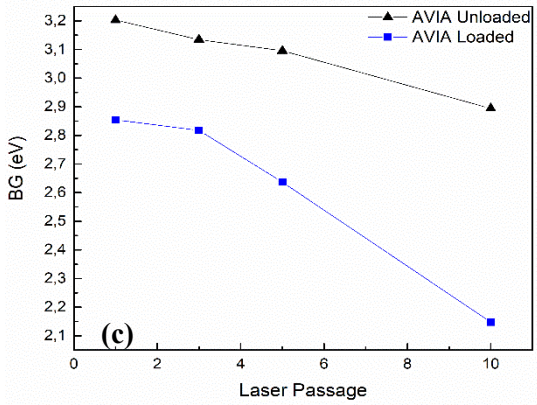


***Fig. 57:*** *$TiO_2$ unloaded (a) and loaded with Au NPs (b) AVIA treated reflectance spectra and estimation of energy BG in function of the number of Laser passage(c)*

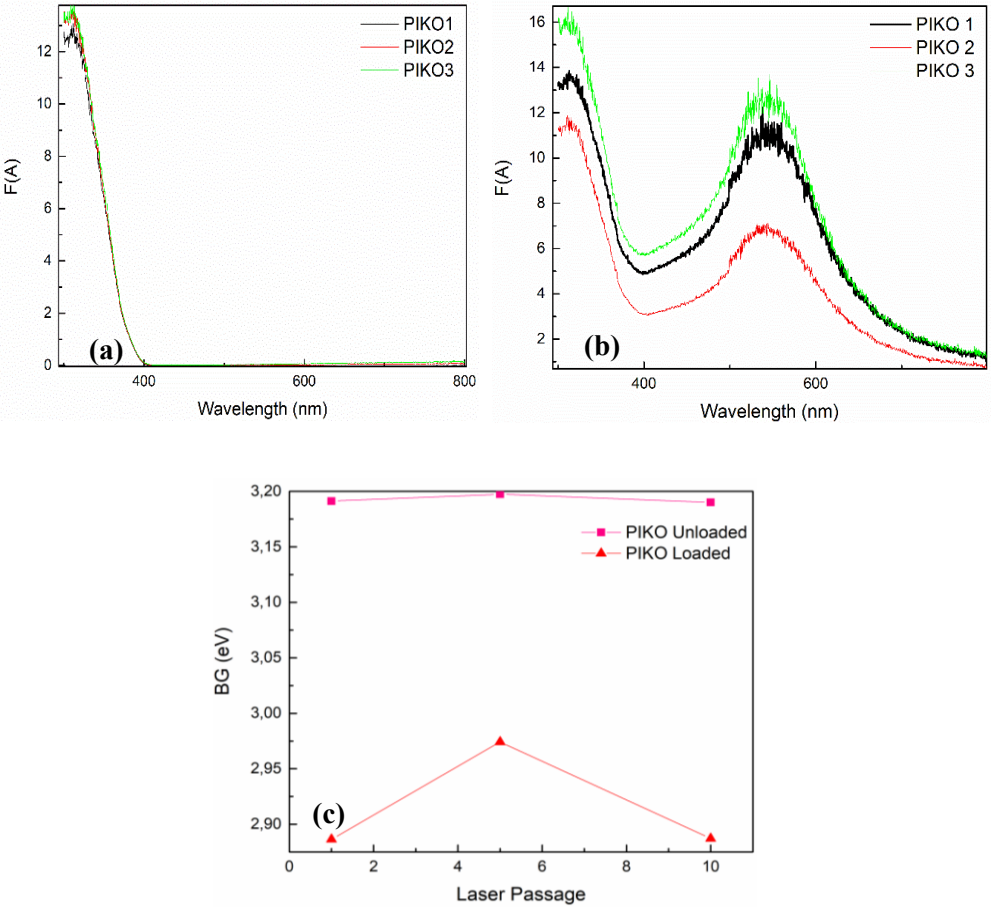


***Fig. 58:*** *$TiO_2$ unloaded (a) and loaded with Au NPs (b) PIKO treated reflectance spectra, estimation of energy BG in function of the number of Laser passage(c)*

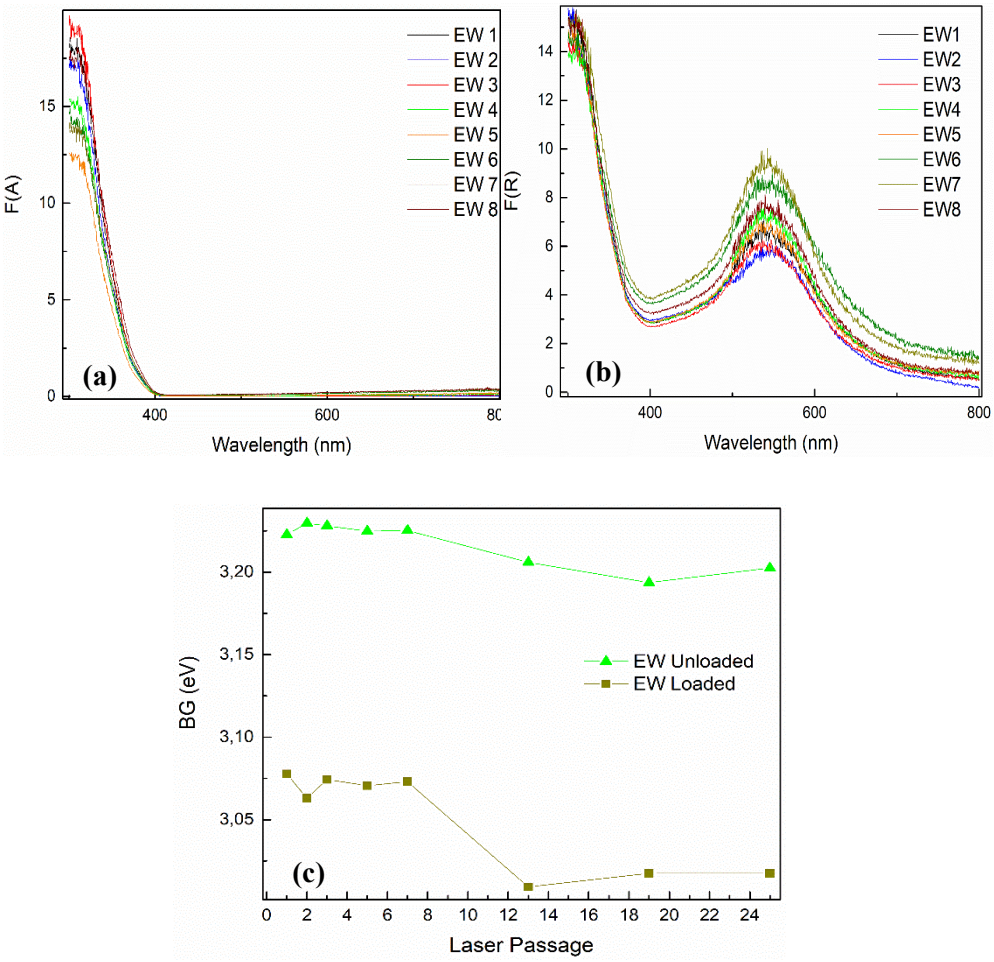


***Fig. 59:*** *$TiO_2$ unloaded (a) and loaded with Au NPs (b) EDGEWAVE treated reflectance spectra, estimation of energy BG in function of the number of Laser passage(c)*

In figures 57-59, are reported all the reflectance spectra for the synthesized sample as prepared, and loaded with 3 % of Gold. As it is possible to note the samples that present a significant change in the reflectance spectra, are the ones irradiated with the AVIA laser. The other sample does not present significant changes. This behavior it's confirmed also from the analysis of the Energy BG reported in table 8.

| | N.Passage | 1 | 2 | 3 | 5 | 7 | 10 | 19 | 25 |
|---|---|---|---|---|---|---|---|---|---|
| **Laser** | | | | | | | | | |
| **EW** | | 3,22 eV | 3,22 eV | 3,22 eV | 3,22 eV | 3,22 eV | 3,20 eV | 3,20 eV | 3,20 eV |
| **PIKO** | | 3,20 eV | / | / | 3,20 eV | / | 3,20 eV | / | / |
| **AVIA** | | 3,20 eV | / | 3,13 eV | 3 eV | / | 2,90 eV | / | / |
| **Gold loaded** | | | | | | | | | |
| **EW** | | 3,1 eV | 3,1 eV | 3,1 eV | 3,1 eV | 3,1 eV | 3 eV | 3 eV | 3 eV |
| **PIKO** | | 2,88 eV | / | / | 2,96 eV | / | 2,88 eV | / | / |
| **AVIA** | | 2,85 eV | 2,81 eV | / | 2,63 eV | / | 2,15 eV | / | / |

***Tab. 8:*** *Estimated Energy band gap for all prepared samples*

These samples show a significant modification in energy BG. These values are consistent with the expectation of the effect of laser treatment. Many reports, in fact, associate the reduction of the energy gap (gap between the orbital of O 2p and the orbital of Ti 3d bands) of $TiO_2$ (bulk) due to the generation of defect states within the gap. These defects are caused by the lattice disorder arising from the vacancies of oxygen generated by the laser treatment. Moreover, the samples loaded with gold, present an even lower bandgap. This behavior could be attributed to the existence of Au impurity energy levels in the middle of the bandgap of $TiO_2$ leading to an additional reduction of the energy bandgap.

### *5.4.2 Raman spectroscopy*

Raman spectroscopy results to be well suited, to investigate the modification induced by laser treatment of P25. Thanks to this technique It's possible to analyze, in fact, the anatase-to-rutile transition and to probe the presences of oxygen vacancies in the crystalline lattice of the material as well[100] the variation of particle sizes. The position of the characteristic peak relative to $TiO_2$ Rutile and Anatase are well known in literature[101]. The micro-Raman spectra obtained using a 633 nm excitation wavelength, of commercial P25 used result to be in very good agreement with already published data Figure 60.

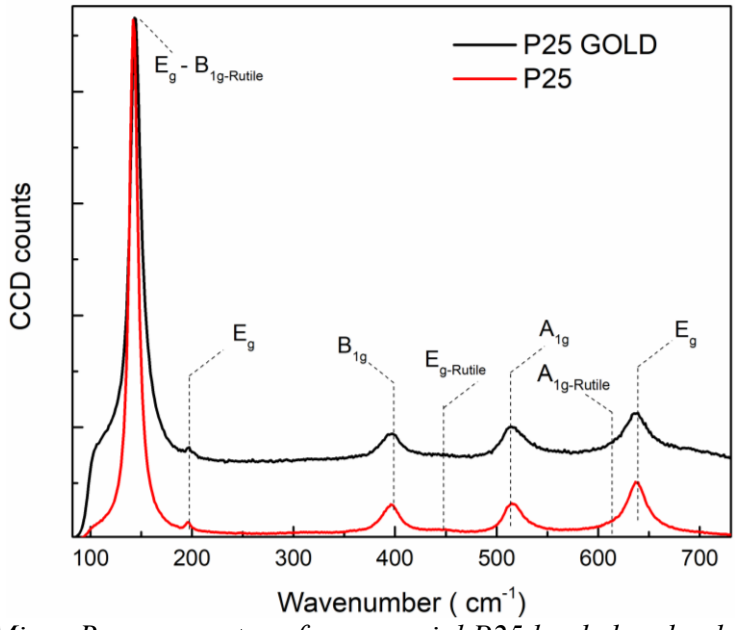


***Fig. 60:*** *Micro-Raman spectra of commercial P25 loaded and unloaded with gold*

In the case of Anatase, the bands corresponding to the six Raman active fundamental modes are recorded at 144 $cm^{-1}$ ($E_g$ ), 197 $cm^{-1}$ ($E_g$ ), 397 $cm^{-1}$ ($B_{1g}$ ), 518 $cm^{-1}$ ($A_{1g}$) and 640 $cm^{-1}$ ($E_g$ ) results very intense. As for rutile, meanwhile, the three of the four Raman active modes, respectively, at 144 $cm^{-1}$ ($B_{1g}$ ), 448 $cm^{-1}$ ($E_g$ ) and 613 $cm^{-1}$($A_{1g}$) are not distinguishable because of the lower concentration of Rutile respect Anatase in P25.

The peak $E_g$ $A_{1g}$ and $B_{1g}$ correspond to specific vibration of O-Ti-O particularly:

• Eg 140 cm-1 it's the symmetric stretching of O-Ti-O Anatase structure

• B1g 394 cm-1 it's the symmetric bending of O-Ti-O for Anatase structure

• A1g 514 and 637 cm-1 it's the antisymmetric bending of O-Ti-O for Anatase structure

• Eg 450 cm-1 it's the symmetric stretching of O-Ti-O for Rutile structure

• A1g 610 cm-1 it's the antisymmetric Bending of O-Ti-O for Rutile structure.

### *5.4.3 Characterization of the defect induced by Laser treatment*

In figures 61-63, are reported the Raman spectra of the treated P25. The modification in the vibrational peak can be attributed to the defect generated in the material due to the laser treatment accordingly with what said before. For the sample irradiated with PIKO and EW Lasers (532 nm) in figure 61,62, Raman spectra don't show significant changes in the vibrational peak respect the as-bought P25. Just after a high number of passage (orange curve), the sample irradiated with EW laser (figure 61) shows an increase in the rutile vibrational features with the appearance of peak at 450 and 610 $cm^{-1}$ and a decreasing in the signals relative to the Anatase phase. This phenomenon is attributed to the change in the crystalline structure from anatase to Rutile produced by the Laser at high number of passages. Increasing the number of

passage, the energy absorbed by the sample increase, inducing a phase transformation from Anatase to more thermodynamically stable Rutile due to laser warming for the irradiance used. Is to note that the vibrational features relative to Anatase and Rutile are highlighted in the spectra respectively with A and R.

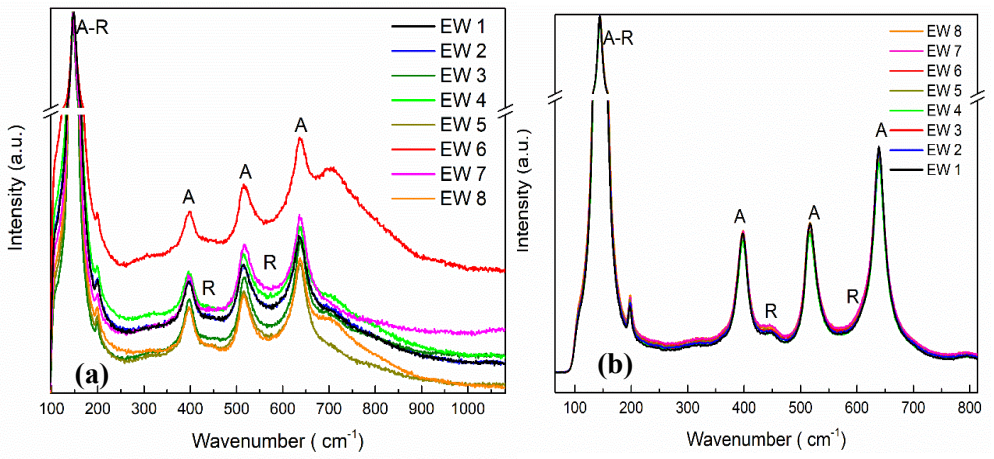


***Fig. 61:*** *Micro-Raman spectra of P25 treated with Edgewave laser unloaded (b) and loaded (a) with gold NPs*

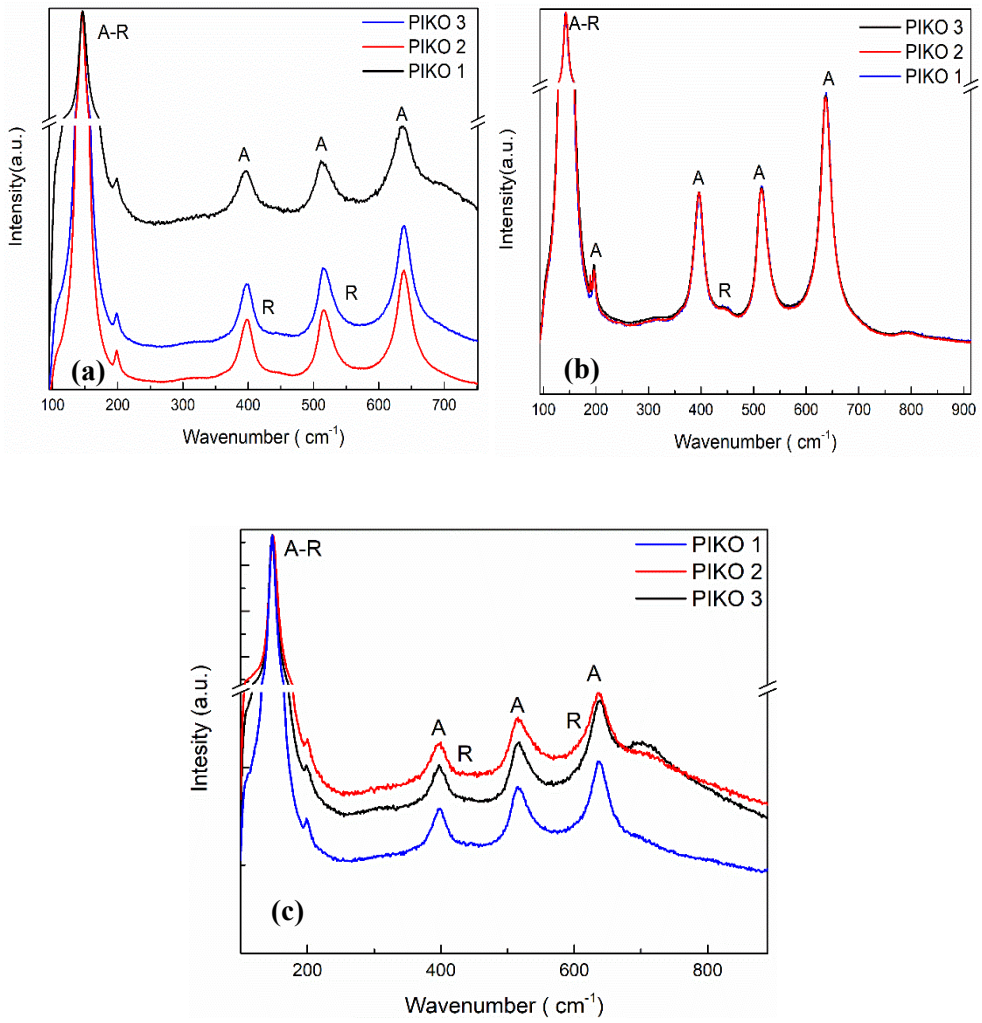


***Fig. 62:*** *Micro-Raman spectra of P25 treated with PIKO laser unloaded (b) loaded before the laser treatment (a) and loaded after the treatment with gold NPs(c)*

The case for the AVIA samples (figure 63) it's totally different. These samples, in fact, shows already, after the first laser passage, a change in the ratio between the Rutile and Anatase signals. Moreover, after loading the sample with gold, a new, not reported in the literature for P25, peak appears at 700 $cm^{-1}$.

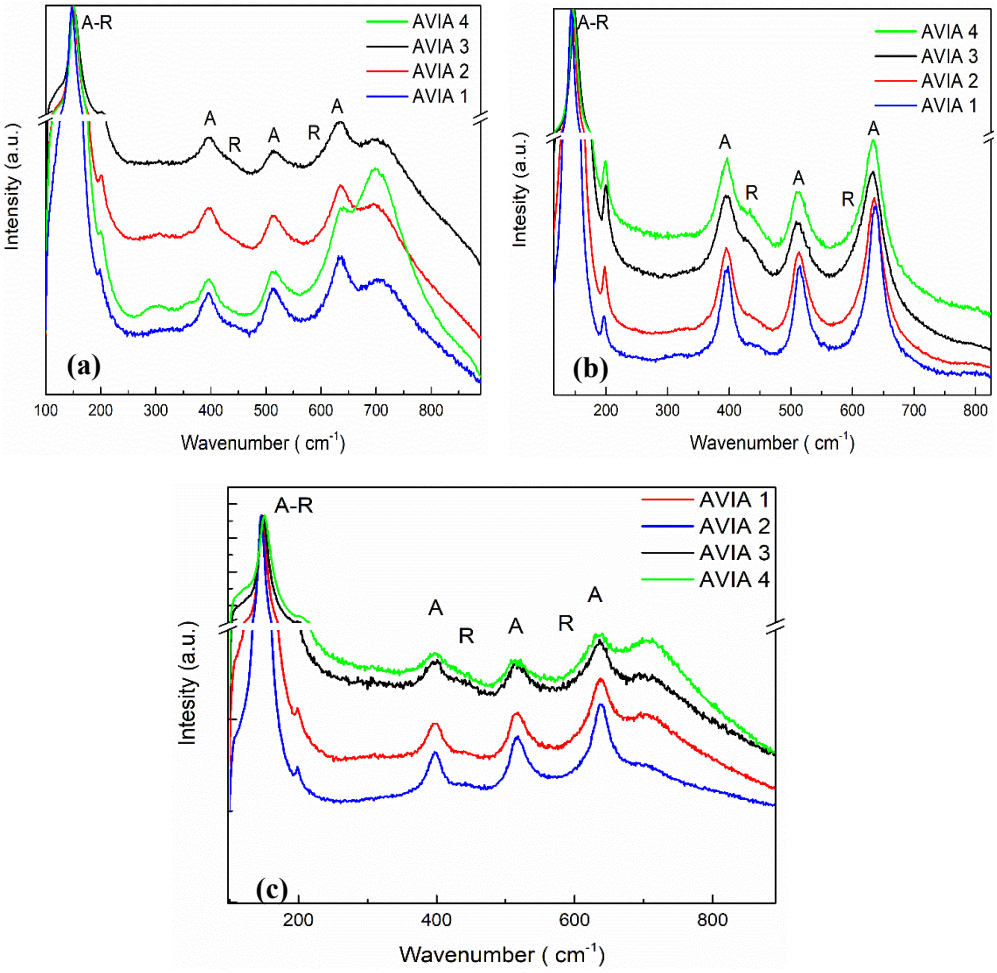


***Fig. 63:*** *Micro-Raman spectra of P25 treated with AVIA laser unloaded (b) loaded before the laser treatment (a) and loaded after the treatment with gold NPs(c)*

By plotting the heights of the pick in function of the number of passages, it is possible to clarify the effect of laser irradiation on the structure of P25. The heights were obtained by fitting the Raman spectra with a Gaussian function( an expel of fitting it's reported in the supplementary information).

The graph in figures 64, 65 for the samples irradiated with PIKO and EW laser, clarify the effect of laser treatment of the material with green Lasers. there is no significant variation in intensity for the main vibrational peaks. These peaks remain almost constant as the number of passages increases, for both loaded and unloaded with gold samples.

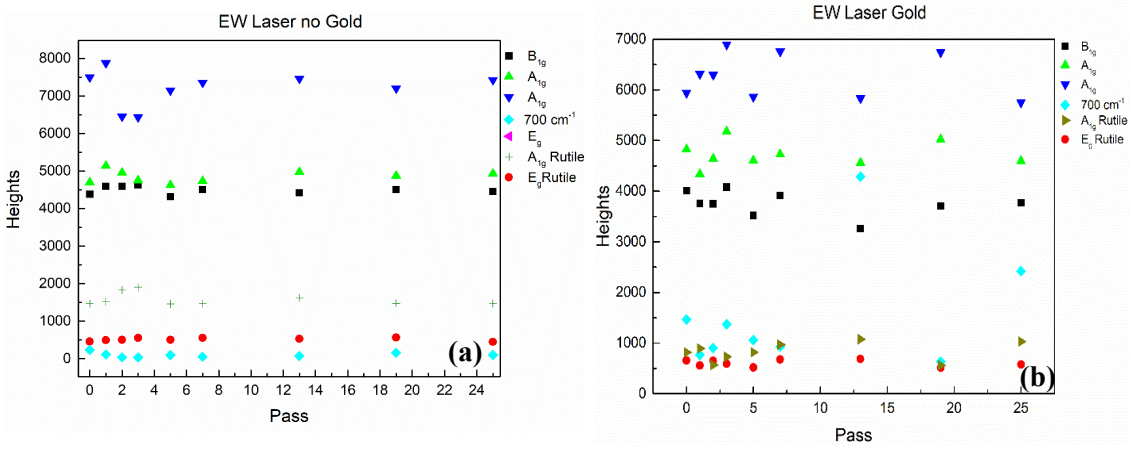


***Fig. 64:*** *Fitted Heights of P25 treated with Edgewave laser unloaded (a) and loaded with gold(b).*

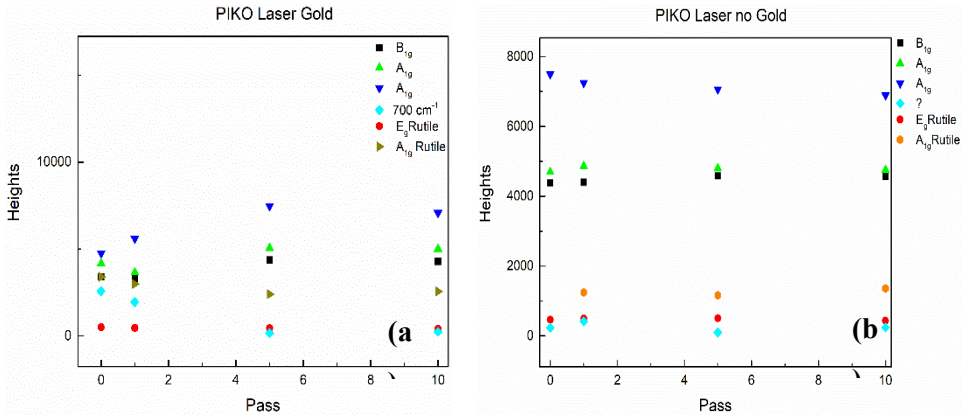


***Fig. 65:*** *Fitted Heights of P25 Raman peaks treated with PIKO laser unloaded (a)loaded (b) and loaded with gold NPs*

The reason for this behavior could be explained considering the wavelength used for irradiation. As said before, the wavelength of EW and PIKO lasers is 532 nm, photon energy at this wavelength is below the bandgap of TiO2, so the light absorption is limited exclusively to interband gap states of already existing defects. Hence, laser treatment only alters the already existing defect structure, moreover, the energy is not absorbed efficiently, consequently the energy is not enough to cause a change in the crystalline structure. Further studies are underway to confirm this statement. Figure 66 shows the fitted heights for the P25 irradiated with AVIA Laser. In this case it' clear that the high quantity of energy adsorbed thanks to the match of the photon energy and the BG of P25, cause immediate changes in the structure. The intensity of $A_{1g}$, $B_{1g}$ of Anatase decrease by increasing the number of laser passage meanwhile the intensity of $A_{1g}$, $E_g$ of Rutile increase. Evidence that the quantity of energy absorbed during the process it's enough to induce phase transformation from Anatase to Rutile.

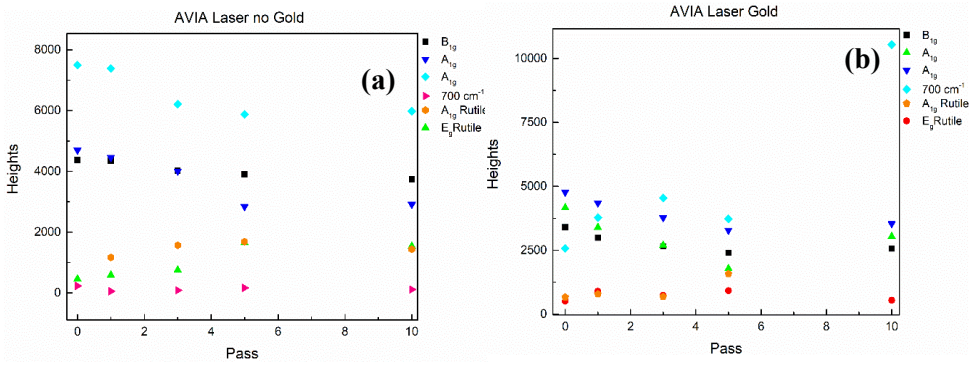


***Fig. 64:*** *Fitted Heights of P25 Raman peaks treated with AVIA laser unloaded (a) loaded (b) and loaded with gold NPs*

This behavior is enhanced after the Gold loading process. It's to note the appearance of a new peak at 700 cm-1 just for the sample loaded with gold, meanwhile for all the other sample not loaded. This peak increased its intensity by increasing the number of passages. The presence of this peak is attributed to a signal of an amorphous non-stoichiometric structure of $TiO_2$[102]. The reasons because this peak is present just in the sample loaded with gold could be two. First the Au NPs can act as catalyst by concentrating the light and consequently increase the temperature near their surface which induce an amorphization of the region of P25 in contact with Au NPs. The second effect is relative to the SERS enhancement of the signal due to the presence of Au NPs. In fact, this amorphous region could be already present, before the impregnation of P25 with gold, as consequence of laser treatment. In this case the concentration of this defective area could be so low that in absence of signal enhancement, is impossible to detect it. But after the loading process the Au NPs present on the surface of P25 can enhance the Raman signal does

increasing the detection limit of the technique permitting to reveal even low concentrated defective area.

Another very interesting feature to note it's the shift of the $E_g$ (140 cm $^{-1}$) peak for all the treated sample. In figure 65 (a) it's reported the Raman spectra of AVIA treated sample of $E_g$ peak and (b) the shift of the same peak for all treated sample.

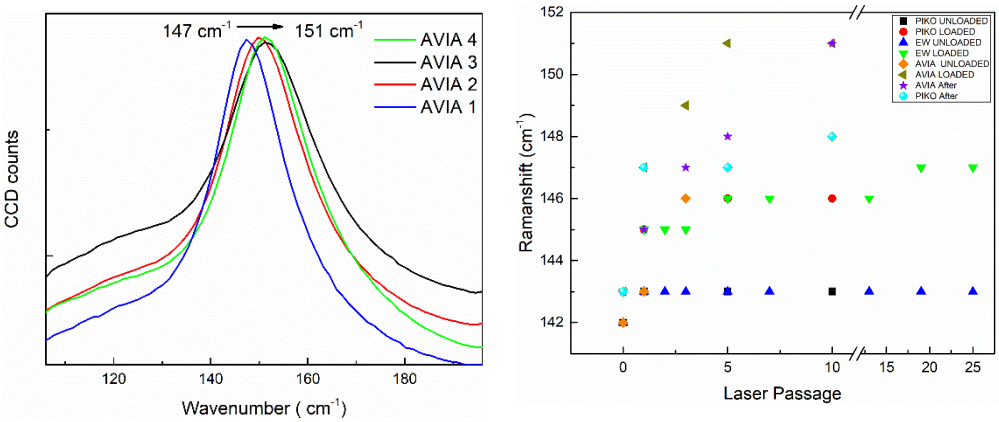


***Fig. 65:*** *Raman spectra of AVIA treated sample of $E_g$ peak and (b) the shift of the same peak for all treated sample*

As shown in figure 65 (a) after AVIA laser treatment the $E_g$ peak blueshift from 142 cm$^{-1}$ of the not treat P25 to 147 cm$^{-1}$ up to 151 cm$^{-1}$ for the 10 passage sample. Moreover, an increase of the full width at half maximum (FWHM) is also evident. This spectral behavior could have two possible origins; an oxygen deficiency and (or) phonon confinement due to the nanosystem size. This last effect results to have a small impact for large particle size but increase dramatically when the size is lower than 10 nm. From figure 65 (b) results, that by increasing the number of laser passages exist two different behavior. The first relative to P25 not loaded and treated with PIKO and EW laser (532 nm), for which after laser treatment there is a blueshift of just 1 cm$^{-1}$. This

first behavior it's a confirmation that by using a 532 nm wavelength the adsorption is limited exclusively to interband gap states of the already existing defect, so laser treatment doesn't generate new defect in the material. The second behavior it's relative to P25 loaded and not loaded and treated with AVIA laser (355 nm). For these samples is present a big blueshift of 7 $cm^{-1}$ for non-loaded and of 9 $cm^{-1}$ for the loaded one, that could be attributed to an intergrain defect that causes a lattice disorder because of increasing loss of oxygen in $TiO_2$[103,104] structure by increasing the number of laser passage. It's to note that the bigger shift of the loaded sample, respect the unloaded one, could be a demonstration that the gold NPs are adsorbed into the defective areas of the materials where there is an oxygen deficiency. These data seem to fit perfectly with reflectance data shown before, where the decreasing of the energy bandgap, for the AVIA treated sample, was related to the increasing number of oxygen vacancy; meanwhile, the sample treated with the other two laser doesn't show any variation in the energy bandgap.

### *5.5 Phase 4: Catalytic and Sensing data*

After the characterization of all the sample produced the catalytic and sensing activity will be analyzed. at the time this work was written there are still no catalytic or sensing data as it is still being worked on. The aim as said in the introduction of this project is to enhance the Ethanol degradation capability of this material and the sensing capability for such materials. From the results of the catalytic and sensing analysis, will be possible to understand if the variation, in the crystalline structure, Band Gap, defect density caused by the Laser treatment, enhance or quench the chemical-physical properties of the hybrid material.

## *Conclusion*

In this work have been studied and presented extensively the chemical-physical properties of metallic Nanoparticles and Hybrid MO/M nanostructures. Starting from the classical theory of dampened oscillator passing to the more accurate Mie theory, it has been possible not only to understand the typical properties of NPs, but above all, it was possible to predict which characteristics of the nanostructures to modify to obtain intensified optical properties. It was thus possible to modify the experimental conditions of the synthesis method, to obtain different sizes and structures of NPs with enhanced chemical-physical properties. Specifically, have been studied deeply the kinetics of the seed-mediated growth of Ag NPTs does obtain a complete control on the shape, size, and SP position. As a result of this have been found the experimental, in terms of precursor adding rate and volume of starting seed, condition to obtain NPTs with highest Dipole sensitivity. For slow Ag precursor rate, 0,3 ml/min, it has been found that the homonucleation of spherical Ag NPs is hindered, meanwhile is favored the growth of larger and sharper NPTs. Moreover, if a very low volume of seeds is used the same behavior in terms of dimension and sharpness is favored. So by combining these two findings, it's possible to obtain larger NPTs that present highest Dipole sensitive and EF as in the case of the NPTs synthetized with 20µl with a flow rate of 0,3ml/min. Obviously, this process has some limits, it is not possible in fact, slow down even more the flow rate because adding rate slower then a limit value does not change the properties of NPTs as shown in figure 16. The growth process, in fact, has been found to follow a saturation behavior, once the $\lambda_{max}$ is reached a further slowing in the precursor addition rate does not involve a further change in the optical properties. Also, the volume of seeds used for the growth process results to be limited. As shown in figure 14 by using 20 µl of seeds solution the main plasmon peak results to be in the NIR region, which is the limit range of classical UV-VIS spectrometer. A further decreasing in seeds volume generate a redshift even more in the IR region of the main resonance peak, thus extremely

complicating the use of NPTs as RI sensor and SERS active substrate. Another interesting finding of this work is that to increase the chemical-physical properties of NPTs, is of fundamental importance a clean synthesis that does not produce by-products. In fact, as reported in table 4 the new synthesis proposed in this work permit to obtain enhanced dipole sensitivity and SERS EF for NPTs produced with "green reshaping process" respect the same NPTs in terms of shape dimension and SP position, produced with the classical chemical synthesis method. This result is certainly attributed to the absence of by-products on the surface of NPTs. By studying the process of reshaping, it has been found that the light used to induce the reshaping photoreaction, determinate the shape of NPs obtained. In fact by using a polychromatic light, which present emission in all VIS range, a mix of different shape have been obtained, meanwhile, by using a monochromatic 580 nm light source just a single family of triangular-shaped NPs have been obtained. Anyway, also this method presents some drawback. In fact, with respect to the chemical synthesis, it is not easy or even possible to tune the dimension of the NPs obtained and so to tune the SP in al VIS-NIR range result to be very complicated. Further studies are necessary to try to drive the reshaping process to obtain complete control on the position of the plasmon resonance. As expected, the combination of Ag NPs, with enhanced characteristic, with ZnO NRs brought two results. First, the dimension and shape of Ag NPs used, guide the growth process ZnO nanostructures thus generating different shape and size of NRs. In fact, by using classical spherical Ag NPs as a catalytic substrate for MOCVD, hexagonal, ordered, nanorods have been obtained. Meanwhile, by using as catalytic substrate Ag NPTs is possible to obtain a more exotic structure as in the case showed in figure 48. This structure result to be very elongated thin and presents Silver nano-droplet on their tips. Second, the combination with Ag NPs enhances the catalytic and sensing capability of ZnO NRs. The SERS

EF of this nanostructures, in fact, results to be of $10^7$; this value is quite the same as Ag NPTs. A more detailed study of the experimental condition of MOCVD to achieve better control on shape size and orientation of NRs can lead to a huge improvement of the SESR capability of these nanostructures. For this reason, a systematic study of the growth condition in terms of temperature, time, and density of the catalytic layer on the substrate is underway.

**Publications:**

- Condorelli, M., Scardaci, V., D'Urso, L., Puglisi, O., Fazio, E., & Compagnini, G. (2019). **Plasmon sensing and enhancement of laser prepared silver colloidal nanoplates**. *Applied Surface Science*, *475*, 633-638.
- Condorelli, M., Scardaci, V., D'Urso, L., Puglisi, O., Fazio, E., & Compagnini, G. (2019). **Optical data related to Ag nanoplates utilized for plasmon sensing.** ***Data in Brief***, *23*, 103798.
- Compagnini, G., Condorelli, M., Fragalà, M. E., Scardaci, V., Tinnirello, I., Puglisi, O., & Fazio, E. (2019). **Growth Kinetics and Sensing Features of Colloidal Silver Nanoplates.** *Journal of Nanomaterials, 2019,* 1–8 (2019)
- D'Urso, L., Condorelli, M., Puglisi, O., Tempra, C., Lolicato, F., Compagnini, G., & La Rosa, C. (2018**). Detection and characterization at nM concentration of oligomers formed by hIAPP, Aβ (1–40) and their equimolar mixture using SERS and MD simulations**. *Physical Chemistry Chemical Physics*, *20*(31), 20588-20596.
- Messina, G. C., Sinatra, M. G., Bonanni, V., Brescia, R., Alabastri, A., Pineider, Campo G. , Sangregorio C., Li Destri G., Sfuncia G., Marletta G., Condorelli M., Zaccaria R. P., De Angelis F., Compagnini G. (2016). **Tuning the composition of alloy nanoparticles through laser mixing: The role of surface plasmon resonance.** *The Journal of Physical Chemistry C*, *120*(23), 12810-12818.
- La Rosa C., Condorelli M., Compagnini G., Lolicato F., Milardi D., Nu Do T., Karttunen M., Pannuzzo M., Ramamoorthy A., Fraternali F., Collu F., Rezaei H.; Strodel B.; Raudino A. **Symmetry-Breaking Transitions in the Early Steps of Proteins self-assembly.** (Under publication)

**Congress Oral presentations and Posters:**

- **Nanoparticles as probe to characterize transient oligomeric state of amyloid protein** *Marcello Condorelli et al.* Poster, Materials 2016
- **Silver Nanoplatelets : a promising dual SPR-SERS substrate for plasmonic sensing** *Marcello Condorelli et al.* Poster, Plasmonica 2017
- **Amyloid oligomers characterization by Surface-Enhanced Raman Spectroscopy at nM concentration.** *Marcello Condorelli et al.* Poster 2017
- **Sintesi e caratterizzazione di Nanoplatelets d'argento.** *Marcello Condorelli et al.* Oral Presentation SCI 2018
- **Plasmon sensitivity of silver nanoplatelets.** *Marcello Condorelli et al.* Oral presentation Sensor 2018
- **Sensing features of Silver Nanoparticles green generated and reshaped.** *Marcello Condorelli et al.* Flash presentation MEYCS 2018
- **Plasmon sensing properties of noble metal colloids prepared by ablation in water.** *Marcello Condorelli et al.* ANGEL 2018 Poster.

**References**


1. *NANOTECHNOLOGY RESEARCH PUBLICATIONS: STATISTICS AND ANALYSIS*. (2017). doi:10.22631/nrp.2017.03
2. Müller, H. Optical Properties of Metal Clusters. *Zeitschrift für Phys. Chemie* **194**, 278–279 (2011).
3. Dereux, A., Ebbesen, T. W. & Barnes, W. L. Surface plasmon subwavelength optics. *Nature* **424**, 824–830 (2003).
4. Linic, S., Christopher, P. & Ingram, D. B. Plasmonic-metal nanostructures for efficient conversion of solar to chemical energy. *Nature Materials* **10**, 911–921 (2011).
5. Zhang, X., Lu, J. J., Qin, X. & Zhao, X. N. A high-level energy consumption model for heterogeneous data centers. *Simul. Model. Pract. Theory* **39**, 41–55 (2013).
6. Sun, Y., Yang, X., Zhao, H. & Wang, R. Non-symmetric hybrids of noble metal-semiconductor: Interplay of nanoparticles and nanostructures in formation dynamics and plasmonic applications. *Progress in Natural Science: Materials International* **27**, 157–168 (2017).
7. Schaming, D. & Remita, H. Nanotechnology: from the ancient time to nowadays. *Found. Chem.* **17**, 187–205 (2015).
8. Rovigo, F. *et al.* Chemical analyses of Bronze Age glasses from Frattesina di Rovigo, Northern Italy. *J. Archaeol. Sci.* **31**, 1175–1184 (2004).
9. BARBER, D. J. & FREESTONE, I. C. AN INVESTIGATION OF THE ORIGIN OF THE COLOUR OF THE LYCURGUS CUP BY ANALYTICAL TRANSMISSION ELECTRON MICROSCOPY. *Archaeometry* **32**, 33–45 (1990).

10. Freestone, I., Meeks, N., Sax, M. & Higgitt, C. The Lycurgus Cup - A Roman nanotechnology. *Gold Bull.* **40**, 270–277 (2008).
11. Polette, L. A., Meitzner, G., Yacaman, M. J. & Chianelli, R. R. Maya blue: Application of XAS and HRTEM to materials science in art and archaeology. *Microchem. J.* **71**, 167–174 (2002).
12. Pérez-Villar, S., Rubio, J. & Oteo, J. L. Study of color and structural changes in silver painted medieval glasses. *J. Non. Cryst. Solids* **354**, 1833–1844 (2008).
13. Rubio, F., Pérez-Villar, S., Garrido, M. A., Rubio, J. & Oteo, J. L. Application of Gradient and Confocal Raman Spectroscopy to Analyze Silver Nanoparticle Diffusion in Medieval Glasses. *J. Nano Res.* **8**, 89–97 (2009).
14. Müller, H. Optical Properties of Metal Clusters. *Zeitschrift für Phys. Chemie* **194**, 278–279 (2011).
15. Garcia, M. A. Surface plasmons in metallic nanoparticles: Fundamentals and applications. *Journal of Physics D: Applied Physics* **44**, 283001 (2011).
16. Drude, P. Zur Elektronentheorie der Metalle; II. Teil. Galvanomagnetische und thermomagnetische Effecte. *Ann. Phys.* **308**, 369–402 (1900).
17. Almog, I. F., Bradley, M. S. & Bulovi, V. The Lorentz Oscillator and its Applications. *Lect. notes* 1–34 (2011).
18. Mie, G. Beiträge zur Optik trüber Medien, speziell kolloidaler Metallösungen. *Ann. Phys.* **330**, 377–445 (1908).
19. Müller, H. Optical Properties of Metal Clusters. *Zeitschrift für Phys. Chemie* **194**, 278–279 (2011).
20. Dimon, P. *et al.* Structure of aggregated gold colloids. *Phys. Rev. Lett.* **57**, 595–598 (1986).

21. Collier, C. P., Saykally, R. J., Shiang, J. J., Henrichs, S. E. & Heath, J. R. Reversible tuning of silver quantum dot monolayers through the metal- insulator transition. *Science (80-. ).* **277**, 1978–1981 (1997).
22. Kreibig, U., Schmitz, B. & Breuer, H. D. Separation of plasmon-polariton modes of small metal particles. *Phys. Rev. B* **36**, 5027–5030 (1987).
23. Kelly, K. L., Coronado, E., Zhao, L. L. & Schatz, G. C. The optical properties of metal nanoparticles: The influence of size, shape, and dielectric environment. *J. Phys. Chem. B* **107**, 668–677 (2003).
24. Link, S. & El-Sayed, M. A. Spectral Properties and Relaxation Dynamics of Surface Plasmon Electronic Oscillations in Gold and Silver Nanodots and Nanorods. *J. Phys. Chem. B* **103**, 8410–8426 (2002).
25. Katz, E. & Willner, I. Integrated nanoparticle-biomolecule hybrid systems: Synthesis, properties, and applications. *Angewandte Chemie - International Edition* **43**, 6042–6108 (2004).
26. Underwood, S. & Mulvaney, P. Effect of the Solution Refractive Index on the Color of Gold Colloids. *Langmuir* **10**, 3427–3430 (1994).
27. Kravets, V. G. *et al.* Composite au nanostructures for fluorescence studies in visible light. *Nano Lett.* **10**, 874–879 (2010).
28. Yu, C. & Irudayaraj, J. Multiplex biosensor using gold nanorods. *Anal. Chem.* **79**, 572–579 (2007).
29. Compagnini, G. *et al.* Growth kinetics and sensing features of colloidal silver nanoplates. *J. Nanomater.* **2019**, 1–8 (2019).
30. Schatz, G. C. Theoretical Studies of Surface Enhanced Raman Scattering. *Acc. Chem. Res.* **17**, 370–376 (1984).
31. D'Urso, L. *et al.* Surface-enhanced Raman scattering study on 1D-2D graphene-based structures. *Carbon N. Y.* **49**, 3149–3157 (2011).

32. D'Urso, L. *et al.* Detection and characterization at nM concentration of oligomers formed by hIAPP, Aβ(1-40) and their equimolar mixture using SERS and MD simulations. *Phys. Chem. Chem. Phys.* **20**, 20588–20596 (2018).
33. Le Ru, E. C. & Etchegoin, P. G. (Pablo G. *Principles of surface-enhanced Raman spectroscopy : and related plasmonic effects*. (Elsevier, 2009).
34. Jackson, J. D. *Classical Electrodynamics, Third Edition, Vol. 67*. *American Journal of Physics* (1999).
35. Le Ru, E. C. & Etchegoin, P. G. Quantifying SERS enhancements. *MRS Bull.* **38**, 631–640 (2013).
36. Chen, G., Roy, I., Yang, C. & Prasad, P. N. Nanochemistry and Nanomedicine for Nanoparticle-based Diagnostics and Therapy. *Chemical Reviews* **116**, 2826–2885 (2016).
37. Pastoriza-Santos, I. & Liz-Marzán, L. M. Colloidal silver nanoplates. State of the art and future challenges. *J. Mater. Chem.* **18**, 1724–1737 (2008).
38. Ingram, D. B. Composite Silver/Titania Photocatalysts for Visible Light Water Splitting: The Role of Silver Surface Plasmons. (2011).
39. Sajanlal, P. R., Sreeprasad, T. S., Samal, A. K. & Pradeep, T. Anisotropic nanomaterials: structure, growth, assembly, and functions. *Nano Rev.* **2**, 5883 (2011).
40. Ji, X. *et al.* Size control of gold nanocrystals in citrate reduction: The third role of citrate. *J. Am. Chem. Soc.* **129**, 13939–13948 (2007).
41. Zong, R., Wang, X., Shi, S. & Zhu, Y. Kinetically controlled seed-mediated growth of narrow dispersed silver nanoparticles up to 120 nm: Secondary nucleation, size focusing, and Ostwald ripening. *Phys. Chem. Chem. Phys.* **16**, 4236–4241 (2014).

42. Park, J., Joo, J., Soon, G. K., Jang, Y. & Hyeon, T. Synthesis of monodisperse spherical nanocrystals. *Angewandte Chemie - International Edition* **46**, 4630–4660 (2007).
43. Jana, N. R., Gearheart, L. & Murphy, C. J. Evidence for seed-mediated nucleation in the chemical reduction of gold salts to gold nanoparticles. *Chem. Mater.* **13**, 2313–2322 (2001).
44. Brown, K. R., Walter, D. G. & Natan, M. J. Seeding of colloidal Au nanoparticle solutions. 2. Improved control of particle size and shape. *Chem. Mater.* **12**, 306–313 (2000).
45. Li, S., Xie, T., Peng, Q. & Li, Y. Nucleation and growth of CeF3 and NaCeF4 nanocrystals. *Chem. - A Eur. J.* **15**, 2512–2517 (2009).
46. Soon, G. K. & Hyeon, T. Colloidal chemical synthesis and formation kinetics of uniformly sized nanocrystals of metals, oxides, and chalcogenides. *Acc. Chem. Res.* **41**, 1696–1709 (2008).
47. Xia, Y., Gilroy, K. D., Peng, H. C. & Xia, X. Seed-Mediated Growth of Colloidal Metal Nanocrystals. *Angewandte Chemie - International Edition* **56**, 60–95 (2017).
48. Condorelli, M. *et al.* Plasmon sensing and enhancement of laser prepared silver colloidal nanoplates. *Appl. Surf. Sci.* **475**, 633–638 (2019).
49. Barcikowski, S. & Compagnini, G. Advanced nanoparticle generation and excitation by lasers in liquids. *Physical Chemistry Chemical Physics* **15**, 3022–3026 (2013).
50. Amans, D., Cai, W. & Barcikowski, S. Status and demand of research to bring laser generation of nanoparticles in liquids to maturity. *Applied Surface Science* **488**, 445–454 (2019).
51. Amans, D. *et al.* Synthesis of oxide nanoparticles by pulsed laser ablation in liquids containing a complexing molecule: Impact on size

distributions and prepared phases. *J. Phys. Chem. C* **115**, 5131–5139 (2011).

52. Zhang, D., Gökce, B. & Barcikowski, S. Laser Synthesis and Processing of Colloids: Fundamentals and Applications. *Chem. Rev.* **117**, 3990–4103 (2017).
53. Von Der Linde, D. & Sokolowski-Tinten, K. Physical mechanisms of short-pulse laser ablation. *Appl. Surf. Sci.* **154**, 1–10 (2000).
54. Russo, P., Liang, R., He, R. X. & Zhou, Y. N. Phase transformation of TiO 2 nanoparticles by femtosecond laser ablation in aqueous solutions and deposition on conductive substrates. *Nanoscale* **9**, 6167–6177 (2017).
55. Shih, C. Y. *et al.* Two mechanisms of nanoparticle generation in picosecond laser ablation in liquids: The origin of the bimodal size distribution. *Nanoscale* **10**, 6900–6910 (2018).
56. Messina, G. C. *et al.* Tuning the Composition of Alloy Nanoparticles Through Laser Mixing: The Role of Surface Plasmon Resonance. *J. Phys. Chem. C* **120**, 12810–12818 (2016).
57. Parnklang, T. *et al.* H2O2-triggered shape transformation of silver nanospheres to nanoprisms with controllable longitudinal LSPR wavelengths. *RSC Adv.* **3**, 12886–12894 (2013).
58. Zhang, Q. *et al.* Dissolving Ag from Au-Ag alloy nanoboxes with H2O2: A method for both tailoring the optical properties and measuring the H 2O2 concentration. *J. Phys. Chem. C* **114**, 6396–6400 (2010).
59. Elechiguerra, J. L., Reyes-Gasga, J. & Yacaman, M. J. The role of twinning in shape evolution of anisotropic noble metal nanostructures. *J. Mater. Chem.* **16**, 3906–3919 (2006).
60. Jin, R. *et al.* Controlling anisotropic nanoparticle growth through plasmon excitation. *Nature* **425**, 487–490 (2003).

61. Zhang, X.-Y. *et al.* Self-Assembly of Large-Scale and Ultrathin Silver Nanoplate Films with Tunable Plasmon Resonance Properties. *ACS Nano* **5**, 9082–9092 (2011).

62. Kulkarni, A. P., Munechika, K., Noone, K. M., Smith, J. M. & Ginger, D. S. Phase transfer of large anisotropic plasmon resonant silver nanoparticles from aqueous to organic solution. *Langmuir* **25**, 7932–7939 (2009).

63. Smythe, E. J., Cubukcu, E. & Capasso, F. Optical properties of surface plasmon resonances of coupled metallic nanorods. *Opt. Express* **15**, 7439 (2007).

64. Charles, D. E. *et al.* Versatile solution phase triangular silver nanoplates for highly sensitive plasmon resonance sensing. *ACS Nano* **4**, 55–64 (2010).

65. Liu, Y. *et al.* Precision synthesis: Designing hot spots over hot spots via selective gold deposition on silver octahedra edges. *Small* **10**, 4940–4950 (2014).

66. Sherry, L. J., Jin, R., Mirkin, C. A., Schatz, G. C. & Van Duyne, R. P. Localized surface plasmon resonance spectroscopy of single silver triangular nanoprisms. *Nano Lett.* **6**, 2060–2065 (2006).

67. Lee, K. S. & El-Sayed, M. A. Gold and silver nanoparticles in sensing and imaging: Sensitivity of plasmon response to size, shape, and metal composition. *J. Phys. Chem. B* **110**, 19220–19225 (2006).

68. McFarland, A. D. & Van Duyne, R. P. Single silver nanoparticles as real-time optical sensors with zeptomole sensitivity. *Nano Lett.* **3**, 1057–1062 (2003).

69. Vasko, P. D., Blackwell, J. & Koenig, J. L. Infrared and raman spectroscopy of carbohydrates. : Part II: Normal coordinate analysis of α-D-glucose. *Carbohydr. Res.* **23**, 407–416 (1972).

70. Lin, W. C. *et al.* Size Dependence of Nanoparticle-SERS Enhancement from Silver Film over Nanosphere (AgFON) Substrate. *Plasmonics* **6**, 201–206 (2011).

71. Kochuveedu, S. T., Jang, Y. H. & Kim, D. H. A study on the mechanism for the interaction of light with noble metal-metal oxide semiconductor nanostructures for various photophysical applications. *Chem. Soc. Rev.* **42**, 8467–8493 (2013).

72. Sun, Y., Yang, X., Zhao, H. & Wang, R. Non-symmetric hybrids of noble metal-semiconductor: Interplay of nanoparticles and nanostructures in formation dynamics and plasmonic applications. *Progress in Natural Science: Materials International* **27**, 157–168 (2017).

73. Kawahara, T. *et al.* A patterned TiO2(anatase)/TiO2(rutile) bilayer-type photocatalyst: Effect of the anatase/rutile junction on the photocatalytic activity. *Angew. Chemie - Int. Ed.* **41**, 2811–2813 (2002).

74. Cesar, I., Sivula, K., Kay, A., Zboril, R. & Grätzel, M. Influence of Feature Size, Film Thickness, and Silicon Doping on the Performance of Nanostructured Hematite Photoanodes for Solar Water Splitting. *J. Phys. Chem. C* **113**, 772–782 (2009).

75. Maiolo, J. R. *et al.* High aspect ratio silicon wire array photoelectrochemical cells. *J. Am. Chem. Soc.* **129**, 12346–12347 (2007).

76. Goldberger, J. *et al.* Single-crystal gallium nitride nanotubes. *Nature* **422**, 599–602 (2003).

77. Kudo, A. & Miseki, Y. Heterogeneous photocatalyst materials for water splitting. *Chem. Soc. Rev.* **38**, 253–278 (2009).

78. Fang, S. & Hu, Y. H. Recent progress in photocatalysts for overall

water splitting. *International Journal of Energy Research* **43**, 1082–1098 (2019).

79. Vayssieres, L. Growth of arrayed nanorods and nanowires of ZnO from aqueous solutions. *Adv. Mater.* **15**, 464–466 (2003).
80. Wang, X., Summers, C. J. & Wang, Z. L. Large-scale hexagonal-patterned growth of aligned ZnO nanorods for nano-optoelectronics and nanosensor arrays. *Nano Lett.* **4**, 423–426 (2004).
81. Le Ru, E. C. & Etchegoin, P. G. Quantifying SERS enhancements. *MRS Bull.* **38**, 631–640 (2013).
82. Jiang, R., Li, B., Fang, C. & Wang, J. Metal/semiconductor hybrid nanostructures for plasmon-enhanced applications. *Advanced Materials* **26**, 5274–5309 (2014).
83. Kim, M., Lin, M., Son, J., Xu, H. & Nam, J. M. Hot-Electron-Mediated Photochemical Reactions: Principles, Recent Advances, and Challenges. *Adv. Opt. Mater.* **5**, 1700004 (2017).
84. Yin, J. *et al.* Ag nanoparticle/ZnO hollow nanosphere arrays: Large scale synthesis and surface plasmon resonance effect induced Raman scattering enhancement. *J. Mater. Chem.* **22**, 7902–7909 (2012).
85. Lee, J. *et al.* Bioconjugated Ag nanoparticles and CdTe nanowires: Metamaterials with field-enhanced light absorption. *Angew. Chemie - Int. Ed.* **45**, 4819–4823 (2006).
86. Awazu, K. *et al.* A plasmonic photocatalyst consisting of silver nanoparticles embedded in titanium dioxide. *J. Am. Chem. Soc.* **130**, 1676–1680 (2008).
87. Fujishima, A. & Honda, K. Electrochemical photolysis of water at a semiconductor electrode. *Nature* **238**, 37–38 (1972).
88. Vinodgopal, K., Stafford, U., Gray, K. A. & Kamat, P. V. Electrochemically assisted photocatalysis. 2. The role of oxygen and

reaction intermediates in the degradation of 4-chlorophenol on immobilized TiO2 particulate films. *J. Phys. Chem.* **98**, 6797–6803 (1994).

89. Fragalà, M. E., Aleeva, Y. & Malandrino, G. Effects of metal-organic chemical vapour deposition grown seed layer on the fabrication of well aligned ZnO nanorods by chemical bath deposition. *Thin Solid Films* **519**, 7694–7701 (2011).
90. Malandrino, G. *et al.* A novel diamine adduct of zinc bis(2-thenoyl-trifluoroacetonate) as a promising precursor for MOCVD of zinc oxide films. *Inorg. Chem.* **44**, 9684–9689 (2005).
91. D'Urso, L. *et al.* Detection and characterization at nM concentration of oligomers formed by hIAPP, Aβ(1-40) and their equimolar mixture using SERS and MD simulations. *Phys. Chem. Chem. Phys.* **20**, 20588–20596 (2018).
92. Zhang, R., Yin, P. G., Wang, N. & Guo, L. Photoluminescence and Raman scattering of ZnO nanorods. *Solid State Sci.* **11**, 865–869 (2009).
93. Shim, S., Stuart, C. M. & Mathies, R. A. Resonance Raman cross-sections and vibronic analysis of rhodamine 6G from broadband stimulated raman spectroscopy. *ChemPhysChem* **9**, 697–699 (2008).
94. Söderholm, S., Roos, Y. H., Meinander, N. & Hotokka, M. Raman spectra of fructose and glucose in the amorphous and crystalline states. *J. Raman Spectrosc.* **30**, 1009–1018 (1999).
95. Haruta, M. Size- and support-dependency in the catalysis of gold. *Catalysis Today* **36**, 153–166 (1997).
96. Bell, A. T. & Goodman, D. W. The Impact of Nanoscience on Heterogeneous Catalysis. *Science (80-. ).* **299**, 1688–1691 (2003).
97. Mallat, T. & Baiker, A. Oxidation of alcohols with molecular oxygen

on solid catalysts. *Chem. Rev.* **104**, 3037–3058 (2004).

98. Valden, M., Lai, X. & Goodman, D. W. Onset of catalytic activity of gold clusters on titania with the appearance of nonmetallic properties. *Science (80-. ).* **281**, 1647–1650 (1998).

99. Haider, P., Grunwaldt, J.-D., Seidel, R. & Baiker, A. Gold supported on Cu–Mg–Al and Cu–Ce mixed oxides: An in situ XANES study on the state of Au during aerobic alcohol oxidation. *J. Catal.* **250**, 313–323 (2007).

100. Robert, T. D., Laude, L. D., Geskin, V. M., Lazzaroni, R. & Gouttebaron, R. Micro-Raman spectroscopy study of surface transformations induced by excimer laser irradiation of TiO2. *Thin Solid Films* **440**, 268–277 (2003).

101. Bersani, D., Antonioli, G., Lottici, P. P. & Lopez, T. Raman study of nanosized titania prepared by sol-gel route. *J. Non. Cryst. Solids* **232**–**234**, 175–181 (1998).

102. Söderholm, S., Roos, Y. H., Meinander, N. & Hotokka, M. Raman spectra of fructose and glucose in the amorphous and crystalline states. *J. Raman Spectrosc.* **30**, 1009–1018 (1999).

103. Parker, J. C. & Siegel, R. W. Raman Microprobe Study of Nanophase TiO2 and Oxidation-Induced Spectral Changes. *J. Mater. Res.* **5**, 1246–1252 (1990).

104. Zhu, Q. *et al.* Stable blue TiO2-x nanoparticles for efficient visible light photocatalysts. *J. Mater. Chem. A* **2**, 4429–4437 (2014).

**Supporting information**

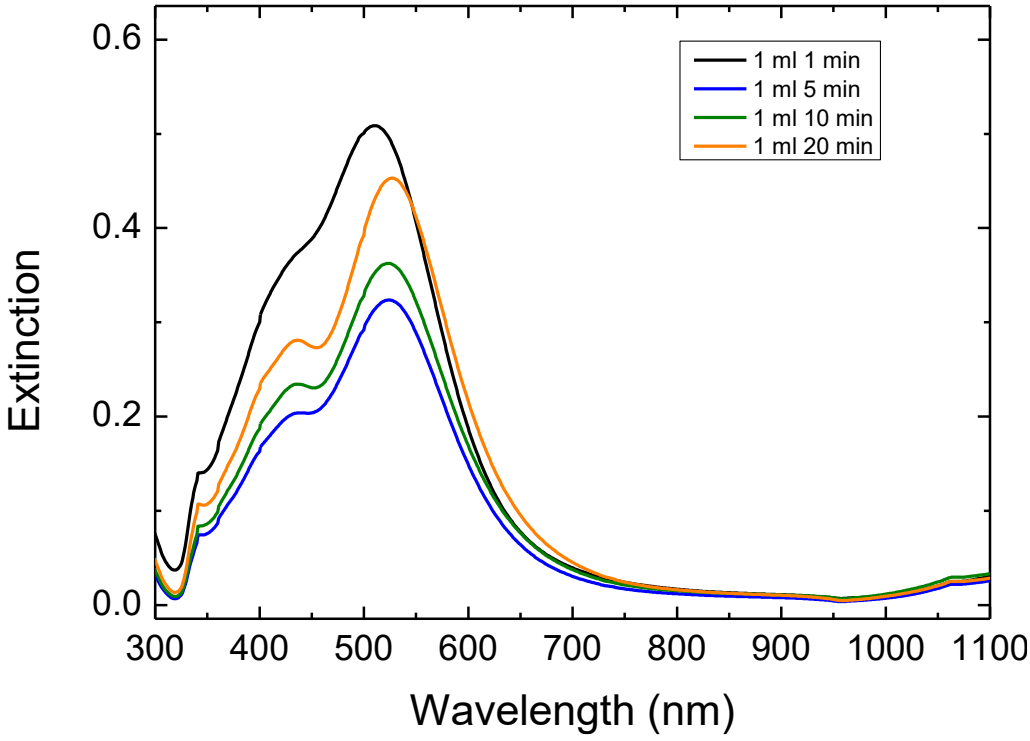


***S 1:****Extiction spectra of NPT grown with 1 ml addition rate from 1 to 20 minutes*

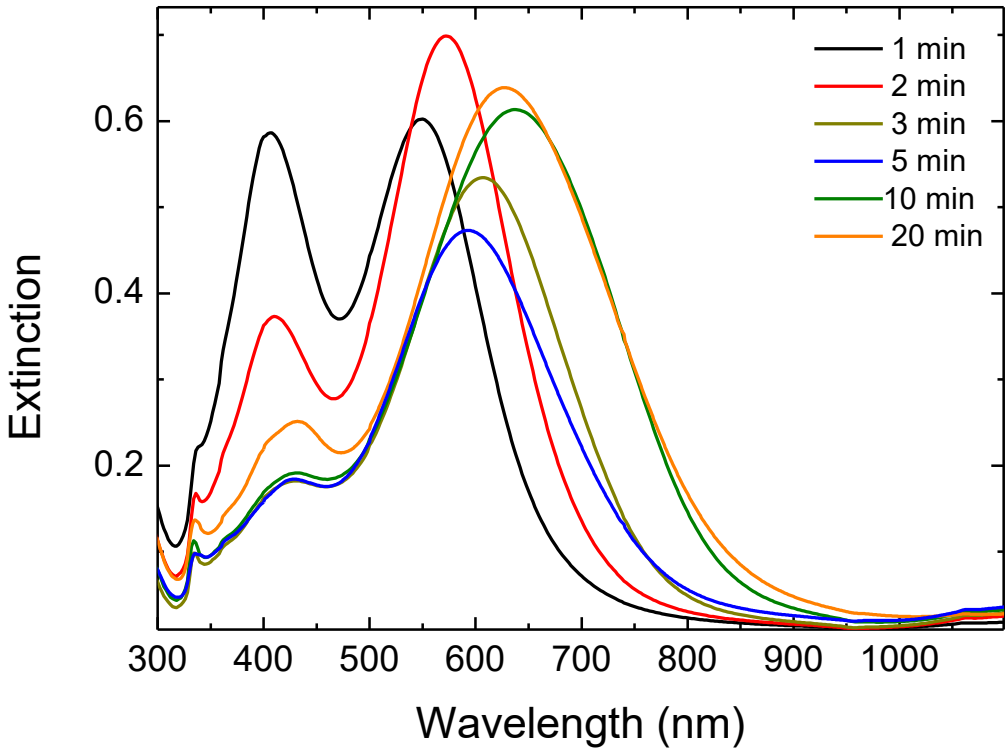


***S 2:*** *Extiction spectra of NPT grown with 350 µl addition rate from 1 to 20 minutes*

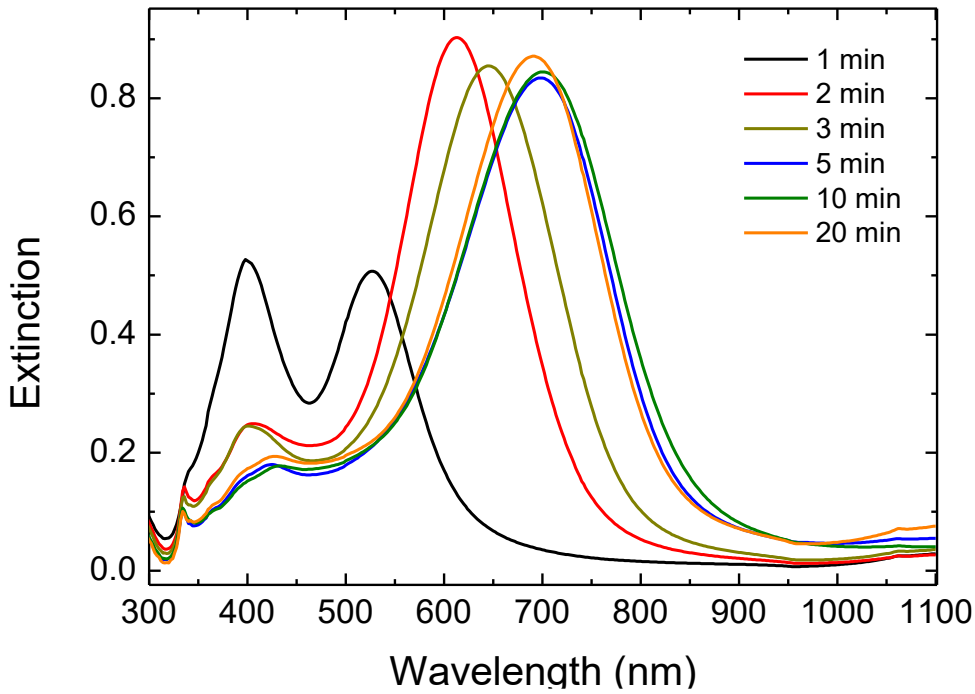


***S.3:*** *Extiction spectra of NPT grown with 160 µL with addition rate from 1 to 20 minutes*

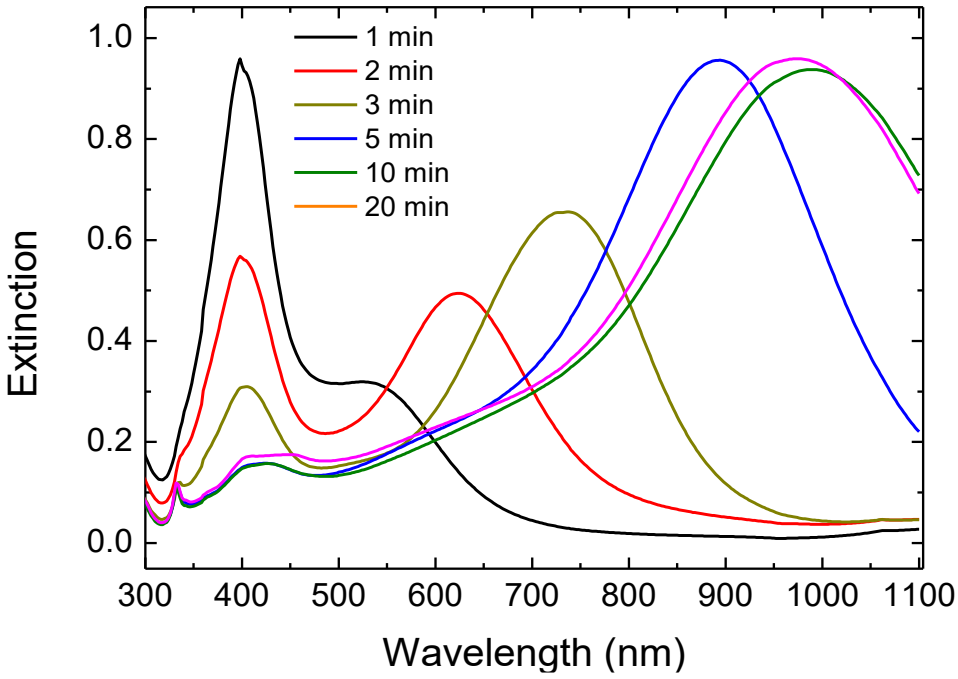


***S 4:*** *Extiction spectra of NPT grown with 80 µl with addition rate from 1 to 20 minutes*

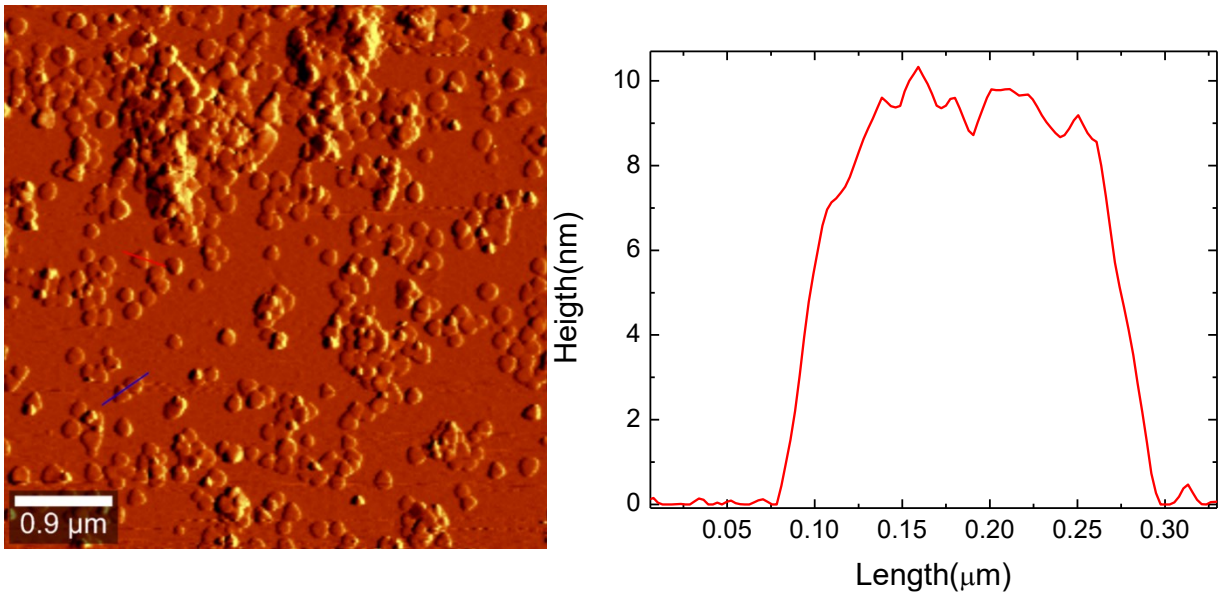


***S 5:*** *AFM image and section analysis of Silver Nanoplatetelets grown with 80 µl of seeds*

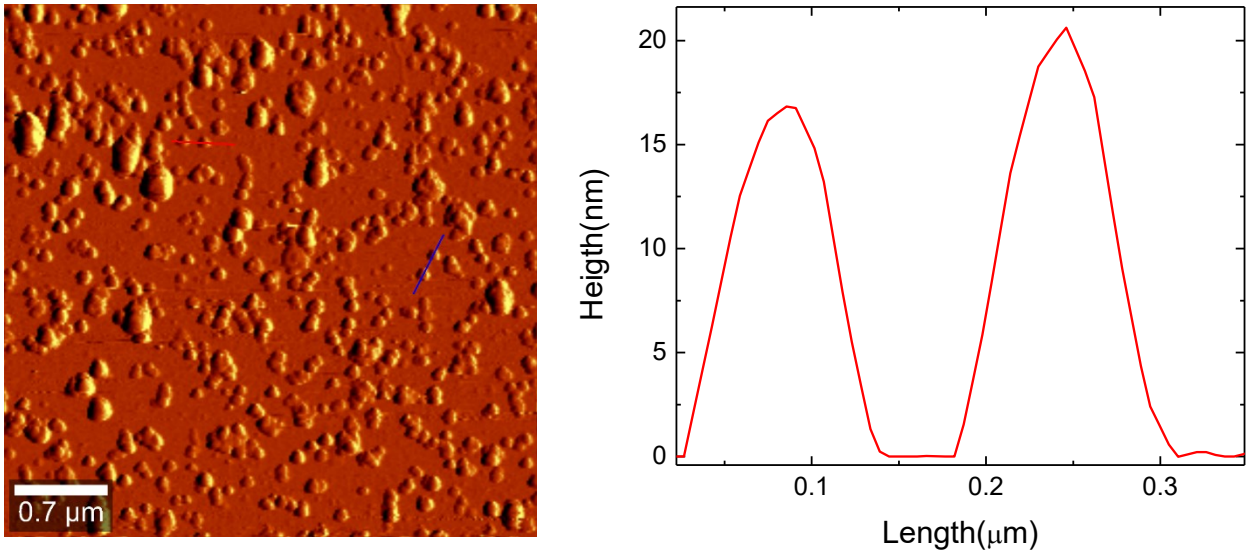


***S 6:*** *AFM image and section analysis of Silver Nanoplatetelets grown with 350 µL of seeds*

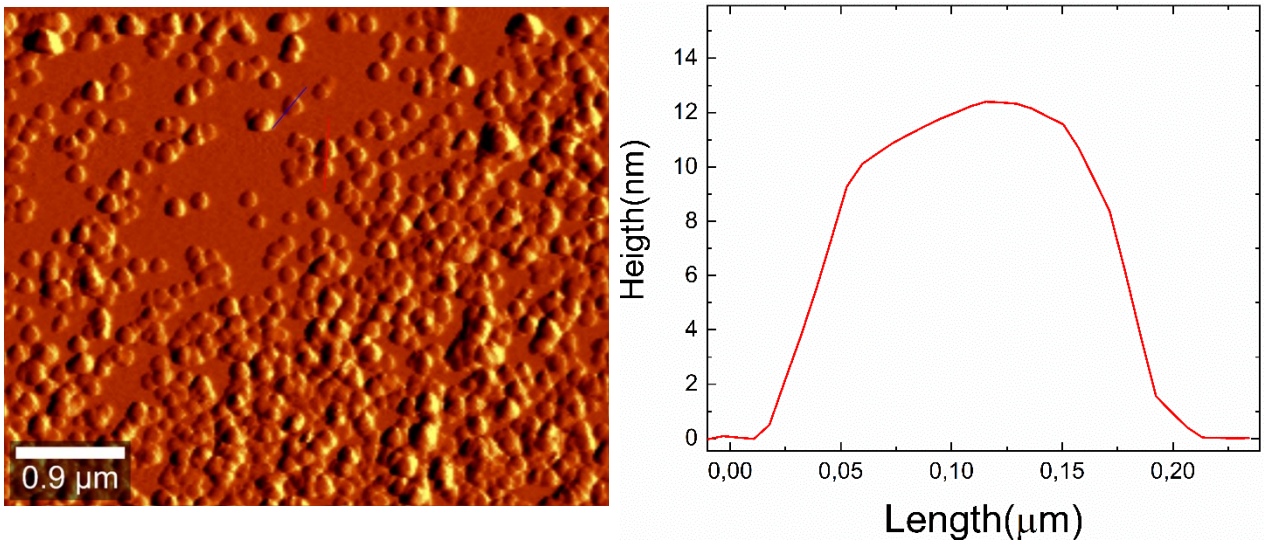


***S 7:*** *AFM image and section analysis of Silver Nanoplatetelets grown with 160 µl of seeds*

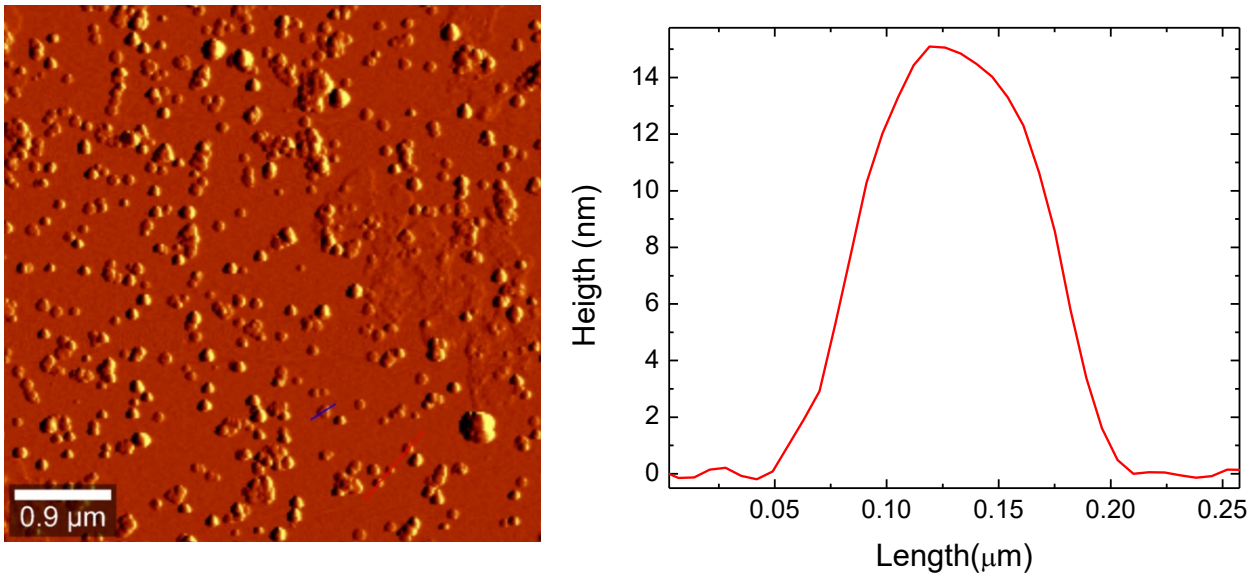


***S 8:*** *AFM image and section analysis of Silver Nanoplatetelets grown with 1 ml of seeds*

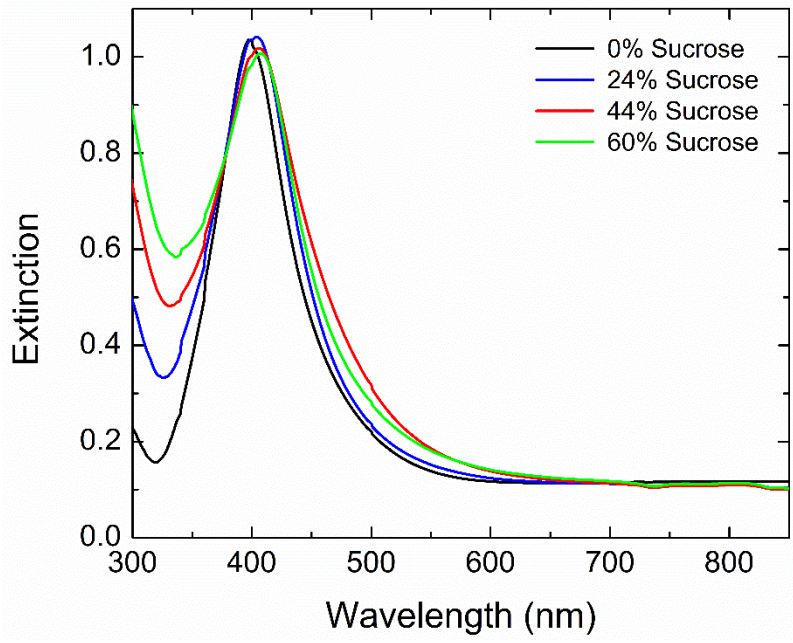


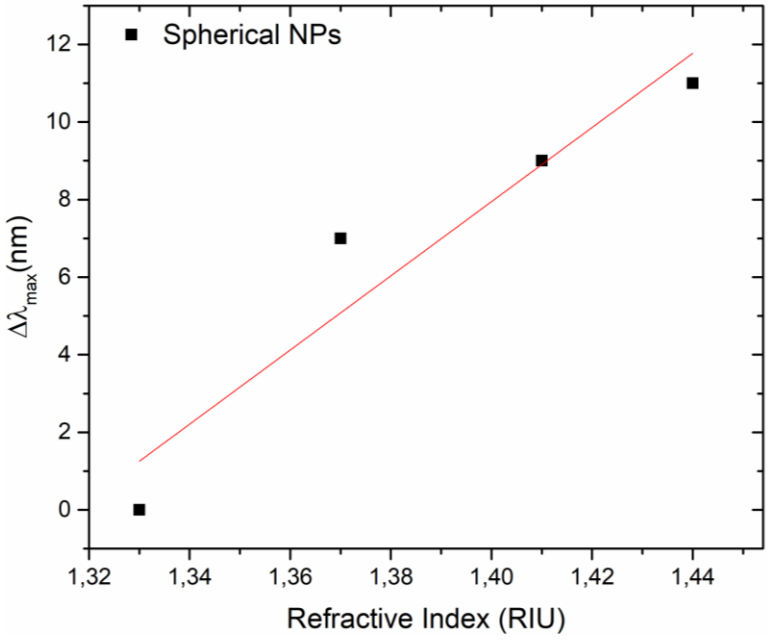


***S 9:*** *a) Extinction spectra spherical AgNPs with different sucrose solution, b)plot of* $\Delta\lambda_{max}$ *in function of refractive index*

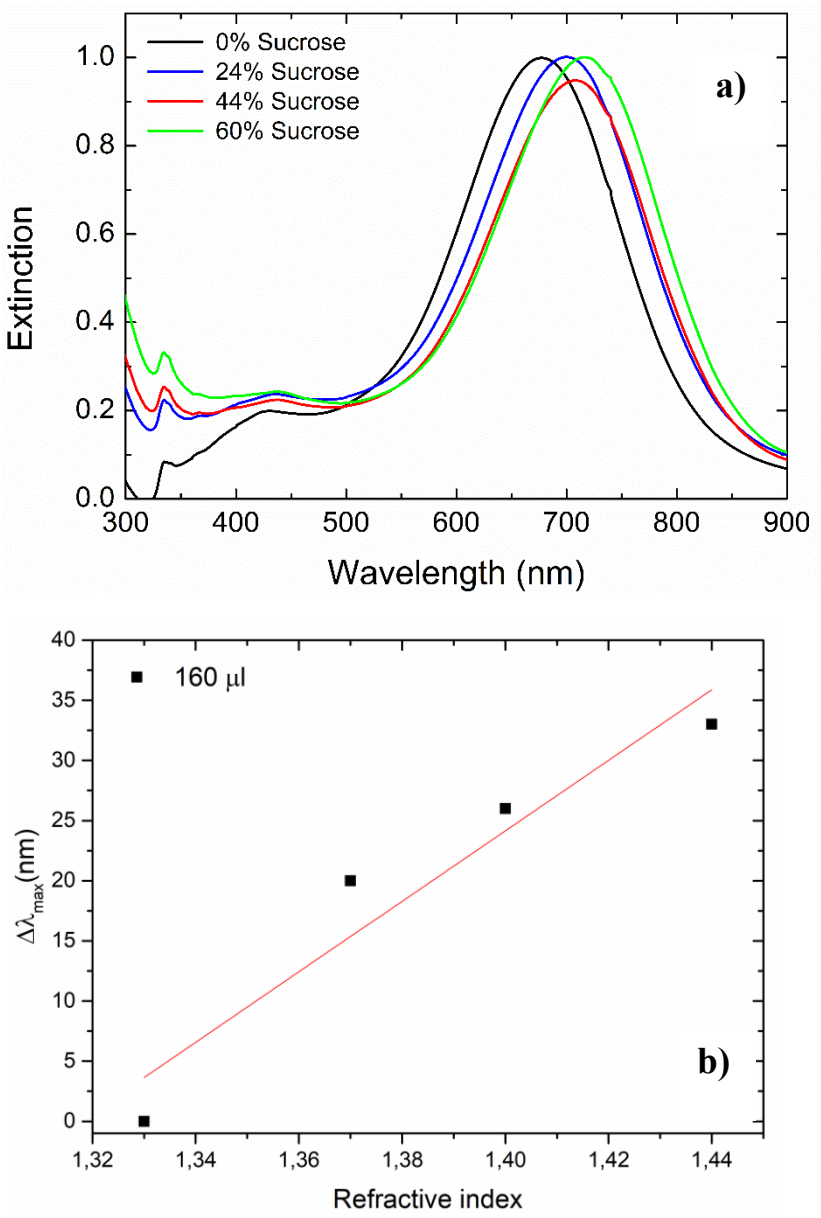


***S 10:*** *a) Extinction spectra of NPTS grown with 160µL of seeds with different sucrose solution, b) plot of $\Delta\lambda_{max}$ in function of refractive index*

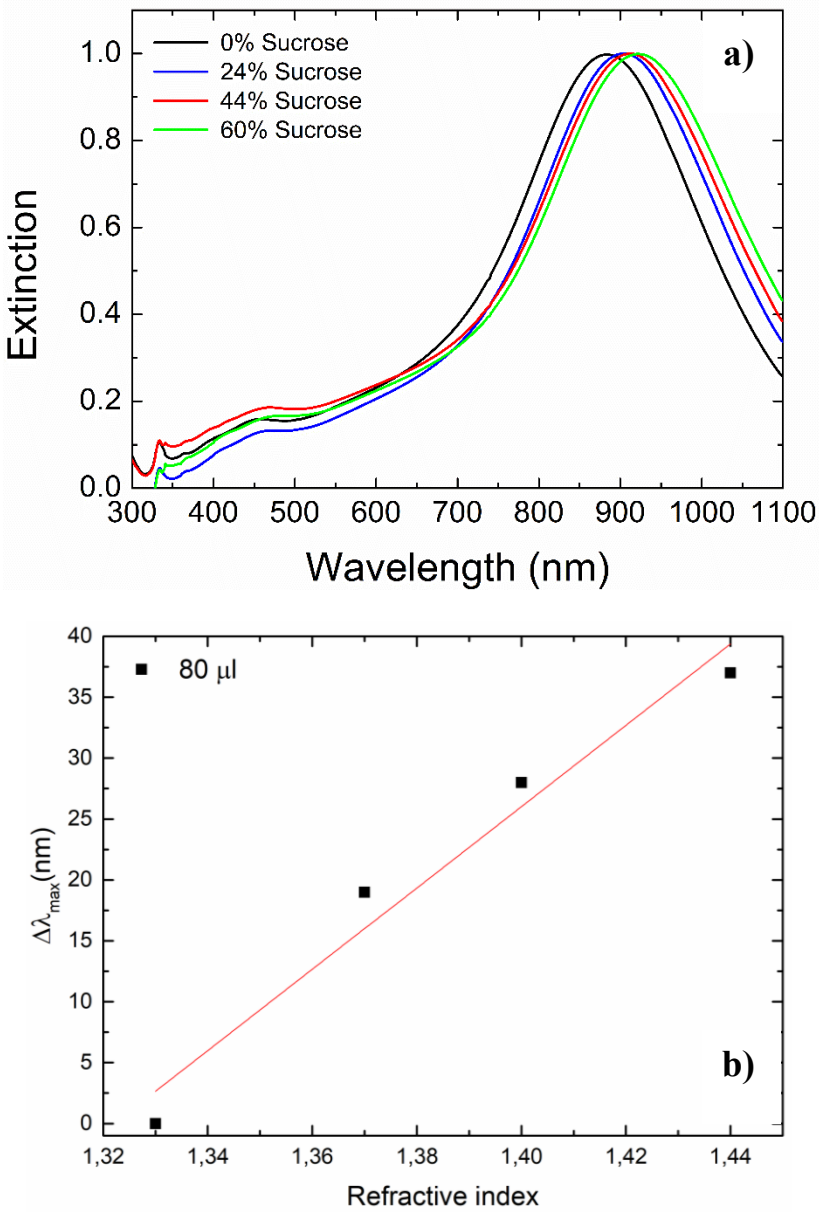


***S 11:.*** *Extinction spectra of NPTS grown with 80µl of seeds with different sucrose solution, b) plot of* $\Delta\lambda_{max}$ *in function of refractive index*

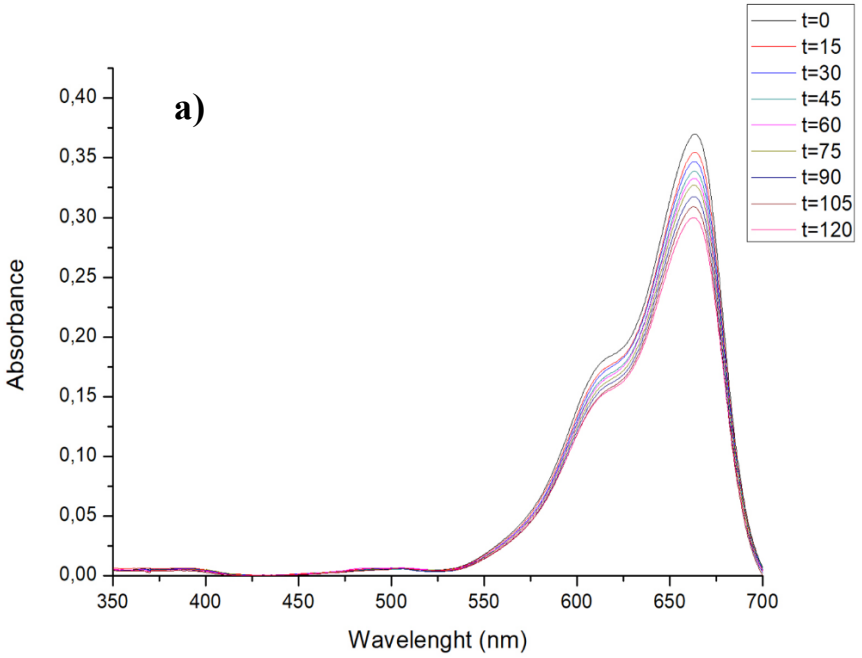
a)
Absorbance
Wavelenght (nm)
0,00
0,05
0,10
0,15
0,20
0,25
0,30
0,35
0,40
350
400
450
500
550
600
650
700
t=0
t=15
t=30
t=45
t=60
t=75
t=90
t=105
t=120

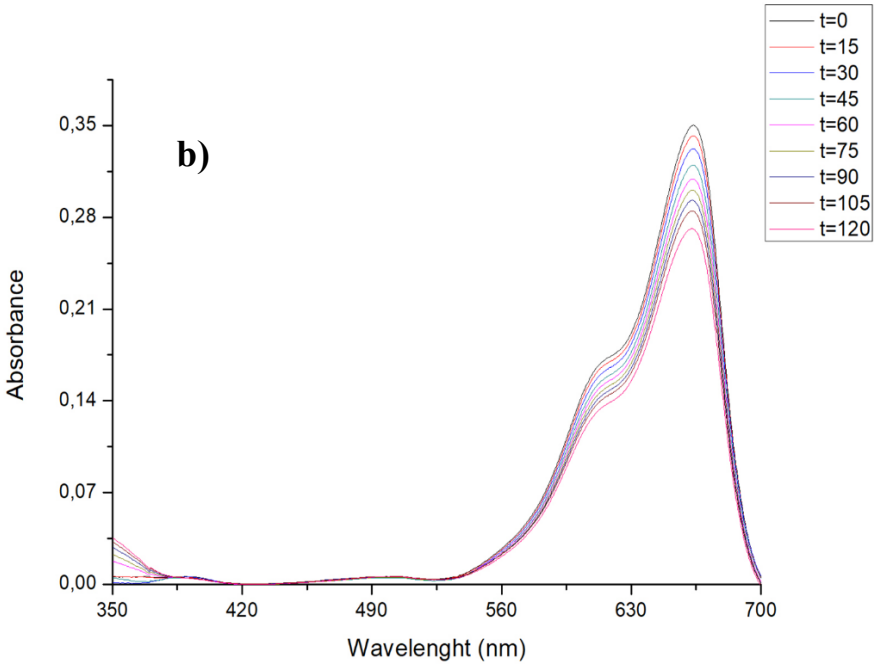
b)
Absorbance
Wavelenght (nm)
0,00
0,07
0,14
0,21
0,28
0,35
350
420
490
560
630
700
t=0
t=15
t=30
t=45
t=60
t=75
t=90
t=105
t=120

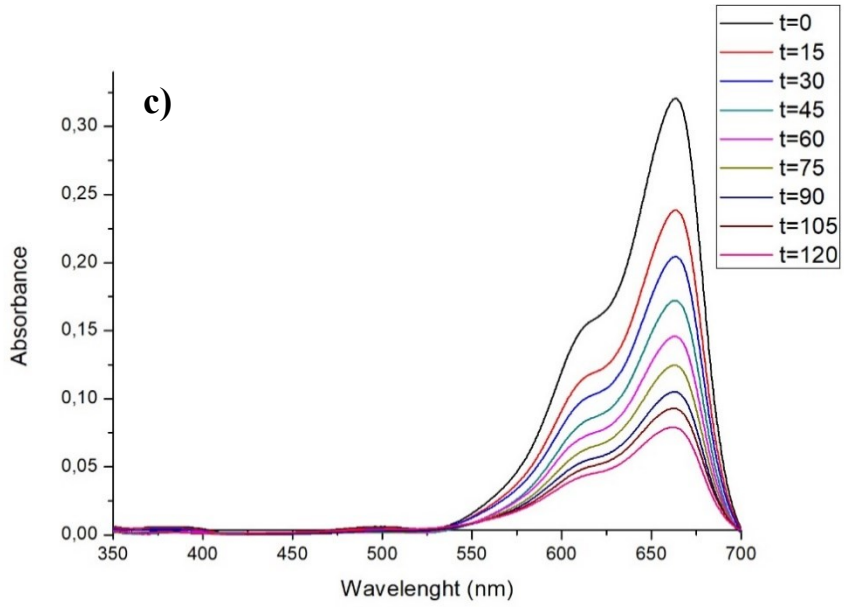


***S 12:*** *Spectra of Absorbance of MB solutions: a) Sample with ZnO film on Si; b) Sample with ZnO nanorods on spherical AgNs on Si (deposited at 650°C for 60 minutes by MOCVD); c) Sample with ZnO nanorods on AgNPTs on Si (deposited at 650°C for 60 minutes by MOCVD)*